TOPOLOGY OPTIMIZATION ALGORITHMS FOR IMPROVED MANUFACTURABILITY AND CELLULAR MATERIAL DESIGN

by

Josephine Voigt Carstensen

A dissertation submitted to The Johns Hopkins University in conformity with the requirements for the degree of Doctor of Philosophy.

Baltimore, Maryland

July, 2017

Abstract

Topology optimization is a free-form approach to structural design in which a formal optimization problem is posed and solved using mathematical programming. It has been widely implemented for design at a range of length scales, including periodic cellular materials. Cellular materials in this context refer to porous materials with a representative unit cell that is repeated in all directions. For cellular material design an upscaling law is required to connect the unit cell topology to the bulk material properties. This has limited most work on topology optimization of cellular materials to linear properties, such as elastic moduli or thermal conduction, where numerical homogenization can be used. Although topology-optimized materials are often shown to outperform conventional cellular material designs, the optimized designs are often complex and can therefore be difficult to fabricate. This is true despite the rapid development of manufacturing technologies that have provided radically new capabilities. Although such technologies have reduced the manufacturing constraints, there are still limitations. This thesis looks to advance topology optimization of cellular materials on two fronts: (i) by more formally integrating manufacturing constraints

and capabilities into topology optimization methodology, and (ii) by moving beyond linear properties to consider the nonlinear response of cellular materials.

In this work we propose to implicitly integrate manufacturing considerations into the topology optimization formulation by using projection based approaches. We seek to improve the manufacturability of topology-optimized structures by providing the designer minimum length scale control of both the design's solid and void phases. The new two-phase projection algorithm is demonstrated on benchmark examples and uses nonlinear weighting functions to let the design variable magnitude determine if solid or void should be actively projected. In addition, we utilize a multi-phase cellular design approach that can leverage the new capability of deposition of multiple solids that is offered by current 3D printing technologies. These multi-phase designs generally outperform two-phase topologies and potentially offer new functionalities. Our algorithm is based on an existing multimaterial formulation and used to design cellular topologies for various elastic properties, including negative Poisson's ratio, and for multiobjectives including mechanical and thermal properties.

Expanding topology optimization to cellular design governed by nonlinear mechanics enables designing effective materials with a range of new improved properties such as energy absorption. However, considering material– and/or geometric nonlinearities in cellular design faces the challenge of the lack of a recognized upscaling technique. Previous works have turned to finite periodicity. This thesis will explore the necessary steps in developing a topology optimization algorithm for cellular de-

ABSTRACT

sign governed by nonlinear mechanics. Further, the forward homogenization problem of how the unit cell topology effects the effective material's energy absorption will be numerically investigated for a range of conventional and topology-optimized unit cells.

Primary Reader: James K. Guest

Secondary Readers: Stavros Gaitanaros and Alberto Donoso

Acknowledgments

First, I want to thank the Department of Civil Engineering at Johns Hopkins University – this includes both the faculty, students and staff. The support I have received through the years has made my time as a grad student an amazing experience. I want to give a special thanks Prof. James K. Guest for all his enthusiasm, guidance and encouragement. His advising is a major source of inspiration.

Secondly, I want thank Prof. Stavros Gaitanaros and Prof. Alberto Donoso for serving as thesis readers, and Prof. Benjamin W. Schafer and Prof. Lori Graham-Brady for serving on my committee.

I would also like to thank Prof. Grunde Jomaas (University of Edinburgh) and Prof. José L. Torero (University of Maryland) for first planting the idea of pursuing grad school at Johns Hopkins.

Finally, I want to acknowledge the financial support from the National Science Foundation grant No. 1400394, DARPA through the MCMA program, the Denmark-America Foundation, as well as financial support for travel from the US Association of Computational Mechanics, the Hopkins Extreme Material Institute, and the Dean's

ACKNOWLEDGMENTS

Office at Johns Hopkins University. The support is greatly appreciated.

Dedication

To Edith & Francesco

Contents

Abstract **ii**

Acknowledgments **v**

List of Tables **xii**

List of Figures **xiii**

1 Introduction **1**

2 Improved Manufacturability by Length Scale Control **6**

2.1 Introduction 6

2.2 The Heaviside Projection Method 12

2.3 Two-Phase Projection with Nonlinear Weighting Functions 15

2.4 Solution Algorithm 16

2.4.1 Penalization of Intermediate Densities 17

2.4.2 Sensitivities 17

2.4.3 Optimizer 18
2.5 Numerical Examples 19
2.5.1 MBB and Cantilever Beams 21
2.5.2 Heat Sink 24
2.5.3 Compliant Inverter Mechanism 26
2.6 Maximum Length Scale on the Solid Phase 27
2.6.1 Cantilever Beam 29
2.7 Summary 31

3 Elastic Cellular Materials with Multiple Base Solids 33

3.1 Introduction 33
3.2 The Inverse Homogenization Problem 39
3.2.1 Numerical Homogenization 40
3.2.2 Mechanical Properties and Symmetry 42
3.2.2.1 Symmetry Constraints on the Constitutive Matrix . 43
3.2.2.2 Homogenized Mechanical Properties 44
3.2.3 Thermal Conduction and Symmetry 49
3.2.4 Penalization of Intermediate Densities 50
3.2.5 Sensitivities 51
3.2.6 Algorithmic Details 54
3.3 Cellular Material Topologies with Two Material Phases 55
3.3.1 Optimizing for Mechanical Properties 56

3.3.2 Multiobjectives in the Mechanical and Thermal Behaviors . . 60

3.4 Cellular Material Design with Multiple Material Phases 63

3.4.1 Topologies with Improved Mechanical Properties 66

3.4.2 Designs Optimized for Stiffness–Conduction Objectives 70

3.5 Summary 72

4 Cellular Materials with Nonlinear Properties 74

4.1 Introduction 74

4.2 Topology Optimization of Beams with Nonlinear Mechanics 79

4.2.1 Solids-Only Modeling in the Physical Space 81

4.2.2 Geometric Nonlinearities 82

4.2.2.1 Penalization of Intermediate Densities 84

4.2.2.2 Sensitivities 84

4.2.2.3 Cantilever Beam Designs 86

4.2.3 Material Nonlinearities 87

4.2.3.1 Penalization of Intermediate Densities 89

4.2.3.2 Sensitivities 90

4.2.3.3 Clamped Beam Designs 95

4.3 Extending to Cellular Topology Design with Nonlinear Mechanics . . 97

4.4 Energy Absorption of Cellular Bulk Metallic Glass Topologies 99

4.5 Summary 106

5 Concluding Remarks and Future Work **108**

Bibliography **111**

Vita **130**

List of Tables

2.1 Combinations of ρ_s^e, ρ_v^e and ρ_{xv}^e and the resulting ρ^e from Eq. (2.4) and Eq. (2.15) with $c_{r_{min}} = 2.0$. 29
2.2 Compliances obtained with $\eta = 1$ and $\eta = 15$ for the cantilever beam designs with maximum length scale control in Fig. 2.10. 31

3.1 Normalized performance of the unit cell topologies with three material phases (Fig. 3.10). The normalization is performed by dividing with the objective values obtained with two material phases (Fig. 3.4). . . 68
3.2 Comparison of the performance and material use in the robust negative Poisson's ratio designs with two material phases (Fig. 3.6b) and three material phases (Fig. 3.11). 70

4.1 Absorbed energies [MJ/m^3] in the response plots in Fig. 4.8 obtained by numerical analyses of 5×5 samples of the unit cells in Fig.s. 4.5-4.7. The largest magnitude for each volume constraint is indicated in bold. 105

List of Figures

2.1 Examples of undesirable features in the non-controlled phase of topology-optimized MBB beams with minimum length scale control on (a) the solid phase and (b) the void phase. 8

2.2 Schematic of (a) the two spaces of the topology optimization problem with the spheres symbolizing the design variable space and the blocks signifying the physical representation. Figure (b) shows the radial projection of the design variable ϕ_i onto the finite elements with $r_{min,p}$, and (c) gives the element perspective of the radial projection with an element e receiving design variable information from within the projection domain N_p^e. 12

2.3 The nonlinear weighting functions $w_s(\phi)$ and $w_v(\phi)$ in the interval ϕ_{min} to ϕ_{max} for $\alpha_s = 0.15$ and $\alpha_v = 0.05$. 15

2.4 Design domains for (a) the cantilever beam–, (b) the MBB beam–, (c) the heat conduction–, and (d) the compliant mechanism design problem. 20

2.5 MBB beam designs with $r_{min,p} = 1$ for (a) solid projection, (b) void projection, and (c) improved two-phase projection. 22

2.6 Element volume fraction distributions (ρ^e) obtained for the cantilever problem with $r_{min,s} = r_{min,v} = 0.5$ on a (a) 80×50 mesh, and a (b) 240×150 mesh. Figure (c) illustrates how a $r_{min,s} + r_{min,v}$ layer of non-projecting design variables is needed for a crips boundary, and (d) gives the design variable distribution (ϕ_i) for the topology in (b). . . 23

2.7 Results of the heat conduction problem with $r_{min,p} = 0.015$ for (a) solid projection, (b) void projection, and (c) the new two-phase projection. 24

2.8 Topologies obtained for the heat conduction problem with $r_{min,v} = 0.02$ and (a) $r_{min,s}$ = NA, (b) $r_{min,s} = 0.005$, (c) $r_{min,s} = 0.01$, (d) $r_{min,s} = 0.015$, and (e) $r_{min,s} = 0.02$. 25

2.9 Compliant inverter mechanism designs obtained with $r_{min,s} = 4.0$ and (a) $r_{min,v} = 4.0$, and (b) $r_{min,v} = 2.0$. 27

2.10 Distribution of the volume fraction ρ^e found for the cantilever beam problem with $r_{min,s} = r_{min,v} = 0.5$, $a_s = 0.0005$, $a_v = 0.002$ and $a_{xv} = 0.001$, $\beta_x = 15$, $c_{r_{max}} = 1.90$ and $\eta_{max} = 15$ on a 80×50 mesh with (a) $r_{max,s} = 2.0$, (b) $r_{max,s} = 3.0$, (c) $r_{max,s} = 6.0$ and (d) $r_{max,s} =$ NA. 30

3.1 Schematic of topology optimization for cellular materials; (a) the unit cell design domain, (b) the optimized unit cell topology, and (c) the unit cell in the effective bulk material. 34
3.2 Boundary conditions applied in numerical homogenization of a 2D unit cell for (a) the normal test strain fields $\epsilon^{0(11)}$ and $\epsilon^{0(22)}$, and (b) the pure shear test strain field $\epsilon^{0(12)}$. 41
3.3 Scaled graded initial guesses for the design variables ϕ_i with (a) solid, and (b) void in the center. 55
3.4 Unit cell topologies and 3×3 samples maximized for the stiffness objectives bulk–, Young's– and shear modulus as defined in Eq.s (3.13), (3.16) and (3.18) with $V_{max} = 50\%$ and square symmetry constraints. 56
3.5 Unit cell topologies and 3×3 samples with maximized bulk modulus from Eq. (3.13) with isotropic symmetry constraints and $V_{max} = 50\%$. 57
3.6 Negative Poisson's ratio designs with $V_{max} = 20\%$, a square symmetry constraint and $r_{min} = 0.015$ using (a) the regular problem formulation in Eq. (3.40) and (b) the robust problem formulation in Eq. (3.40) with $\Delta r = 0.005$. 58
3.7 Schematic of the robust topology optimization formulation used herein. Figure (a) illustrates the material placement space that projects twice onto the physical space, and (b) shows a top view of a design variable projecting with $r_{min} - \Delta r$ and $r_{min} + \Delta r$ onto the finite elements. . . 59
3.8 Unit cell and 3×3 samples of topologies maximized for multiobjectives of bulk modulus B^H and thermal conduction κ^H as defined in Eq.s (3.13) and (3.25). 62
3.9 Schematic of the used multimaterial topology optimization approach for design with two solid materials that varyies with ΔE in stiffness. Figure (a) illustrates the two material placement spaces and the physical represenation, and (b) shows how the placement spaces each projects features with ΔE stiffness onto the finite elements. . . . 63
3.10 Multimaterial unit cell topologies maximized for the stiffness objectives bulk–, Young's– and shear modulus as defined in Eq.s (3.13), (3.16) and (3.18) with $V_{max} = 50\%$, $V_2 = 1.00V_1$ and $V_2 = 0.80V_1$. 66
3.11 Multimaterial negative Poisson's ratio design with $V_{max} = 20\%$ and $V_2 = 1.00V_1$; (a) gives unit cell topology, and (b) provides a 3×3 sample of the effective material. A square symmetry constraint is applied and a robust formulation is used with $r_{min} = 0.015$ and $\Delta r = 0.005$. . . . 69

3.12 Multimaterial unit cell topologies maximized for multiobjective combinations of bulk modulus B^H and thermal conduction κ^H as defined in Eq.s (3.13) and (3.25) with $V_{max} = 50\%$ and $V_2 = 1.00V_1$. 72

4.1 Design domains for the benchmark beam design problems that considers (a) geometric– , and (b) material nonlinear effects. 80
4.2 Solutions to the benchmark cantilever beam problem with geometric nonlinearities and the final compliance objective from Eq. (4.5). The figure contains the obtained topologies for a various amplitudes of the applied load and provides elastic designs for comparison. 86
4.3 The obtained topology from Fig. 4.2 with $P = 144$ kN in its (a) undeformed and (b) deformed state. 88
4.4 Solutions to the benchmark clamped beam problem with maximized energy absorption as defined in Eq. (4.12) and an elastic– and an elasto-plastic material model, respectively. 95
4.5 Previously obtained unit cell topologies maximized for absorbed energy considering both material– and geometric nonlinearities. A bulk metallic glass (BMG) is used as the base material, the minimum length scale is prescribed as $r_{min} = 0.006$ and designs are made with volume constraints of $V_{max} = 10\%$, $V_{max} = 12.5\%$ and $V_{max} = 25\%$. 100
4.6 Response comparison for $V_{max} = 10\%$ of 5×5 samples of the unit cell topology with optimized energy absorption (Fig. 4.5) and a regular grid. The deformed states are illustrated in the plot and the magnitudes of the absorbed energies are listed. 101
4.7 Unit cell designs obtained with linear topology optimization for maximized bulk–, Young's– and shear modulus and minimized Poisson's ratio. The base material is a bulk metallic glass (BMG) and the minimum length scale is prescribed as $r_{min} = 0.006$ for the stiffness objectives. A robust formulation is used for the negative Poisson's ratio designs with $r_{min} = 0.0075$ and $\Delta r = 0.0025$. 103
4.8 Stress-strain responses obtained by the nonlinear FE analysis of 5×5 cellular material samples. The absorbed energies for of the each cellular materials are listed in Tab. 4.1. 104

Chapter 1

Introduction

In recent years manufacturing technologies, including 3D printing, have developed rapidly and made it possible to fabricate increasingly complex designs. This has created a demand for new design methods that can leverage the new manufacturing possibilities. Topology optimization offers a means to create designs that take full advantage of the potentials provided by the new fabrication techniques. It is a free-form design approach that aims at finding optimal distributions of material within a domain. Both the material layout and connectivity are optimized without a predetermined notion of the design. It has therefore been known to lead to new and unanticipated designs that typically outperform conventional low weight designs.[1] Topology optimization has been implemented for design at length scales ranging from tall buildings,[2] over devices and components, such as the structural beams of airplane wings,[3] and periodic cellular materials with numerous improved properties. Examples

of topology-optimized cellular materials are listed in the review papers by Cadman et al.[4] and Osanov and Guest[5] and include auxetics,[6,7] materials with improved thermoelastic–[8,9] or piezoelectric–[10,11] properties, improved fluid permeability,[12–14] and improved stiffness–thermal conductivity.[15] In this work we aim at developing topology optimization algorithms to improve the manufacturability of the designs as well as algorithms for designing cellular topologies with multiple base materials or nonlinear mechanical properties.

Typical topology optimization approaches requires the designer to define a design domain Ω with applied loads and boundary conditions. The domain is discretized most often using finite elements. A formal optimization problem is posed and solved using a mathematical program. The problem typically has an objective f that, for example, is to minimize (or maximize if negative) the compliance, strain energy or displacements of the design. This will be subject to a structural equilibrium constraint and a limitation on the material use in the design domain. A commonly used problem formulation for linear elastic design is as follows.

$$\begin{aligned} \underset{\phi}{\text{minimize}} \quad & f = \mathbf{L}^T\mathbf{d} \\ \text{subject to} \quad & \mathbf{K}(\phi)\mathbf{d} = \mathbf{F} \\ & \textstyle\sum_{e\in\Omega} \rho^e v^e \leq V_{max} \\ & \phi_{min} \leq \phi_i \leq \phi_{max} \quad \forall\ i \in \Omega \end{aligned} \tag{1.1}$$

Here ϕ are the design variable, $\mathbf{F}$ are the nodal forces, $\mathbf{d}$ are the nodal displacements

and $\mathbf{K}$ is the global stiffness matrix. The allowable volume of material within the design domain is denoted V_{max} and v^e is the volume of element e. For minimum compliance problems $\mathbf{L} = \mathbf{F}$, whereas for a minimum displacement objective $\mathbf{L}$ is a vector with value one at the displacement(s) of concern and zeros at all other locations. Alternatively, the topology optimization problem in Eq. (1.1) can be formulated with minimizing the material use at the objective, subject to a stiffness or displacement constraint.

A mathematical programming method is used to solve Eq. (1.1), however, solving it as a binary 0-1 (existence or non-existence of material in an element in the design domain) optimization problem is an immense task. It is well established that the size and complexity of the design space makes stochastic search methods impractical.[16] Typical topology optimization approaches therefore relax the 0-1 constraint and make it possible to use gradient based optimizers. It should be noted that this requires sensitivity evaluations of the objective and constraints in Eq. (1.1). As described in the review by Sigmund and Maute,[17] the binary relaxation approaches include level-set– and density based methods. In this work we use the density based approach where intermediate element densities are allowed to exist. An element density magnitude between zero and one is interpreted as a mixture of solid and void material.[18] The intermediate densities are penalized using interpolation schemes[19–21] that guides the design to a 0-1 solution.

The free-form nature of topology optimization is well known to lead to complex

design solutions that can be difficult to construct or fabricate. One means to improve the manufacturability is to control the minimum length scales of the design. The phase (solid or void) where it is relevant to control the minimum length scale is dictated by the manufacturing process. If the design, for example, is going to be fabricated by a material removal process such as CNC machining the curvature of the holes will be prescribed by the size of the drill. Similarly if a 3D printing technology is used, the printer resolution determines the minimum size of the solid features of the design. Several approaches exist for controlling the minimum length scale of a single phase of the design.[22,23] However, undesirable features can still occur in the uncontrolled phase. To improve the manufacturability of topology-optimized design we have developed an algorithm that allows for minimum length scale control of both phases. Chapter 2 present the proposed two-phase projection method that uses nonlinear weighting function to let the design variable magnitude determine if solid or void is actively projected. Ongoing work is to extend the algorithm to maximum length scale control.

As mentioned, topology optimization has been widely applied to design periodic cellular materials with improved elastic properties. Here a periodic cellular material refers to a material with a representative unit cell that is repeated throughout. Generally the following topics are interesting to investigate for cellular materials: (i) the forward problem of how the topology influences the effective material properties, and (ii) the inverse problem of what unit cell topology that optimizes these effec-

tive properties. For both topics an upscaling law is required to connect the unit cell mechanics to the effective material behavior. Numerical homogenization is typically used for linear elastic properties. Novel 3D printing technologies can deposit multiple materials in complex cellular topologies. Therefore we propose an algorithm to solve a multi-phase inverse homogenization problem in Chapter 3. The suggested approach allows cellular design with multiple base materials for optimized elastic properties and uses an exiting multimaterial approach[24] as the backbone of the algorithm.

Topology optimization of periodic cellular materials with nonlinear mechanics is a far more challenging task, primarily due to the lack of rigorous upscaling techniques. Therefore most efforts in including nonlinear effects has focused on structural, component and device design and material– and geometric nonlinearities have typically been considered separately.[25–27] However, including nonlinearities in cellular design offers immense opportunities in designing for improved nonlinear properties such as energy absorption. Therefore Chapter 4 examines the necessary steps in developing a topology optimization algorithm for the inverse problem (ii). The aim is a design formulation that includes both geometric– and material nonlinearities. In lack of a recognized homogenization technique for nonlinear properties we suggest using finite periodicity for the upscaling. In addition, Chapter 4 investigates the forward problem (i) as the energy absorption of numerous traditional and optimized cellular topologies are analyzed and compared.

Chapter 2

Improved Manufacturability by Length Scale Control

2.1 Introduction

Topology optimization is a free-form design approach and therefore it may result in designs that are difficult to fabricate or construct. Examples of features that impede fabrication include ultra slender structural features or small scale pore spaces. To improve manufacturability, the capabilities and/or limitations of the planned fabrication process must be integrated in the design process. In recent years, several algorithms have therefore been developed to include the potentials and restrictions of various manufacturing processes in topology optimization. Examples include the constraints associated with milling and casting methods that have been implemented

for both density based and level-set topology optimization.[28,29] For concrete design a strut-and-tie model has been implemented to design the layout of discrete reinforcement bars[30,31] and discrete objects for general applications has been placed through the projection in the density based approach.[32–34]

The rapid development of additive manufacturing technologies, such as 3D printing, has raised a need for design method that can leverage the new fabrication possibilities. Therefore algorithms have been developed that can create topology-optimized designs without sacrificial support material and hence designs that satisfies the overhang constraint.[35–37] In addition, infill optimization[38] has been performed and a consideration of the the layer-by-layer nature of 3D printing has been implemented.[5,39] Several 3D printing technologies allows for multiple materials to be printed adjacent to each other in complex topologies and this capability has been leveraged by[24,40] (see Chapter 3).

One way of improving the manufacturability of topology-optimized designs is to specify a minimum length scale requirement on the design features. The minimum length scale is generally defined as the minimum radius or diameter of the material phase of concern. For designs realized by an additive manufacturing approach, such as 3D printing or direct metal laser sintering (DMLS), one can consider the minimum length scale of the structural members to be dictated by minimum resolution of the used printer. Similarly for topologies fabricated by a material removal process, such as eg. CNC machining, the curvature and size of the holes in the design are dictated

by the drill size. However, currently most algorithms only considers a single phase of the design to be active in the design process and therefore undesirable features can occur in the uncontrolled, passive phase of the design. This is illustrated in Fig. 2.1 where an MBB beam has been designed with control of the (a) solid–, and (b) void phase (a full description of the MBB beam design problem is given in section 2.5). The undesirable features includes small scale voids and sharp corners when the solid phase is active such as those highlighted in Fig. 2.1a, and ultra-thin structural members when only the void phase is active as can be seen in Fig. 2.1b. The key focus of this chapter is therefore to improve the manufacturability of topology-optimized designs by controlling the minimum length scale of the topological features of both phases.

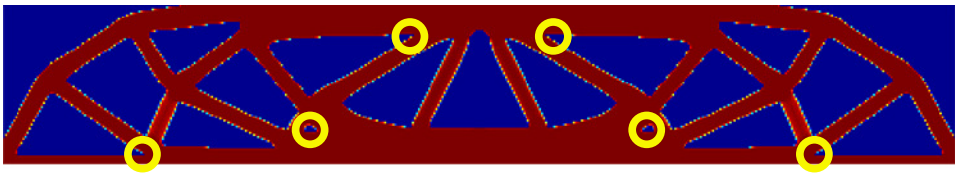

$d_{min,s}$

(a)

$d_{min,v}$

(b)

Figure 2.1: Examples of undesirable features in the non-controlled phase of topology-optimized MBB beams with minimum length scale control on (a) the solid phase and (b) the void phase.

CHAPTER 2. IMPROVED MANUFACTURABILITY BY LENGTH SCALE CONTROL

It is well established that controlling the minimum length scale has the additional advantage of circumventing numerical instabilities, such as checkerboard patterns and mesh dependency.[41,42] Sigmund[9,43] proposed a sensitivity filter to reduce numerical instabilities including checkerboard patterns.[44] Later it was suggested to use density filters.[45,46] Both of these filtering approaches suffer from the undesirable boundary effect where intermediate density (gray) elements exist along the boundary of the structure.

The initial efforts to restrict the minimum length scale of topology-optimized designs were based on formulating constraints on the gradient of the material distribution function. In Petersson and Sigmund[47] the change in element volume fraction between adjacent elements is limited to insure a smooth transition from solid to void material, but this again suffered from the gray boundary effect. Poulsen[48] suggested the MOLE (MOnotonicity based minimum LEngth scale) method, which restricts the number of discrete phase changes within a circular "looking glass" of radius r_{min}. The method is able of achieving 0-1 designs, however at a high computational expense due to the large number of local nonlinear constraints.

Controlling the minimum length scale through a nonlinear filter or projection was first suggested by Guest et al.[22] In the Heaviside Projection Method (HPM)[22] the minimum length scale control is achieved for one phase of the design through the use of a regularized Heaviside function that ensures a 0-1 design. The formulation suggested in[22] requires user specification of a single parameter β. A thresholding

Heaviside function was suggested by Xu et al.[49] to ensure volume preservation when using continuation methods for single phase designs, however it demands user specification of an additional parameter and the minimum length scale control is lost. Recently, filters based on geometric and the harmonic means as opposed to a weighted arithmetic mean have been suggested[50] and fast algorithms for filters based on a quasi-arithmetic mean over polytope-shaped neighborhoods on regular meshes have been developed.[51] These algorithms have the potential to be linked with projection algorithms to provide fast minimum length control.

Sigmund[23] suggested the morphology-based filtering approach to control the minimum length scale. In this method an erode (min) operation is performed when a void design variable is projecting within the minimum length scale r_{min}. Similarly, a dilate (max) operation is conducted when a solid design variable is projecting. The method uses successive filtering of design variables referred to as the open (max(min)) and close (min(max)) operators and is capable of achieving volume preservation. However, the successive filtering increases the complexity of the sensitivity analysis and as for single phase HPM, the minimum length scale is only satisfied for a single phase of the design. Wang et al.[52] proposed a robust morphology filter that allows for minimum length scale control of both the solid and void phases of a design and ensure mesh convergence. However, the proposed filter adds to the computational cost by having to solve three separate finite element problems per iteration and large iteration numbers. Zhou et al.[53] suggested to achieve two-phase minimum length scale control by a

combination of a thresholding Heaviside filter and cheap geometric constraints. The method has proved to be very sensitive to the user provided initial guess and requires significant parameter tuning. Lazarov and Wang[54] have extended the morphology-based filtering approach from[53] to restrict minimum and maximum length scales on both phases of the design. For more on maximum length scale restriction the reader is referred to.[55–59]

In Guest[60] it was proposed to control the minimum length scale of multiple phases by having multiple sets of design variables - one for each phase. All the design variables are projected independently onto the finite elements and combined to obtain the finial topology, using a standard intermediate density penalization scheme. While this seemed to perform well, the primary disadvantage of the approach was that the number of design variables increased by a factor of two. Although this could be mitigated using sparse design variable fields (e.g.[61]), this property was generally undesirable.

In this work, we propose to control the minimum length scale of two phases of a design by letting the magnitude of a single design variable determine which phase it projects actively onto the finite elements. This is done by letting the design variable pass through nonlinear weighting functions. This idea was recently proposed in Guest[62] where negative design variables indicated void projection and positive solid projection. The weighting functions, however, required user definition of three parameters that, for some problems, demanded significant tuning. Our goal here is

to develop a more stable algorithm and extend the formulation to give the design control of the maximum feature sizes.

2.2 The Heaviside Projection Method

In this work we use the Heaviside Projection Method (HPM)[22] to control the minimum length scale of topology-optimized designs because the operator of this method is capable of yielding 0-1 designs without additional explicit constraints on the problem. This section therefore gives a short review of the method used for multiple-phase projection in.[60]

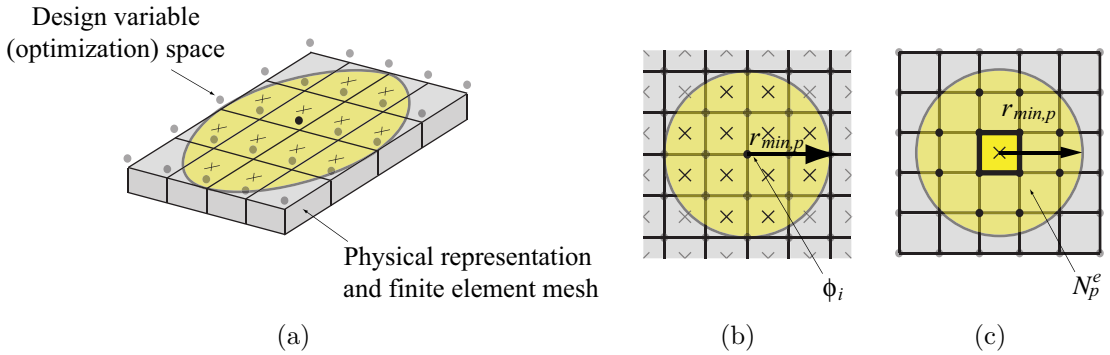

Figure 2.2: Schematic of (a) the two spaces of the topology optimization problem with the spheres symbolizing the design variable space and the blocks signifying the physical representation. Figure (b) shows the radial projection of the design variable ϕ_i onto the finite elements with $r_{min,p}$, and (c) gives the element perspective of the radial projection with an element e receiving design variable information from within the projection domain N_p^e.

In HPM the design variables ϕ_i are associated with a material phase and projected onto the finite elements by a Heaviside function. Figure 2.2 illustrates this separation

of the problem into a design variable space where the optimization is performed, and a finite element space where the physical equilibrium is solved. In Fig. 2.2a the design variables are illustrated by spheres and the finite elements by blocks. The location of the design variables can be arbitrarily chosen and herein it will coincide with the location of the finite element nodes. The connection between the two spaces is the projection which typically is done radially. In this work the actively projected phase will be denoted $p = s$ and $p = v$ for solid and void, respectively. The projection of the design variable ϕ_i in Fig. 2.2b will affect the volume fraction of all elements with centroids within the projection radius $r_{min,p}$. Therefore, the projection radius can easily be chosen as the prescribed minimum length scale. Fig. 2.2c shows HPM from the element perspective and illustrates how an element receives design variable information from all design variables ϕ_i within the projection domain N_p^e. For radial projection this domain contains all design variables within a distance $r_{min,p}$ of the element centroid $\bar{\mathbf{x}}^e$:

$$i \in N_p^e \quad \text{if } ||\mathbf{x}_i - \bar{\mathbf{x}}^e|| \leq r_{min,p} \tag{2.1}$$

where $\mathbf{x}_i$ is the location of design variable i.

The mapping onto the finite elements is done separately for each phase of each element by computing the weighted average of the design variables in the set N_p^e. For

the considered phase the weighted average μ_p^e is expressed as

$$\mu_p^e = \frac{\sum_{i \in N_p^e} w(\mathbf{x}_i - \bar{\mathbf{x}}^e) \cdot \phi_i}{\sum_{i \in N_p^e} w(\mathbf{x}_i - \bar{\mathbf{x}}^e)} \tag{2.2}$$

where $w(\mathbf{x}_i - \bar{\mathbf{x}}^e)$ is a linear weighting function that scales the information received by each design variable according to the design variable location. Typically either a uniform or a linear weighting is used.

To obtain binary solutions, nonlinear projection is used where the average design variables μ_p^e are passed through a Heaviside function to obtain the element volume fraction ρ_p^e. The element volume fraction is defined such that $\rho_p^e = 1$ means that an element is actively receiving projection from phase p:

$$\rho_p^e = 1 - e^{-\beta \mu_p^e} + \frac{\mu_p^e}{\mu_{max}} e^{-\beta \mu_{max}} \tag{2.3}$$

Here $\beta \geq 0$ dictates the curvature of the regularization which approaches the Heaviside function as β approaches infinity. Further, μ_{max} is the maximum value that μ_p can take.

The combined element volume fractions ρ_e are for each element assembled by averaging the element volume fractions from the projected phases.

$$\rho^e = \frac{\rho_s^e + (1 - \rho_v^e)}{2} \tag{2.4}$$

2.3 Two-Phase Projection with Nonlinear Weighting Functions

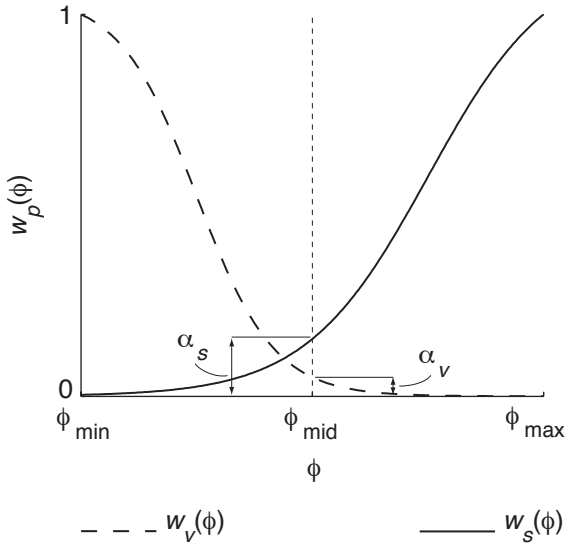

Figure 2.3: The nonlinear weighting functions $w_s(\phi)$ and $w_v(\phi)$ in the interval ϕ_{min} to ϕ_{max} for $\alpha_s = 0.15$ and $\alpha_v = 0.05$.

This work proposes to determine the actively projected phase by using nonlinear weighting functions. Instead of letting weighted average of the design variables μ_p^e be expressed by (2.2), it will now be defined as

$$\mu_p^e = \frac{\sum_{i \in N_p^e} w(\mathbf{x}_i - \bar{\mathbf{x}}^e) \cdot w_p(\phi_i)}{\sum_{i \in N_p^e} w(\mathbf{x}_i - \bar{\mathbf{x}}^e)} \tag{2.5}$$

where $w_p(\phi)$ is the nonlinear functions that the design variables are passed through. For the solid phase, the function values ranges from close to zero for the minimum

value of the design variable ϕ_{min}, to 1 at the maximum value ϕ_{max}. Similarly, the function value of void weighting function ranges from 1 at ϕ_{min} to close to zero at ϕ_{max}. At the mid of the range of the design variables ϕ_{mid}, the weighting function equals the constant α_p, that is chosen for each phase such that $\alpha_p \in (0, 1]$. Herein, the nonlinear weighting functions are taken as the hyperbolic tangent since it only requires user specification of a the parameters α_p. The nonlinear weighting functions are illustrated in Fig. 2.3 and defined by

$$w_s(\phi) = \frac{1+\alpha_s}{1+\alpha_s \cdot e^{2n_s(\phi_{max}-\phi)}} \tag{2.6}$$

$$w_v(\phi) = \frac{1+\alpha_v}{1+\alpha_v \cdot e^{2n_v(\phi-\phi_{min})}} \tag{2.7}$$

where $\phi_{range} = \phi_{max} - \phi_{min}$ and

$$n_p = -\frac{2\ln(\alpha_p)}{\phi_{range}} \tag{2.8}$$

The herein chosen definition of weighing functions $w_p(\phi_i)$ results in $\mu_{max} = 1$ which is used throughout.

2.4 Solution Algorithm

The topology optimization problem in Eq. (1.1) is solved with the proposed algorithm on a range of benchmark examples. This section provides the algorithmic

details used in the designs.

2.4.1 Penalization of Intermediate Densities

The Solid Isotropic Material with Penalization (SIMP) method[19] is used to guide the design to a 0-1 solution. Therefore the following expression relates the element stiffness matrices to the topology:

$$\mathbf{K}^e(\phi) = \big(\rho_e^\eta + \rho_{min}\big)\mathbf{K}_0^e \tag{2.9}$$

Here $\eta \geq 1$ is the exponent penalty term, $\mathbf{K}_0^e$ is the stiffness matrix of a pure solid element and ρ_{min}^e is a small positive number required to maintain positive definiteness of the global stiffness matrix. In this chapter, $\rho_{min}^e = 10^{-4}$ is used for elastic design problems and $\rho_{min}^e = 10^{-2}$ for thermal conduction problems.

The proposed two-phase projection formulation has also been tested using the Rational Material Penalization (RAMP) method[21] and for all examples similar observations were made for both penalization schemes.

2.4.2 Sensitivities

The sensitivities of the objective function are calculated as follows:

$$\frac{\partial f}{\partial \phi_i} = \sum_{e \in \Omega} \frac{\partial f}{\partial \rho^e} \frac{\partial \rho^e}{\partial \phi_i} \tag{2.10}$$

The partial derivative of the objective function f with respect to the element volume fraction ρ^e is problem dependent and calculated using the adjoint method. The partial derivative of the element volume fraction with respect to the design variables follows the chain rule. By differentiating Eq.s (2.3) and (2.4) the following expression is found:

$$\frac{\partial \rho^e}{\partial \phi_i} = \frac{1}{2}\left[\left(\beta e^{-\beta\mu_s^e} + e^{-\beta}\right)\frac{\partial \mu_s^e}{\partial \phi_i} - \left(\beta e^{-\beta\mu_v^e} + e^{-\beta}\right)\frac{\partial \mu_v^e}{\partial \phi_i}\right] \tag{2.11}$$

where the partial derivates of μ_s^e and μ_v^e are found by differentiating Eq.(2.5) for $p = s$ and $p = v$, respectively. In these, the sensitivities of the nonlinear weighting functions in Eq. (2.6-2.7) are as follows:

$$\frac{\partial w_s}{\partial \phi_i} = \frac{1+\alpha_s}{(1+\alpha_s \cdot e^{2n_s(\phi_{max}-\phi_i)})^2} \cdot 2\ \alpha_s n_s e^{2n_s(\phi_{max}-\phi_i)} \tag{2.12}$$

$$\frac{\partial w_v}{\partial \phi_i} = \frac{1+\alpha_v}{(1+\alpha_v \cdot e^{2n_v(\phi_i-\phi_{min})})^2} \cdot (-2)\alpha_v n_v e^{2n_s(\phi_i-\phi_{min})} \tag{2.13}$$

2.4.3 Optimizer

All problems are solved using the Method of Moving Asymptotes (MMA) as the optimization algorithm (,[6364]). A continuation method is applied to the SIMP exponent penalty to transform the problem from a relaxed, unpenalized state to the penalized, near discrete formulation. This is common practice in topology optimization as it is known to help avoid convergence to undesirable local minima. Herein, an increment of $\Delta\eta = 1.0$ is used. For the cantilever and the MBB beam problems no

continuation is applied to the Heaviside parameter[65] and a constant value of $\beta = 50$ is taken. The heat conduction and compliant mechanism design problems are solved using an incrementation on the Heaviside parameter of $\Delta\beta = 1.1^k$ where k is the iteration number. Further, it is used that $\beta_{max} = 50$. The reader is referred to[22] for detailed algorithmic steps. All problems are solved using four node quadrilateral elements, a uniform initial distribution of material, and $\phi_{min} = -1$ and $\phi_{max} = 1$.

The parameters used in the nonlinear weighting functions must be chosen small enough to allow the design variables at ϕ_{mid} to be inactive in both phases. In this work we have used $\alpha_s = 0.002$ and $\alpha_v = 0.0005$ for all examples. We have also tried other parameter combinations and found nearly identical results to those produced herein. It should be noted that the algorithm is more stable when α_s and α_v have slightly different magnitudes as this produces different sensitivities for the two phase.

Elasticity problems assume plane stress conditions as the depths of the design domains are much smaller than the lengths and widths. Young's modulus and Poisson's ratio are taken as $E = 1.0$ and $\nu = 0.3$, respectively. For the heat conduction problem the conductivity of the solid is set to $\kappa = 1.0$.

2.5 Numerical Examples

The proposed algorithm is tested on the benchmark examples of minimum compliance for the cantilever and MBB beams, the complaint inverter design problem

and the thermal heat conduction problem. The design domains for the four example problems are illustrated i Fig. 2.4.

The cantilever problem (Fig. 2.4a) has $L = 40$, $H = 25$ and $P = 1$, whereas the MBB problem (Fig. 2.4b) has $L = 60$, $H = 20$ and $P = 1$. For both problems, a volume constraint of $V_{max} = 50\%$ is used and, for the MBB beam problem, only the right half of the domain is designed.

The heat conduction problem (Fig 2.4c) is solved similarly to the minimum compliance problem where **d** represent the nodal temperatures instead of the nodal displacements. The domain is uniformly heated and zero temperature is prescribed along

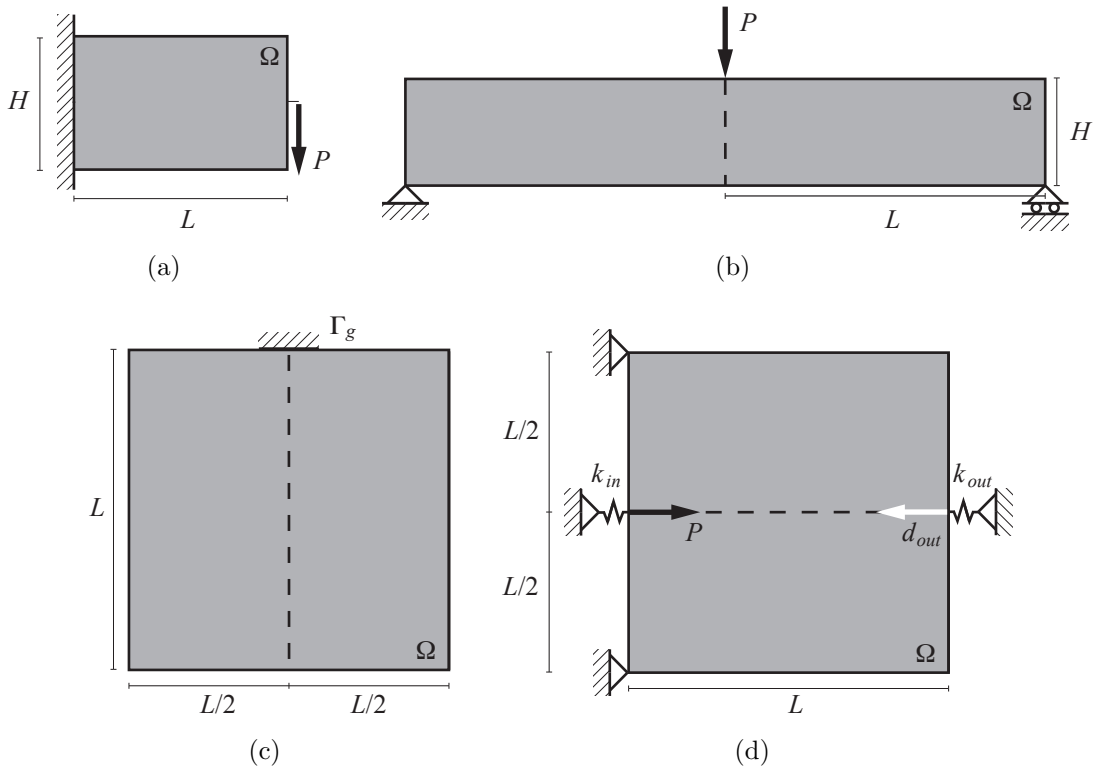

Figure 2.4: Design domains for (a) the cantilever beam–, (b) the MBB beam–, (c) the heat conduction–, and (d) the compliant mechanism design problem.

the middle 20% of the top boundary ($|\Gamma_g| = 0.2L$). The heat flux on the remaining boundaries is zero. We have used $L = 1$ unit and only the right half of the domain is designed.

The compliant inverter mechanism problem (Fig. 2.4d) is only designed for the bottom half of the domain. It is used that $L = 120$, $P = 1$, $V_{max} = 25\%$ and the spring stiffnesses are taken as $k_{in} = 1$ and $k_{out} = 10^{-3}$.

2.5.1 MBB and Cantilever Beams

The solution to the MBB beam problem is shown in Fig. 2.5 for a minimum length scale of $r_{min,p} = 1$ for (a) solid phase projection only, (b) void phase projection only, and (c) both solid and void projection using the herein proposed approach. The results are obtained on a 240×80 mesh, using a uniform weighting function and no continuation on the Heaviside parameter. It is clearly seen how the single phase projections does not provide control of the minimum length scale in the passive phase. In Fig. 2.5a this is evident by the sharp corners and in Fig. 2.5b by the slender members. In Fig. 2.5c the solution obtained using the improved two-phase projection is given and it is seen that the specified length scales are satisfied for both phases. However, it is seen to come at the cost of an increase in the intermediate density region. Further, we have found that to obtain crisp boundaries of the design it is necessary to drive the SIMP exponent higher than what is typically done, for this example to $\eta_{max} = 10$.

Fig. 2.6a and b shows the obtained topologies for the cantilever beam problem. The designs are obtained with uniform weighting, $\eta_{max} = 7$ and improved two-phase projection on two meshes. It is easily seen that mesh insensitivity is fulfilled for this problem. In Fig. 2.6d the design variable distribution for the fine mesh topology (Fig. 2.6b) is given. It is seen that the design variables do not provide a strict ϕ_{max} and ϕ_{min} distribution, but that this is irrelevant since the projection onto the finite elements results in a 0-1 density distribution (Fig 2.6d). Moreover, it is seen that a

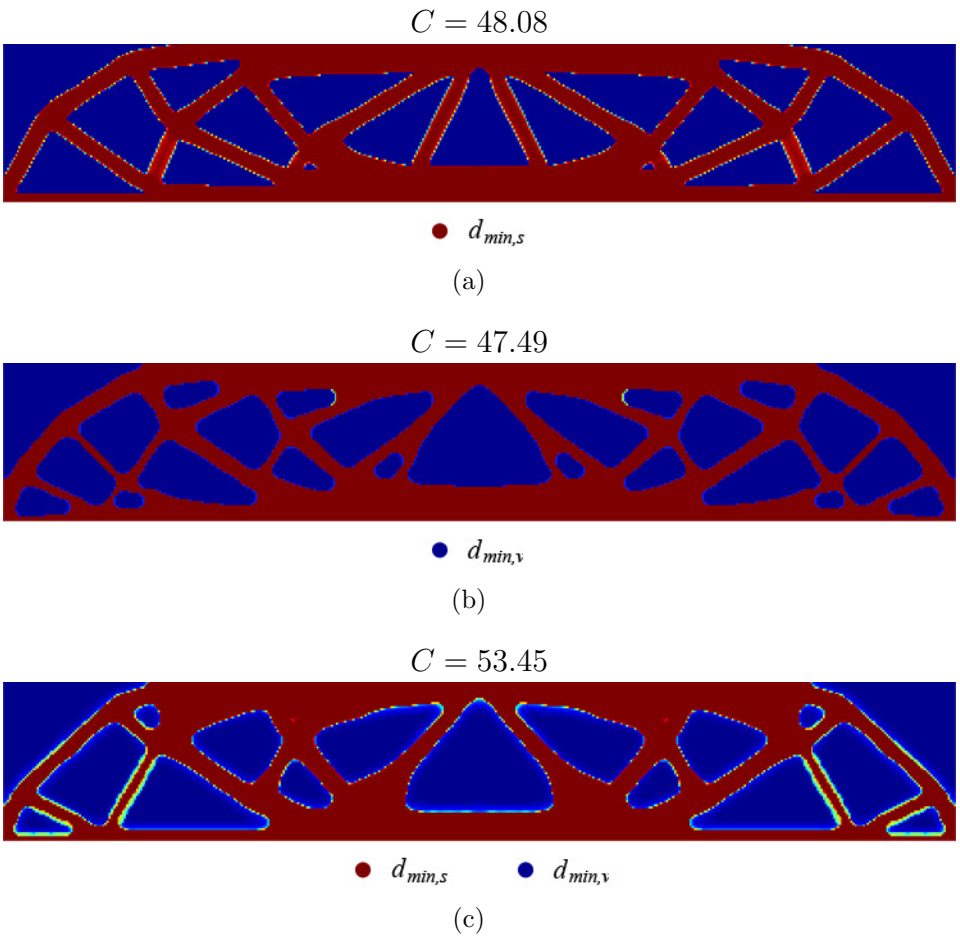

Figure 2.5: MBB beam designs with $r_{min,p} = 1$ for (a) solid projection, (b) void projection, and (c) improved two-phase projection.

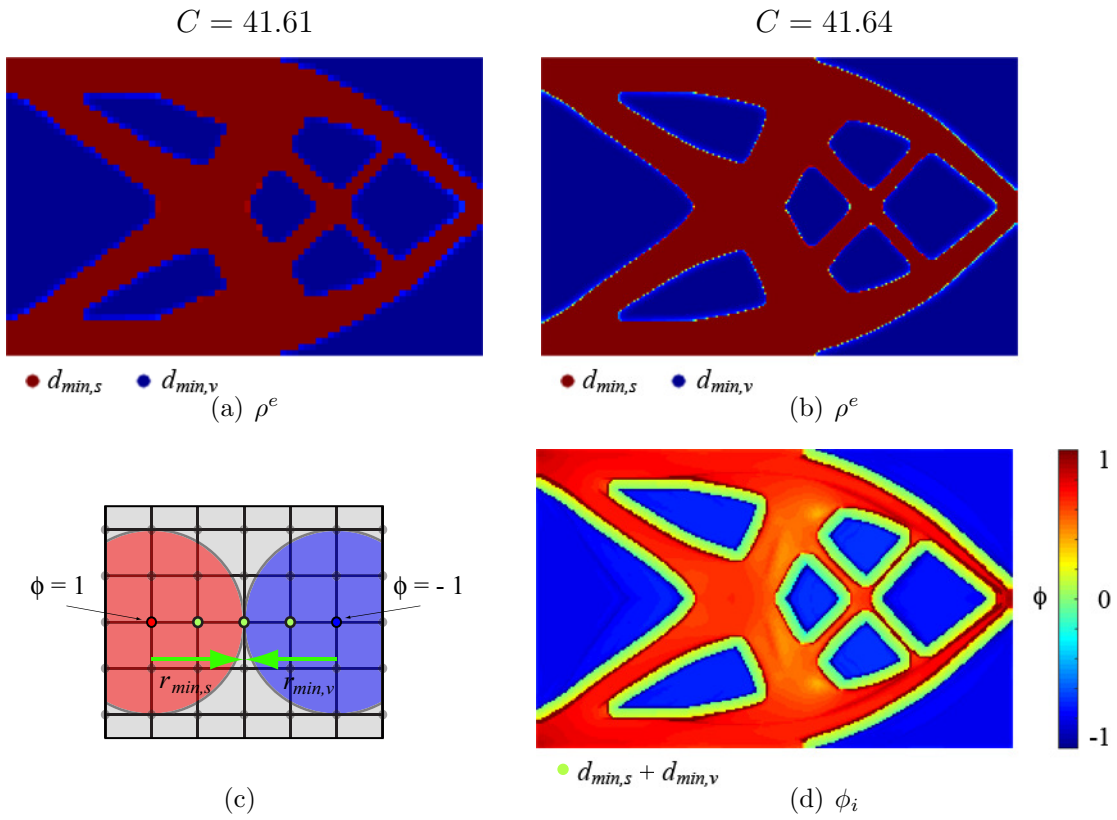

Figure 2.6: Element volume fraction distributions (ρ^e) obtained for the cantilever problem with $r_{min,s} = r_{min,v} = 0.5$ on a (a) 80×50 mesh, and a (b) 240×150 mesh. Figure (c) illustrates how a $r_{min,s} + r_{min,v}$ layer of non-projecting design variables is needed for a crips boundary, and (d) gives the design variable distribution (ϕ_i) for the topology in (b).

layer of design variables of magnitude ϕ_{mid} is located around the edges of the design. This layer of size $r_{min,s} + r_{min,v}$ is necessary for a crisp boundary. The illustration in Fig. 2.6c shows two actively projecting design variables (the red and the blue node in the mesh) that create a crisp boundary because the design variables between them not are actively projecting. The non-projecting design variables are in this figure indicated by a green color.

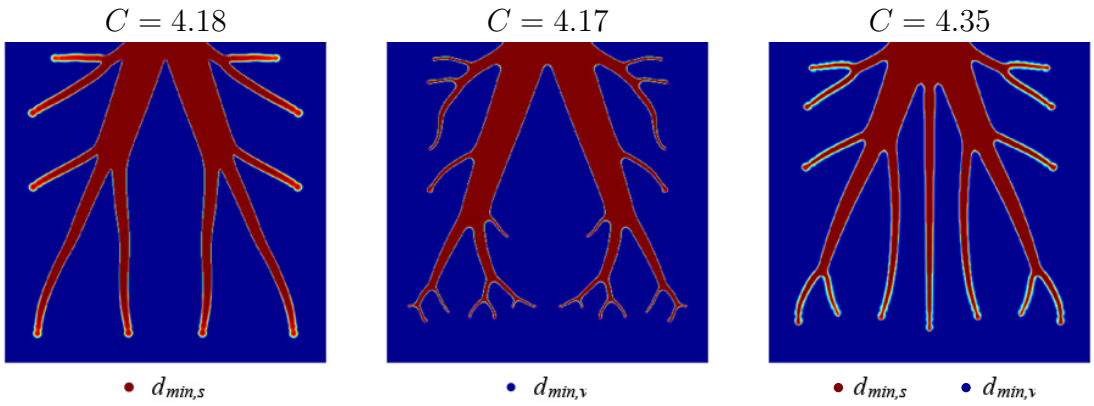

Figure 2.7: Results of the heat conduction problem with $r_{min,p} = 0.015$ for (a) solid projection, (b) void projection, and (c) the new two-phase projection.

2.5.2 Heat Sink

In Fig. 2.7 the results of the heat conduction problem are given for projection of (a) the conductive (solid) phase only, (b) the non-conductive (void) phase only, and (c) both phases. The results are obtained on a 200×400 mesh, with a minimum length scale of $r_{min,p} = 0.015$ and a volume constraint of $V_{max} = 20\%$. A linear proximity based weighing function has been used and the SIMP exponent has for these designs been driven to $\eta_{max} = 7$. As expected, it is seen that the results resemble root structures where the conductive phase is collecting the heat load though thin arms. The results for this example also clearly illustrates how sharp corners appear when the conductive (solid) phase is actively projected and very thin arms when active projection only is performed on the non-conductive (void) phase. It is seen in Fig. 2.7c that the two-phase projection fulfill both length scale requirements.

The proposed algorithm does not require the prescribed minimum length scale of

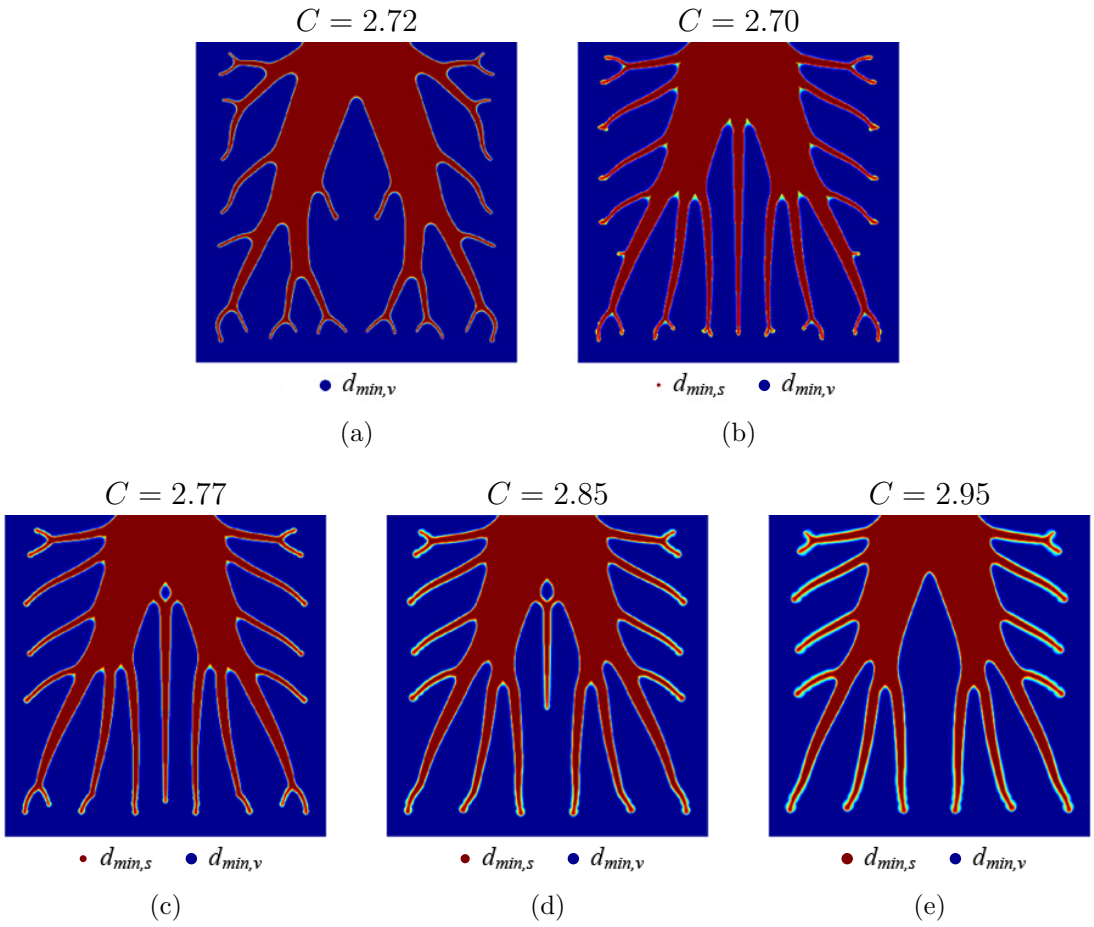

Figure 2.8: Topologies obtained for the heat conduction problem with $r_{min,v} = 0.02$ and (a) $r_{min,s} =$ NA, (b) $r_{min,s} = 0.005$, (c) $r_{min,s} = 0.01$, (d) $r_{min,s} = 0.015$, and (e) $r_{min,s} = 0.02$.

the two phases to be equal. Fig 2.8 gives the results of the heat conduction problem for a range of different prescribed length scales on the conductive (solid) phase. To obtain the designs a linear proximity based weighting function has been used and a minimum length scale of $r_{min,v} = 0.020$ has been specified for the non-conductive (void) phase. The volume constraint was set at $V_{max} = 30\%$ and the SIMP exponent driven to $\eta_{max} = 7$. By comparison of the results in the figure it is clearly seen that the length

scale of the conductive (solid) phase varies while the radius of the corners maintain the same radius $r_{min,v} = 0.020$. The figure also reveals that this design problem tends to form triangularly shaped features of intermediate densities in the corners of the topology (see Fig. 2.8b-d) when the minimum length scale of the conductive (solid) phase is smaller than the minimum length scale of the non-conductive (void) phase.

2.5.3 Compliant Inverter Mechanism

The results of the compliant inverter mechanism design is given in Fig. 2.9. For these results an initial guess of $\phi_{init} = -0.3$ snd a linear proximity based weighting function were used. The design was conducted on a 240×120 mesh and $\eta_{max} = 5$ was found to be sufficient. For the two-phase projection with $r_{min,s} = r_{min,v} = 4.0$ (Fig 2.9a), it is seen that length scale requirements are fulfilled, however that large areas of intermediate densities occurs around the hinges of the design. It should be noted that the inverter mechanism benchmark examples are well known to create artificially stiff one node hinges unless a robust topology optimization formulation is used.[23,24] When decreasing the void radius to $r_{min,v} = 2.0$ (Fig 2.9b) smaller intermediate density regions are found in the hinge areas.

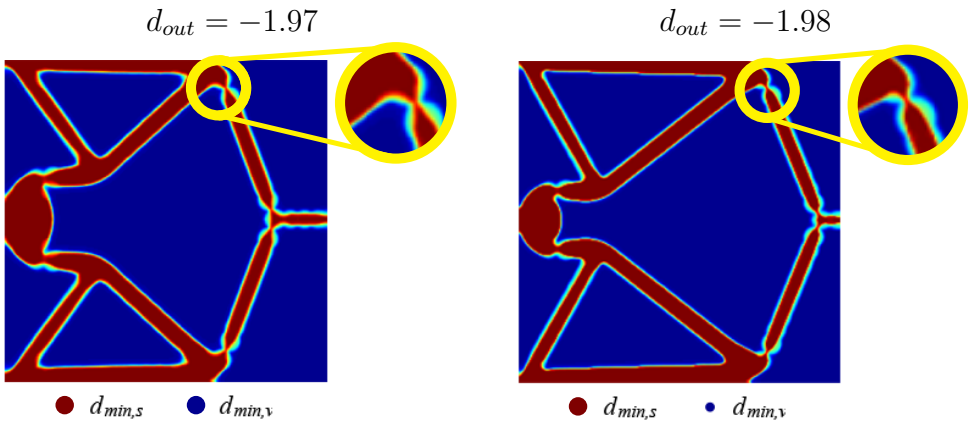

(a) (b)

Figure 2.9: Compliant inverter mechanism designs obtained with $r_{min,s} = 4.0$ and (a) $r_{min,v} = 4.0$, and (b) $r_{min,v} = 2.0$.

2.6 Maximum Length Scale on the Solid Phase

An ongoing work is the extension of the two-phase projection algorithm to maximum feature size control. The extension is done by creating an additional projection domain for the maximum length scale of the considered phase. From Eq. (2.4) it is evident that a solid element will only be created if the solid phase is actively projecting and the void phase is passively projecting ($\rho_s^e = 1$ and $\rho_v^e = 0$). For a maximum length scale $r_{max,s}$ to be enforced on the solid phase, the element must additionally be within a radius of $r_{max,s} + r_{min,v}$ from a design that is variable actively projecting void. This can be expressed by the neighborhood

$$i \in N^e_{r_{max,s}} \quad \text{if } ||\mathbf{x}_i - \bar{\mathbf{x}}^e|| \leq r_{max,s} + r_{min,v} \tag{2.14}$$

By this neighborhood and additional void projection ρ_{xv}^e can be performed. This projection must be active ($\rho_{xv}^e = 1$) to create a solid element, since it implies that a void is present within a radius of $r_{max,s} + r_{min,v}$. If a void is not detected within this distance ($\rho_{xv}^e = 0$), then the element volume fraction should encourage the optimizer to change the design. For all other combinations of ρ_s^e, ρ_v^e and ρ_{xv}^e the resulting element volume fraction should be similar to Eq. (2.4). To accommodate the inclusion of the maximum length scale on the solid phase, the following expression is proposed for the element volume fraction:

$$\rho^e = \frac{\rho_s^e + (1 - \rho_v^e)}{c_{r_{min}}} - \frac{\rho_s^e(1 - \rho_v^e)(1 - \rho_{xv}^e)}{c_{r_{max,s}}} \tag{2.15}$$

The sensitivity of Eq. (2.15) is

$$\begin{aligned} \frac{\partial \rho^e}{\partial \phi_i} = & \left(\frac{1}{c_{r_{min}}} - \frac{(1 - \rho_v^e)(1 - \rho_{xv}^e)}{c_{r_{max,s}}} \right) \frac{\partial \rho_s}{\partial \mu_s} \frac{\partial \mu_s}{\partial \phi_i} \\ - & \left(\frac{1}{c_{r_{min}}} - \frac{\rho_s^e(1 - \rho_{xv}^e)}{c_{r_{max,s}}} \right) \frac{\partial \rho_v}{\partial \mu_v} \frac{\partial \mu_v}{\partial \phi_i} + \frac{\rho_s^e(1 - \rho_v^e)}{c_{r_{max,s}}} \frac{\partial \rho_{xv}}{\partial \mu_{xv}} \frac{\partial \mu_{xv}}{\partial \phi_i} \end{aligned} \tag{2.16}$$

In Tab. 2.1 some combinations of ρ_s^e, ρ_v^e and ρ_{xv}^e are given along with the element volume fractions computed by Eq. (2.4) and Eq. (2.15). It is seen that the only difference is found in combination b, where Eq. (2.15) ensures that a solid element cannot be created if no void is detected within $N_{r_{max,s}}^e$.

Table 2.1: Combinations of ρ_s^e, ρ_v^e and ρ_{xv}^e and the resulting ρ^e from Eq. (2.4) and Eq. (2.15) with $c_{r_{min}} = 2.0$.

Combination	ρ_s^e	ρ_v^e	ρ_{xv}^e	Eq. (2.4)	Eq. (2.15)
a	1	0	1	1	1
b	1	0	0	1	$1 - 1/c_{r_{max,s}}$
c	1	1	1	0.5	0.5
d	1	1	0	0.5	0.5
e	0	0	1	0.5	0.5
f	0	0	0	0.5	0.5
g	0	1	1	0	0
h	0	1	0	0	0

2.6.1 Cantilever Beam

In Fig. 2.10 the solution to the cantilever beam problem with two-phase minimum length and maximum length scale control on the solid phase. The results are obtained on a 80×50 mesh with $r_{min,s} = r_{min,v} = 0.5$ and maximum length scale requirements of (a) $r_{max,s} = 2.0$, (b) $r_{max,s} = 3.0$ and (c) $r_{max,s} = 6.0$. These are compared with (d) the two-phase solution. A uniform weighting function is used, a constant Heaviside parameter is taken for the maximum length scale projection as $\beta_x = 15$ and the SIMP exponent is driven to $\eta_{max} = 15$. Further, due to the increased nonlinearity of the objective function, it was necessary to tigthen the MMA optimizer such that $s_0 = 1/(2\beta + 1)$ and $raa0 = 0.0001$. From the figure it is clearly seen that the applied maximum length scale and both minimum length scales are fulfilled for the

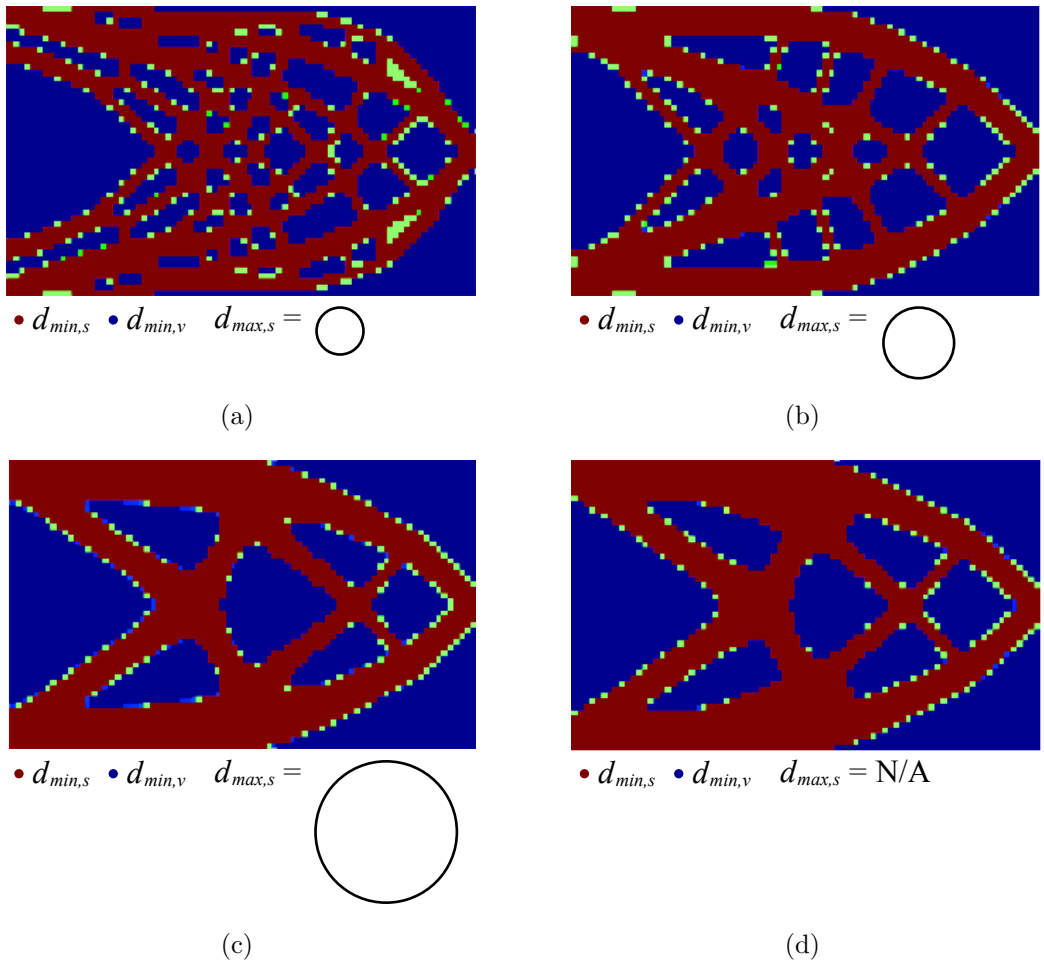

Figure 2.10: Distribution of the volume fraction ρ^e found for the cantilever beam problem with $r_{min,s} = r_{min,v} = 0.5$, $a_s = 0.0005$, $a_v = 0.002$ and $a_{xv} = 0.001$, $\beta_x = 15$, $c_{r_{max}} = 1.90$ and $\eta_{max} = 15$ on a 80×50 mesh with (a) $r_{max,s} = 2.0$, (b) $r_{max,s} = 3.0$, (c) $r_{max,s} = 6.0$ and (d) $r_{max,s} = \text{NA}$.

optimized designs. However, it is evident that that the intermediate density region is larger for more restricted designs when r_{max} is close to $r_{min,p}$. In Tab. 2.2 the obtained objective functions for the designs in Fig. 2.10 are listed. It is seen that the compliance decreases as the maximum length scale is increased and approaches the two-phase results when the applied maximum length scale is larger than the greatest

Table 2.2: Compliances obtained with $\eta = 1$ and $\eta = 15$ for the cantilever beam designs with maximum length scale control in Fig. 2.10.

$d_{max,s}$	Fig. 2.10	$C(\eta = 1)$	$C(\eta = 15)$
4.0	a	41.8	48.0
6.0	b	38.3	42.0
12.0	c	37.6	39.9
N/A	d	37.7	39.8

feature size in the two-phase solution.

It should be noted that this is ongoing work as significant parameter tuning has been necessary to obtain the designs in Fig. 2.10. Therefore it is currently difficult to obtain quality solutions to problems with more nonlinear design spaces than the cantilever beam. Du to the multiplication term in Eq. (2.15), the sensitivities in Eq. (2.16) are typically very small for large design variable ranges. This makes it difficult for the optimizer to move. The RAMP[21] interpolation scheme generally has better performance than SIMP for low sensitivities, however, using RAMP has not had a significant effect on the needed amount of tuning.

2.7 Summary

A technique is proposed for restricting the minimum length scale of multiple phases in topology optimization. This allows the designer to prescribe a minimum allowable length scale for both the solid (structural or conductive) phase and the void (or non-

conductive) phase, and these length scales need not be equivalent. This is achieved by actively projecting both solid and void phases from each design variable. This is in contrast to the previous work by Guest[60] which used independent design variables associated with each specific phase, thereby doubling the number of design variables. The effect is achieved here using nonlinear weighting functions. These weighting functions are structured such that the design variable magnitude indicates whether solid phase or the void phase is actively projected. This maintains constant dimensionally of the design variable space, while allowing active projection and therefore length scale control of both phases. The disadvantage of the proposed approach is that the weighting functions are now design variable dependent and nonlinear. This could potentially make it more challenging for the optimizer to identify quality solutions, although our preliminary results indicate this is not necessarily the case. Ongoing work is the extension to maximum feature size control.

Chapter 3

Elastic Cellular Materials with Multiple Base Solids

3.1 Introduction

The recent development of manufacturing technologies (including additive manufacturing) has increased the interest in high performance engineered materials such as periodic cellular materials because fabrication is now possible for increasingly complex topologies. Here, cellular materials refers to periodic materials with a unit cell that is repeated throughout. Well known examples of period cellular materials include honeycomb topologies and materials that can be characterized as microtruss or microlattices. Although generally well performing, it should be noted that these well know examples of cellular topologies have not been designed by a rigorous optimiza-

tion method. In fact, recent work using ultrahigh resolution topology optimization has shown that lattice structures are not optimal for stiffness objectives at any length scale including the material architecture level.[66] This result motivates further the use of topology optimization as a rigorous design approach for cellular materials that can leverage the new manufacturing capabilities.

Cellular material design using topology optimization, or so-called inverse homogenization, is schematically illustrated in Fig. 3.1. Contrarily to homogenization problems where the effective material properties are estimated by analyzing a given unit cell, the inverse homogenization problem seeks to design a unit cell for some given effective properties. Figure 3.1a shows how the characteristic unit cell is defined as the design domain Ω. The unit cell topology that is achieved by solving the inverse problem is exemplified in Fig. 3.1b and Fig. 3.1c illustrates how an upscaling technique is required to connect the unit cell topology to the effective material properties.

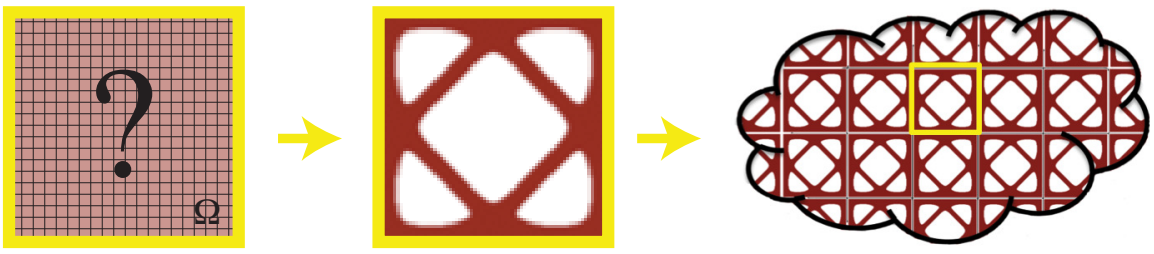

(a) (b) (c)

Figure 3.1: Schematic of topology optimization for cellular materials; (a) the unit cell design domain, (b) the optimized unit cell topology, and (c) the unit cell in the effective bulk material.

CHAPTER 3. ELASTIC CELLULAR MATERIALS WITH MULTIPLE BASE SOLIDS

Already in the pioneering work by Sigmund[43] it was shown that topology optimization can be used to design periodic cellular materials with optimized linear properties via inverse homogenization. Sigmund tailored the elasticity tensor using 2D truss, frame and continuum elements to achieve a range of properties including negative Poisson's ratio.[6,7,43] Andreassen et al.[67] considered manufacturing constraints and used an ultrahigh resolution for the design of 3D cellular materials, including an isotropic material designed for a Poisson's ratio of $\nu = -0.50$. Without post-processing a sample was fabricated with an SLS 3D printer and experimentally found to have a Poisson's ratio of $\nu = -0.50 \pm 0.03$. Other examples of topology-optimized cellular materials that have been fabricated and tested include the additively manufactured bone implant scaffolds by Challis et al.[68] and the three dimensional woven porous lattices that have been designed under weaving constraints for stiffness–permeability.[69–71] Upon numerical and experimental investigation of the woven lattices they have been found to lie between free-form topologies and stochastic foams, both in terms of performance and manufacturing cost.

In addition to the above mentioned examples, numerous researchers have developed topology optimization algorithms that tailor cellular materials to a broad range of linear properties including thermoelastic,[8,9] piezoelectric,[10,11] fluid permeability,[12–14,72] and stiffness–thermal conductivity.[15,73] A thorough assessment of all published work on the topic is beyond the scope of this chapter and the reader is referred to the review papers by Cadman et al.[4] and Osanov and Guest.[5] It is note-

worthy that most algorithms only consider design with a single base material. Several 3D printing technologies can now deposit multiple materials adjacent to each other in complex topologies and this chapter therefore seeks to extend topology optimization to cellular material design with multiple base materials.

Bendsøe and Sigmund[40] proposed a SIMP-based interpolation model for topology optimization with multiple base materials and demonstrated it on a minimum compliance example. The methodology uses multiple sets of design variables (one per solid material phase) and requires multiplication to combine them. Gaynor et al.[24] proposed a combinatorial SIMP approach that also uses multiple sets of design variables but relies on summation for the combination. Gaynor et al.[24] used both multimaterial formulations ([24,40]) to design robust compliant inverter mechanisms.[74] The designs were fabricated by a PolyJet 3D printing process with a 2:1 material stiffness ratio and mechanical testing showed improvements of $45\% - 85\%$ over the single phase design. It should be noted that the large variation in the obtained performance could be influenced by quality of the identified local minima in the highly nonlinear design space for the complaint inverter problem. Yin and Ananthasuresh[75] proposed a multimaterial topology optimization algorithm that uses a single design variable space to design compliant inverter mechanisms. The suggested methodology uses a normal distribution function to convert the continuous design problem into one with more discrete material choices. As the algorithm progresses, the normal function is contracted so that additional peaks begin to appear at the locations of the candidate

material options. The goal is to guide each design variable to one of these peaks and thereby obtain a discrete material distribution. However, besides adding nonlinearity to the design problem and making it more difficult to obtain quality solutions, the design variables are not necessarily driven to the value at the top of a peak and therefore intermediate stiffness values may still appear in the final result. Recently, Watts and Tortorelli[76] have proposed a multimaterial thresholding interpolation rule to be used in combination with SIMP[19] or RAMP.[21]

Sigmund and Torquato[9] were the first to use inverse homogenization to design multimaterial periodic cellular topologies using the formulation from[40] and specifying the volumes of each material phase. However the used approach did discretely account for the different base materials. Three-phase 2D topologies were designed with maximized, zero and minimized thermal expansion. The negative thermal expansion design was recently extended to high resolution 3D.[77,78] Watts and Tortorelli[79] used their multimaterial framework from[76] with RAMP to design 3D unit cells for minimized thermal expansion coefficients with three discrete material phases. Gibiansky and Sigmund[80] used the same formulation to design three-phase 2D topologies with maximized bulk modulus for a range of volume constraint combinations and with square and isotropic symmetry constraints. The designed topologies were in good agreement with the theoretical Hashin–Shtrikman[81] and Walpole[82] bound and therefore proved that the bound is attainable in a much wider range than it was previously believed. An additional effort on cellular topology design with multiple solid base

materials is the work by Ha and Guest[33] on periodic materials with discrete inclusions. Using a projection-based methodology stiff inclusions are placed in a compliant matrix or compliant inclusions are placed in a stiff matrix. The proposed methodology allows for different inclusion sizes, shapes and minimum spacings. The inclusions must however be discrete non-overlapping objects and only the layout of the inclusions is designed. The extension recently proposed by Koh and Guest[34] allows for design of the the discrete object layout as well as the matrix topology, but has yet to be implemented for cellular design problems.

The current chapter presents a topology optimization algorithm that allows for inverse homogenization with multiple base materials. The algorithm uses the multiple material formulation from[24] and allows for two types of volume constraints: (i) a specified total volume constraint with no requirement on the distribution of the material phases, and (ii) volume constraints specified on each material phase. The chapter focuses on 2D design but the methodology is extendable to three dimensions. The chapter has three main sections where the first describes the inverse homogenization topology optimization approach that is generally used for period cellular material design with linear properties. This is followed by a section that gives the topologies obtained with two base materials for a range of mechanical properties and for multiobjectives in stiffness and thermal conduction. The third main section of the chapter extends the inverse homogenization formulation to allow for multimaterial design and gives several topologies to demonstrate the algorithm.

3.2 The Inverse Homogenization Problem

As mentioned, most approaches considers the unit cell as the design domain for topology optimization of periodic cellular materials. A typical problem formulation is as follows:

$$\begin{aligned}
\underset{\phi}{\text{minimize}} \quad & f(\mathbf{C}^H(\phi, \mathbf{d}^{(i)})) \\
\text{subject to} \quad & \mathbf{K}(\phi)\mathbf{d}^{(i)} = \mathbf{f}(\phi)^{(i)} \quad \forall \quad i \\
& g\big(\mathbf{C}^H(\phi, \mathbf{d}^{(i)})\big) \geq g_{min} \\
& \sum_{e \in \Omega} \rho_e v_e \leq V_{max} \\
& \phi_{min} \leq \phi_n \leq \phi_{max} \quad \forall \quad n \in \Omega \\
& \mathbf{d}^{(i)} \quad \text{is } \Omega\text{-periodic}
\end{aligned} \tag{3.1}$$

Here f is the objective function that can be chosen as some (negative if maximizing) effective property such as Young's–, shear– or bulk modulus or Poisson's ratio. Further, ϕ are the design variables and $\mathbf{K}(\phi)$ is the global stiffness matrix. The constraints are defined by g with allowable magnitude g_{min}. A typical constraint, for example, is elastic symmetry of the effective material, which is usually chosen as either square symmetric or isotropic. The volume of element e is denoted v_e and ρ_e is the element density. The bounds on the volume fraction are defined by V_{max} and ϕ_{min} and ϕ_{max} describes the design variable bounds that in this chapter are taken as 0 and 1. An upscaling law is required to relate the unit cell mechanics to the effective material level. For linear properties numerical homogenization can be used to evalu-

ate the homogenized constitutive matrix $\mathbf{C}^H$. A numerical homogenization approach is described in the following section. The used approach is based on applying test strain fields to the unit cell and in Eq. (3.1) $\mathbf{d}^{(i)}$ and $\mathbf{f}^{(i)}$ refers the displacements and force vectors associated with test strain fields (i).

3.2.1 Numerical Homogenization

When numerical homogenization is used to solve Eq. (3.1) it aims at determining the components of the effective or homogenized constitutive matrix $\mathbf{C}^H$. For a linear elastic homogeneous material the stress tensor is symmetric ($\sigma_{ij} = \sigma_{ji}$) and therefore the constitutive matrix must also be symmetric $C^H_{ij} = C^H_{ji}$.[83] As a result, the constitutive matrix for the mechanical properties in 2D can be written as:

$$\mathbf{C}^H_{\mathrm{2D}} = \begin{bmatrix} C^H_{11} & C^H_{12} & C^H_{13} \\ C^H_{12} & C^H_{22} & C^H_{23} \\ C^H_{13} & C^H_{23} & C^H_{33} \end{bmatrix} \tag{3.2}$$

The numerical homogenization used herein is performed by applying test strain fields $\epsilon^{0(i)}$ to the unit cell as described in.[84–87] Due to the symmetry of $\mathbf{C}^H_{\mathrm{2D}}$ in Eq. (3.2), it is sufficient to apply three test strain fields for mechanical properties in 2D. The test fields separately considers a normal strain state in the x_1- and x_2-directions

and a state of pure shear:

$$\epsilon^{0(11)} = \begin{bmatrix} 1 \\ 0 \\ 0 \end{bmatrix}, \quad \epsilon^{0(22)} = \begin{bmatrix} 0 \\ 1 \\ 0 \end{bmatrix}, \quad \epsilon^{0(12)} = \begin{bmatrix} 0 \\ 0 \\ 1 \end{bmatrix} \tag{3.3}$$

Since a discretized numerical method is used, the test strain fields in Eq. (3.3) are applied as displacement fields $\mathbf{d_0}^{(i)}$ in the analyses. The boundary conditions on the unit cell are taken as in Hassani and Hinton[86] and illustrated in Fig. 3.2 for (a) the normal strain state test fields $\epsilon^{0(11)}$ and $\epsilon^{0(22)}$, and (b) the pure shear state test field $\epsilon^{0(12)}$. The numerical analysis of test field (i) results in the nodal displacement

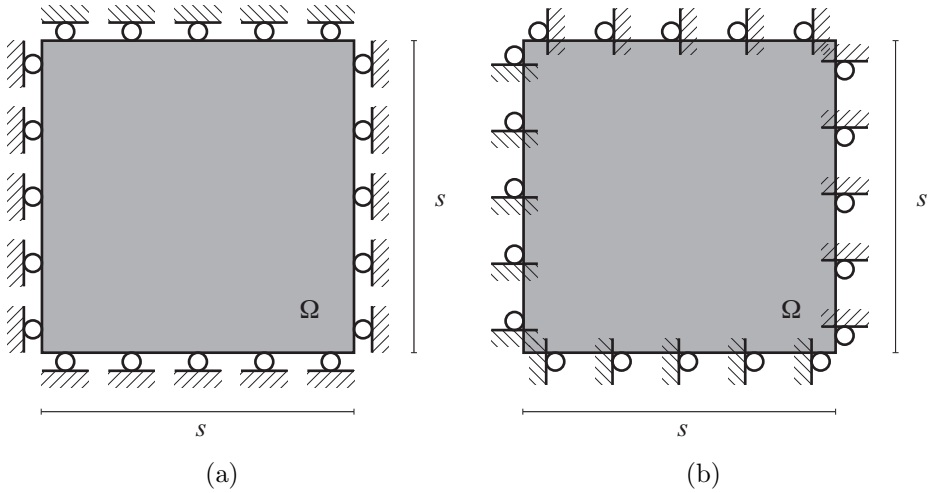

Figure 3.2: Boundary conditions applied in numerical homogenization of a 2D unit cell for (a) the normal test strain fields $\epsilon^{0(11)}$ and $\epsilon^{0(22)}$, and (b) the pure shear test strain field $\epsilon^{0(12)}$.

vector $\mathbf{d}^{(i)}$. The element contributions to the strain energy q^e_{ij} can be calculated from

the nodal displacement vectors:

$$q_{ij}^e = \frac{1}{|\Omega|}\left(\mathbf{d_0}^{e(i)} - \mathbf{d}^{e(i)}\right)^{\mathbf{T}} \mathbf{K}^e \left(\mathbf{d_0}^{e(j)} - \mathbf{d}^{e(j)}\right) \tag{3.4}$$

In Eq. (3.4) $\mathbf{d}_0^{e(i)}$ and $\mathbf{d}^{e(i)}$ are the applied and resulting nodal displacements for element e that corresponds to the test field (i) and $\mathbf{K}^e$ is the element stiffness matrix. The element contributions to the strain energies are normalized by the size of the unit cell which in this work is equal to the design domain Ω. The components of the effective constitutive matrix are found as the sum of all element contributions to the strain energy within the unit cell:

$$C_{ij}^H = \sum_{e \in \Omega} q_{ij}^e \tag{3.5}$$

3.2.2 Mechanical Properties and Symmetry

The mechanical properties and symmetry conditions of the effective material can be expressed in therms of the effective constitutive matrix components C_{ij}^H. In the topology optimization problem in Eq. (3.1) these expressions typically appear as the objective and/or the constraints.

3.2.2.1 Symmetry Constraints on the Constitutive Matrix

For most applications it is desirable to design material topologies with specific symmetry conditions such as square symmetry or isotropy. The symmetry conditions will constrain the component values in the homogenized constitutive matrix. For example, for a 2D homogeneous material to exhibit a square symmetric behavior, it is required that $C_{13} = C_{23} = C_{31} = C_{32} = 0$ and $C_{11} = C_{22}$.[83] The constitutive matrix from Eq. (3.2) therefore reduces to

$$\mathbf{C}^H_{\text{2D, } sq} = \begin{bmatrix} C_{11} & C_{12} & 0 \\ C_{12} & C_{11} & 0 \\ 0 & 0 & C_{33} \end{bmatrix}$$

Several error function formulations have been suggested for square and cubic symmetry constraints.[12,43,88] In this work we have used the following formulation from:[12,88]

$$error_{sq} = (C^H_{11} - C^H_{22})^2 + (C^H_{13})^2 + (C^H_{23})^2 \tag{3.6}$$

Some applications require that the homogenized material has the same material properties in all direction and that it thus exhibits isotropic behavior. Isotropy is a constrained variant of cubic or square symmetric behavior. In 2D an isotropic material therefore has the requirements of square symmetry $C_{13} = C_{23} = C_{31} = C_{32} = 0$ and $C_{11} = C_{22}$, and the additional requirement that $C_{33} = \frac{1}{2}(C_{11} - C_{12})$,[83] resulting in

the following constitutive matrix:

$$\mathbf{C}^H_{\text{2D, } iso} = \begin{bmatrix} C^H_{11} & C^H_{12} & 0 \\ C^H_{12} & C^H_{11} & 0 \\ 0 & 0 & \frac{1}{2}(C^H_{11} - C^H_{12}) \end{bmatrix}$$

In this work we have taken the error formulation from[88] for isotropic symmetry in 2D:

$$error_{iso} = error_{sq} + \left(C^H_{11} - (C^H_{12} + 2C^H_{33})\right)^2 + \left(C^H_{22} - (C^H_{12} + 2C^H_{33})\right)^2 \tag{3.7}$$

When solving the topology optimization problem in Eq. (3.1) in this work, we have applied the symmetry error functions as an explicit constraint and normalized by the square of the objective value f to prevent trivial solutions.

$$error = \frac{error_{sym}}{f^2} \tag{3.8}$$

Here $error_{sym} = error_{sq}$ or $error_{sym} = error_{iso}$ for square and isotropic symmetry, respectively.

3.2.2.2 Homogenized Mechanical Properties

The elastic mechanical properties such as the bulk– B^H, Young's– E^H and shear modulus G^H and the Poisson's ratio ν^H can be expressed in terms of the components

of the homogenized constitutive matrix $\mathbf{C}^H$. As all topology optimization designs in this work are 2D and has at least a square symmetry requirement, the derivations in this section are, for simplicity, performed with $\mathbf{C}^H = \mathbf{C}^H_{\text{2D, } sq}$. For all derivations it is necessary to recall Hooke's law that describes the stresses in terms of the the strains and components of the constitutive matrix:

$$\sigma_{11} = C_{11}\epsilon_{11} + C_{12}\epsilon_{22} \tag{3.9}$$

$$\sigma_{22} = C_{12}\epsilon_{11} + C_{22}\epsilon_{22} \tag{3.10}$$

$$\tau_{12} = C_{33}\epsilon_{12} \tag{3.11}$$

Bulk Modulus

The bulk modulus is defined as the ratio of the hydrostatic stress to the relative volume change. A state of hydrostatic stress where $\sigma_{11} = \sigma_{22} = \sigma$ is therefore applied.

$$B = \frac{\sigma}{\Delta V/V} = \frac{\sigma}{\epsilon_{11} + \epsilon_{22}} \tag{3.12}$$

Since $\sigma_{11} = \sigma_{22} = \sigma$ it follows that $\epsilon_{11} = \epsilon_{22} = \epsilon$ and Eq. (3.9) reduces to:

$$\sigma = (C_{11} + C_{12})\epsilon$$

Inserting this in Eq.(3.12) yields the following expression for the bulk modulus:

$$B = \frac{1}{2}(C_{11} + C_{12})$$

As we will require all designs to have symmetric behavior that demands $C_{11}^H = C_{22}^H$, the objective for optimizing the bulk modulus is taken as a average over the bulk moduli in the x_1- and x_2-directions:

$$B^H = \frac{1}{2}\left(\frac{1}{2}\left(C_{11}^H + C_{22}^H\right) + C_{12}^H\right) \tag{3.13}$$

Young's Modulus

The Young's modulus in the x_1-direction is defined by Hook's law as:

$$E_{11} = \frac{\sigma_{11}}{\epsilon_{11}} \tag{3.14}$$

Therefore, Young's modulus can be found from the constitutive relation by considering a uniaxial stress state where $\sigma_{22} = \tau_{12} = 0$. Upon insertion, Eq.s (3.9-3.10) reduce to

$$\begin{aligned} \sigma_{11} &= C_{11}\epsilon_{11} + C_{12}\epsilon_{22} \\ 0 &= C_{12}\epsilon_{11} + C_{22}\epsilon_{22} \end{aligned}$$

Isolation of the latter yields that

$$\epsilon_{22} = -\frac{C_{12}}{C_{22}}\epsilon_{11} \tag{3.15}$$

and hence

$$\sigma_{11} = C_{11}\epsilon_{11} - \frac{(C_{12})^2}{C_{22}}\epsilon_{11}$$

Inserting σ_{11} in Eq. (3.14) results in the following expression for the Young's modulus in the x_1-direction:

$$E_{11} = C_{11} - \frac{(C_{12})^2}{C_{22}}$$

When at least square symmetry is required, the objective for optimizing the Young's modulus is therefore taken as:

$$E^H = \frac{1}{2}(C^H_{11} + C^H_{22}) - \frac{2(C^H_{12})^2}{C^H_{11} + C^H_{22}} \tag{3.16}$$

Shear Modulus

The shear modulus is defined from a state of pure shear where $\sigma_{11} = \sigma_{22} = 0$:

$$\tau_{12} = G_{12}\epsilon_{12} \tag{3.17}$$

From Eq. (3.11) it can easily be seen that the shear modulus in terms of the homogenized constitutive relation can be taken as:

$$G^H = C^H_{33} \tag{3.18}$$

Poisson's Ratio

The Poisson's ratio is defined as the negative of the ratio of the transverse strain to the axial strain.

$$\nu_{12} = -\frac{\epsilon_{22}}{\epsilon_{11}} \tag{3.19}$$

As for the derivation of the Young's modulus expression, a uniaxial stress state ($\sigma_{22} = \tau_{12} = 0$) is considered. Inserting Eq. (3.15) in Eq. (3.19) gives the Poisson's ratio for a normal stress in the x_1-direction:

$$\nu_{12} = \frac{C_{12}}{C_{11}} \tag{3.20}$$

In this work we have therefore used the following expression for designs with optimized Poisson effects:

$$\nu^H = \frac{2C^H_{12}}{C^H_{11} + C^H_{22}} \tag{3.21}$$

3.2.3 Thermal Conduction and Symmetry

Cellular material design for thermal conduction differ slightly from the design for mechanical properties because the finite element formulation for thermal condition only has one degree of freedom per node. The constitutive matrix for thermal properties in 2D is therefore given as the following 2×2 matrix:

$$\mathbf{C}^H_{\text{2D},thermal} = \begin{bmatrix} C^H_{11} & C^H_{12} \\ C^H_{12} & C^H_{22} \end{bmatrix} \tag{3.22}$$

As a result, it is only necessary to apply two test strain fields $\epsilon^{0(i)}$ when using numerical homogenization to upscale from the unit cell properties to the effective material properties.

$$\epsilon^{0(11)} = \begin{bmatrix} 1 \\ 0 \end{bmatrix}, \quad \epsilon^{0(22)} = \begin{bmatrix} 0 \\ 1 \end{bmatrix} \tag{3.23}$$

For thermal conduction problems, it is not relevant to distinguish between square and isotropic symmetry, as both require that $C_{12} = 0$ and $C_{11} = C_{22}$. Therefore Eq.s (3.6) and (3.7) reduce to the same error formulation.

$$error_{sym} = (C^H_{11} - C^H_{22})^2 + (C^H_{12})^2 \tag{3.24}$$

As for mechanical problems, the error is normalized according to Eq. (3.8).

From the homogenized constitutive matrix, the thermal conduction of the effective

material can be expressed as:

$$\kappa^H = C_{11}$$

Since all designs in this work have a required symmetric behavior, we have taken the objective formulation as the average of the thermal conduction in the x_1- and x_2-directions.

$$\kappa^H = \frac{C_{11} + C_{22}}{2} \tag{3.25}$$

3.2.4 Penalization of Intermediate Densities

When solving the topology optimization problem in Eq. (3.1), the Solid Isotropic Material with Penalization (SIMP) method[19] method is used to guide the design to a 0-1 solution. The element stiffness matrices are therefore related to the topology by:

$$\mathbf{K}^e(\phi) = \left(\rho_e^\eta + \rho_{min}^e\right)\mathbf{K}_0^e \tag{3.26}$$

where $\eta \geq 1$ is the exponent penalty term, $\mathbf{K}_0^e$ is the stiffness matrix of a pure solid element and ρ_{min}^e is a small positive number required to maintain positive definiteness of the global stiffness matrix. In this work it is taken as $\rho_{min}^e = 10^{-4}$.

For elastic cellular material design problems that uses numerical homogenization, it is convenient to reformulate the expression for the element contributions to the strain energy and the components of the constitutive matrix for the effective material in terms of ρ^e and $\mathbf{K}_0^e$. The element contribution to the strain energy from Eq (3.4)

is therefore now defined as the contribution from a pure solid element with stiffness $\mathbf{K}_0^e$.

$$q_{ij}^e = \frac{1}{|\Omega|}\left(\mathbf{d_0}^{e(i)} - \mathbf{d}^{e(i)}\right)^{\mathbf{T}} \mathbf{K}_0^e \left(\mathbf{d_0}^{e(j)} - \mathbf{d}^{e(j)}\right) \tag{3.27}$$

The SIMP penalty can now easily be applied to the components of the constitutive matrix from Eq. (3.5).

$$C_{ij}^H = \sum_{e\in\Omega} (\rho_e^\eta + \rho_{min}^e) q_{ij}^e \tag{3.28}$$

3.2.5 Sensitivities

To compute the sensitivity of all objective and error expressions, it is necessary to know the sensitivity of the components of the homogenized constitutive matrix. Using an adjoint method the sensitivity of C_{ij}^H can be found as

$$\frac{\partial C_{ij}^H}{\partial \rho_e} = \eta \rho_e^{\eta-1} q_{ij}^e \tag{3.29}$$

The derivation is described in Bendsøe and Sigmund[1] and is therefore omitted here.

Mechanical Properties

The sensitivity of the bulk modulus from Eq. (3.13) is found by taking the derivative with respect to the element density ρ_e:

$$\frac{\partial B^H}{\partial \rho_e} = \frac{1}{2}\left(\frac{1}{2}\left(\frac{\partial C_{11}^H}{\partial \rho_e} + \frac{\partial C_{22}^H}{\partial \rho_e}\right) + \frac{\partial C_{12}^H}{\partial \rho_e}\right)$$

Inserting $\dfrac{\partial C_{ij}^H}{\partial \rho_e}$ from Eq. (3.29) results in the following expression:

$$\frac{\partial B^H}{\partial \rho_e} = \frac{\eta \rho_e^{\eta-1}}{2}\left(\frac{1}{2}(q_{11}^e + q_{22}^e) + q_{12}^e\right) \tag{3.30}$$

By a similar derivation, the sensitivity of the Young's modulus from Eq. (3.16) is found to be the following.

$$\frac{\partial E^H}{\partial \rho_e} = \eta \rho_e^{\eta-1}\left(\frac{q_{11}^e + q_{22}^e}{2} - \frac{4C_{12}^H q_{12}^e}{C_{11}^H + C_{22}^H} + \frac{2(C_{12}^H)^2}{(C_{11}^H + C_{22}^H)^2}(q_{11}^e + q_{22}^e)\right) \tag{3.31}$$

The expression for the sensitivity of the shear modulus in Eq. (3.18) is:

$$\frac{\partial G^H}{\partial \rho_e} = \eta \rho_e^{\eta-1} q_{33}^e \tag{3.32}$$

Finally, the sensitivity of the Poisson's ratio from Eq. (3.21) is as follows.

$$\frac{\partial \nu^H}{\partial \rho_e} = 2\eta \rho_e^{\eta-1}\left(\frac{q_{12}^e}{C_{11}^H + C_{22}^H} - \frac{C_{12}^H}{(C_{11}^H + C_{22}^H)^2}(q_{11}^e + q_{22}^e)\right) \tag{3.33}$$

Mechanical Symmetries

The sensitivity of the normalized error from Eq. (3.8) is:

$$\frac{\partial error}{\partial \rho_e} = \frac{\partial}{\partial \rho_e}\left(\frac{error_{sym}}{f^2}\right) = \frac{1}{f^2}\frac{\partial error_{sym}}{\partial \rho_e} - 2\frac{error_{sym}}{f^3}\frac{\partial f}{\partial \rho_e} \tag{3.34}$$

Recall that for mechanical properties $error_{sym} = error_{sq}$ and $error_{sym} = error_{iso}$ for requirements of square and isotropic symmetry, respectively. The sensitivity of these are found by takening the derivative of Eq.s (3.6) and (3.7):

$$\frac{\partial error_{sq}}{\partial \rho_e} = 2\eta\rho_e^{\eta-1}\left((C_{11}^H - C_{22}^H)(q_{11}^e - q_{22}^e) + C_{13}^H q_{13}^e + C_{23}^H q_{23}^e\right) \tag{3.35}$$

$$\begin{aligned}\frac{\partial error_{iso}}{\partial \rho_e} &= \frac{\partial error_{sq}}{\partial \rho_e} + 2\eta\rho_e^{\eta-1}\Big(\big(C_{11}^H - (C_{12}^H + 2C_{33}^H)\big) \\ &\quad \cdot\big(q_{11}^e - (q_{12}^e + 2q_{33}^e)\big) \\ &+ \big(C_{22}^H - (C_{12}^H + 2C_{33}^H)\big)\big(q_{22}^e - (q_{12}^e + 2_{33})\big)\Big)\end{aligned} \tag{3.36}$$

Thermal Properties

The sensitivity of the error term used when optimizing the thermal conductivity is found by differentiating Eq. (3.24).

$$\frac{\partial error}{\partial \rho_e} = 2\eta\rho_e^{\eta-1}(C_{11}^H - C_{22}^H)(q_{11}^e - q_{22}^e) \tag{3.37}$$

As the error is also normalized for thermal designs, Eq. (3.34) must again be used.

The sensitivity of the thermal conduction is arrived at by differentiation of Eq. (3.25).

$$\frac{\partial \kappa^H}{\partial \rho_e} = \eta \rho_e^{\eta-1} \frac{q_{11}^e + q_{22}^e}{2} \tag{3.38}$$

3.2.6 Algorithmic Details

The minimum length scale of the solid design features is controlled in this work using the Heaviside Projection Method (HPM)[22] as defined in Eq.s (2.1-2.3). The reader is reader to section 2.2 where HPM is described in full. For all designs in this work continuation is applied to the Heaviside parameter till $\beta_{max} = 50$ in increments $\Delta\beta = 1.1^k$ where k is the iteration number.

The cellular material design problem requires a distributed initial guess for the design variables ϕ_i and an initial SIMP exponent to circumvent the optimizer placing intermediate density material throughout the design domain. In Fig. 3.3 examples of scaled distributed initial guesses are given. In this work the distribution in (a) is used when maximizing the bulk– and Young's modulus and for the multiobjective designs, and (b) is used for maximizing the shear modulus and minimizing the Poisson's ratio. As typically done, we have used SIMP exponents of $\eta_{init} = 3.0$ or $\eta_{init} = 5.0$ and a continuation method is applied to reach η_{max}.

For all designs in this chapter the design domain is defined as a 1×1 unit cell. All problems are solved using four node quadrilateral elements on a 200×200 mesh

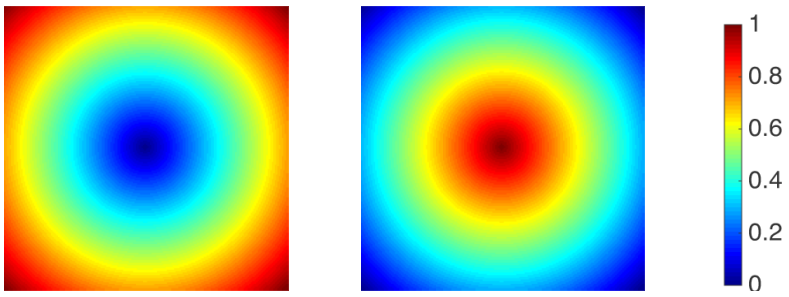

(a) (b)

Figure 3.3: Scaled graded initial guesses for the design variables ϕ_i with (a) solid, and (b) void in the center.

and with the design variable bounds of $\phi_{min} = 0$ and $\phi_{max} = 1$. A plane strain formulation is as the designs are assumed to be extruded out of plane. Young's modulus and Poisson's ratio are taken as $E_0 = 1.0$ and $\nu_0 = 1/3$, respectively. For the heat conduction problem the conductivity of the solid is set to $\kappa_0 = 1.0$.

All problems are solved using the Method of Moving Asymptotes (MMA) as the optimization algorithm.[63,64]

3.3 Cellular Material Topologies with Two Material Phases

In this section the topology optimization problem in Eq. (3.1) has been used to design two-phase cellular material topologies for a range of mechanical properties. In addition, multiobjective topology optimization has been used to design materials for combinations of thermal conduction and mechanical stiffness.

3.3.1 Optimizing for Mechanical Properties

Figure 3.4 shows the unit cells and periodic samples for designs obtained by solving the topology optimization problem in Eq. (3.1) with maximized bulk–, Young's– and shear modulus as the objectives. The designs are obtained with $V_{max} = 50\%$, a square symmetry condition and the minimum length scale of $r_{min} = 0.02$. The optimization is started with an initial SIMP exponent of $\eta_{init} = 5.0$ and raised till $\eta_{max} = 10.0$ through continuation increments of $\Delta\eta = 1.0$.

In Fig. 3.5 three unit cells and 3×3 samples are given for topologies designed

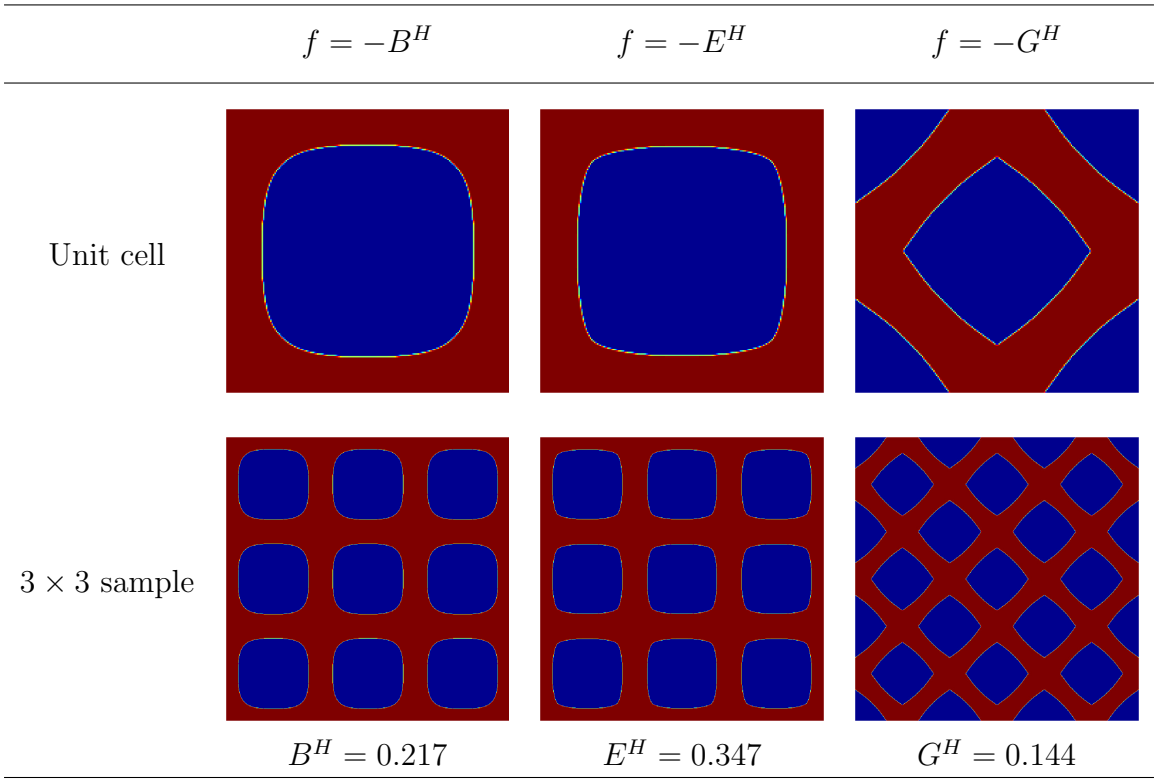

Figure 3.4: Unit cell topologies and 3×3 samples maximized for the stiffness objectives bulk–, Young's– and shear modulus as defined in Eq.s (3.13), (3.16) and (3.18) with $V_{max} = 50\%$ and square symmetry constraints.

for maximized bulks modulus with isotropic symmetry constraints. The topologies have minimum length scales on the topological features of $r_{min} = 0.050$, $r_{min} = 0.020$ and $r_{min} = 0.010$, respectively. The objective values in the figure show that the bulk modulus increases slightly as the minimum feature size is decreased, but that it comes at the cost of an increased complexity of the unit cell design.

Equation (3.1) has also been used to design negative Poisson's ratio materials. Figure 3.6a shows the unit cell topology and periodic sample obtained with $V_{max} = 20\%$ and a square symmetry constraint. The design has been obtained with a constant

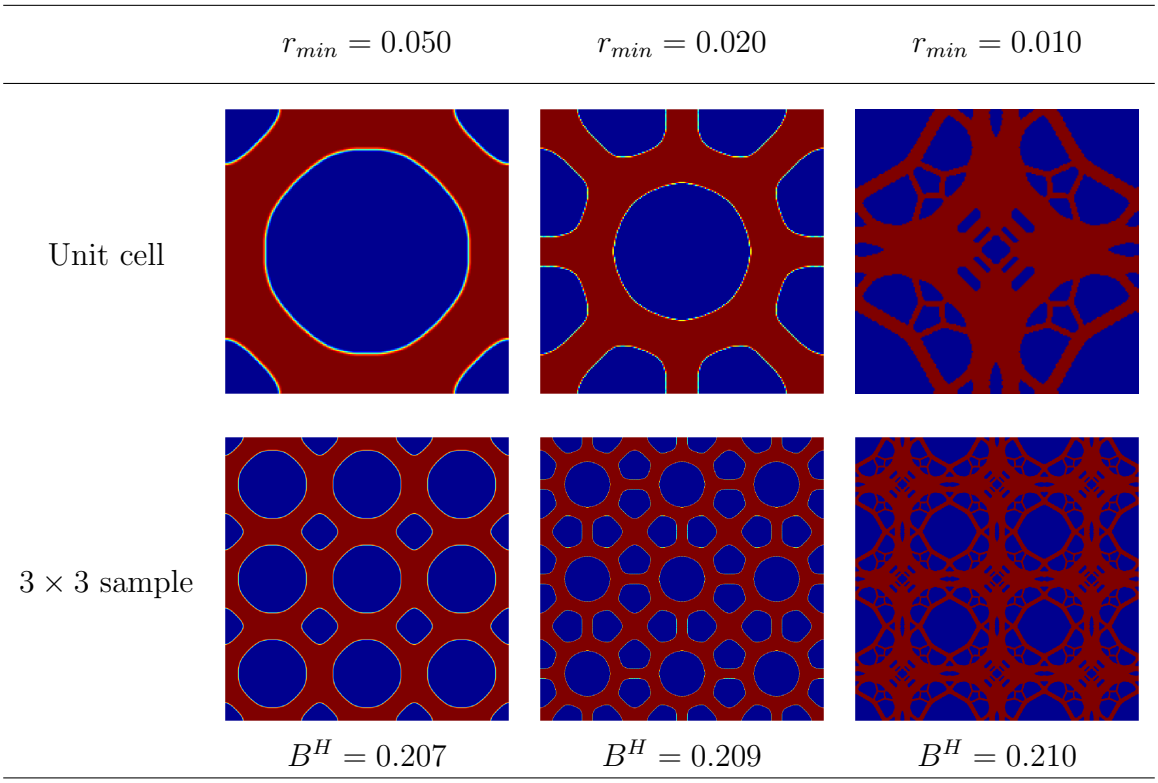

Figure 3.5: Unit cell topologies and 3×3 samples with maximized bulk modulus from Eq. (3.13) with isotropic symmetry constraints and $V_{max} = 50\%$.

SIMP exponent of $\eta = 5.0$. When designing auxerics using the formulation in Eq. (3.1) it is seen that the resulting unit cell topology has artificially stiff one node hinges. To circumvent the existence of these, a robust approach to topology optimization[24,74] has been used. In the robust formulation over and under material deposition is considered by projecting the design variables onto the finite elements multiple times in every iteration. For each projection the equilibrium is solved. Herein over and under material deposition by Δr is herein considered as in[24] and illustrated in Fig.

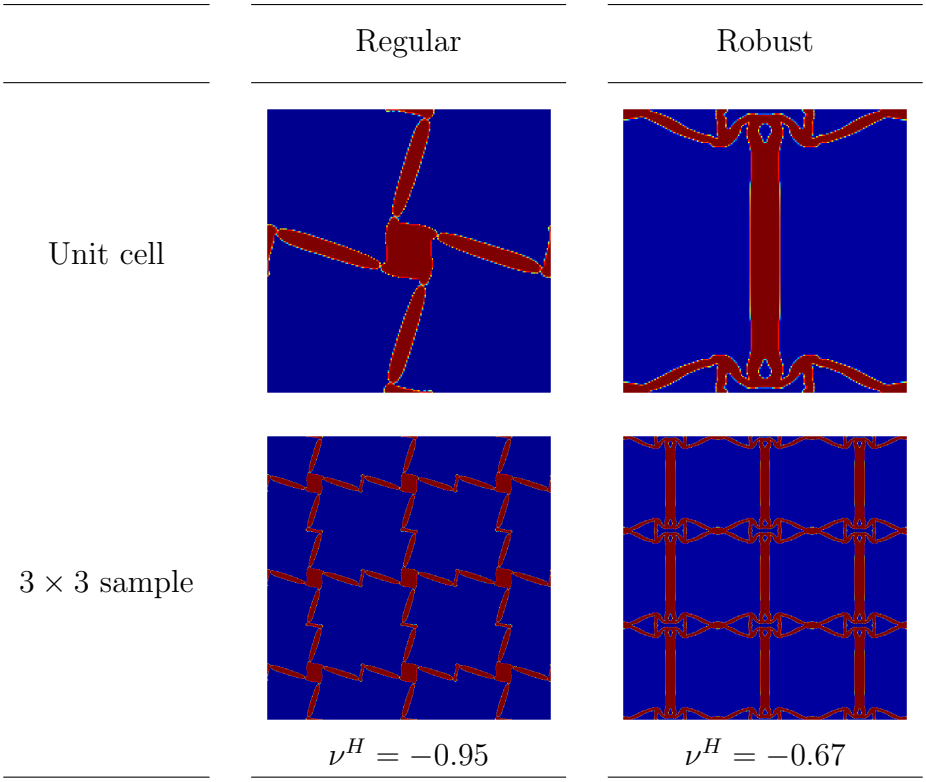

Figure 3.6: Negative Poisson's ratio designs with $V_{max} = 20\%$, a square symmetry constraint and $r_{min} = 0.015$ using (a) the regular problem formulation in Eq. (3.40) and (b) the robust problem formulation in Eq. (3.40) with $\Delta r = 0.005$.

3.7. Each design variable is radially projected twice onto the finite elements with minimum length scales of $r_{min,small}$ and $r_{min,large}$ defined as

$$\begin{aligned} r_{min,small} &= r_{min} - \Delta r \\ r_{min,large} &= r_{min} + \Delta r \end{aligned} \tag{3.39}$$

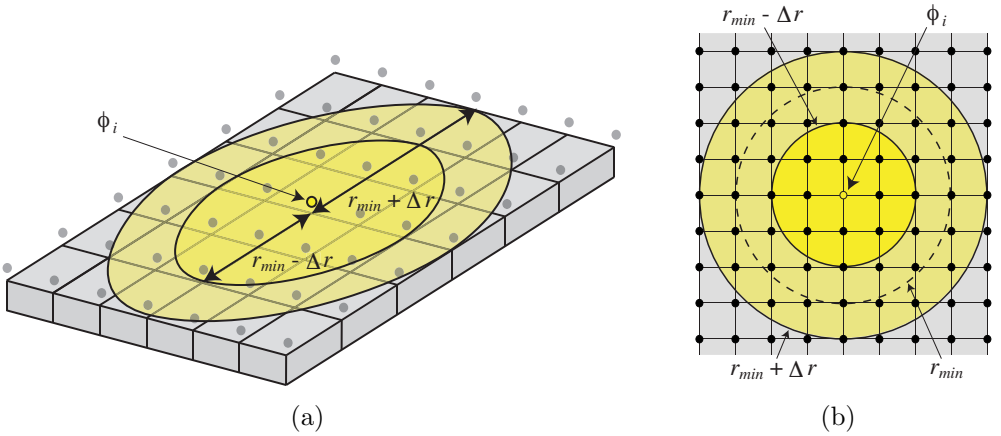

Figure 3.7: Schematic of the robust topology optimization formulation used herein. Figure (a) illustrates the material placement space that projects twice onto the physical space, and (b) shows a top view of a design variable projecting with $r_{min} - \Delta r$ and $r_{min} + \Delta r$ onto the finite elements.

The robust topology optimization problem for cellular material design defined as:

$$
\begin{aligned}
\underset{\phi}{\text{minimize}} \quad & \max\{f(\mathbf{C}^H_{(r_{min,small})}),\ f(\mathbf{C}^H_{(r_{min,large})})\} \\
\text{subject to} \quad & \mathbf{K}\big(\rho(\phi)_{(r_{min,small})}\big)\mathbf{d}^{(i)}_{(r_{min,small})} = \mathbf{f}\big(\rho(\phi)_{(r_{min,small})}\big)^{(i)} \quad \forall \quad i \\
& \mathbf{K}\big(\rho(\phi)_{(r_{min,large})}\big)\mathbf{d}^{(i)}_{(r_{min,large})} = \mathbf{f}\big(\rho(\phi)_{(r_{min,large})}\big)^{(i)} \quad \forall \quad i \\
& g\big(\mathbf{C}^H_{(r_{min,small})}\big) \geq g_{min} \\
& g\big(\mathbf{C}^H_{(r_{min,large})}\big) \geq g_{min} \\
& \sum_{e\in\Omega} \rho_{e(r_{min})} v_e \leq V_{max} \\
& \phi_{min} \leq \phi_n \leq \phi_{max} \quad \forall \quad n \in \Omega \\
& \mathbf{d}^{(i)} \quad \text{is } \Omega\text{-periodic}
\end{aligned}
\tag{3.40}
$$

Figure 3.6b gives the topology obtained by solving Eq. (3.40) with $r_{min} = 0.015$ and $\Delta r = 0.005$. Compared to design solution achieved by the regular topology optimization formulation in Fig 3.6a, it is seen that the robust formulation does not allow the artificially stiff one node hinges to appear in the design.

3.3.2 Multiobjectives in the Mechanical and Thermal Behaviors

The multiobjective topology optimization performed in this work uses a scaled sum of the desired properties as its objective and hence follows the formulation from.[12–15]

This objective formulation can be used for stiffness–thermal conduction properties due to the Gibiansky-Torquato bound.[89]

$$\begin{aligned} \underset{\phi}{\text{minimize}} \quad & \sum_{j}^{nobj} \omega_j \cdot f_j(\mathbf{C}^H(\phi, \mathbf{d}^{(i)})) \\ \text{subject to} \quad & \mathbf{K}(\phi)\mathbf{d}^{(i)} = \mathbf{f}^{(i)} \quad \forall \quad i \\ & g\big(\mathbf{C}^H(\phi, \mathbf{d}^{(i)})\big) \geq g_{min} \\ & \left| \sum_{e\in\Omega} \rho_e v_e - V \right| \leq \text{tol} \\ & \phi_{min} \leq \phi_n \leq \phi_{max} \quad \forall \quad n \in \Omega \\ & \mathbf{d}^{(i)} \quad \text{is } \Omega\text{-periodic} \end{aligned} \tag{3.41}$$

where $nobj$ is the number of objectives and ω_j are the objective weighting factors.

The design is performed with two base material phases where one (the blue phase) has full thermal conduction but zero stiffness and the other (the red phase) has full stiffness but no thermal conduction ability. To force the optimizer to use equal amounts of the two phases the absolute value function is applied to the volume constraint in Eq. (3.41). As a result, the sensitivity of the volume constraint is computed as:

$$\frac{\partial \left| \sum_{e\in\Omega} \rho_e v_e - V \right|}{\partial \rho_e} = \frac{\sum_{e\in\Omega} \rho_e v_e - V}{\sqrt{\left(\sum_{e\in\Omega} \rho_e v_e - V \right)^2}} \cdot v_e \tag{3.42}$$

Fig. 3.8 gives the obtained topologies from solving Eq. (3.41) for maximized objectives of bulk modulus B^H and thermal conduction κ^H as defined in Eq.s (3.13)

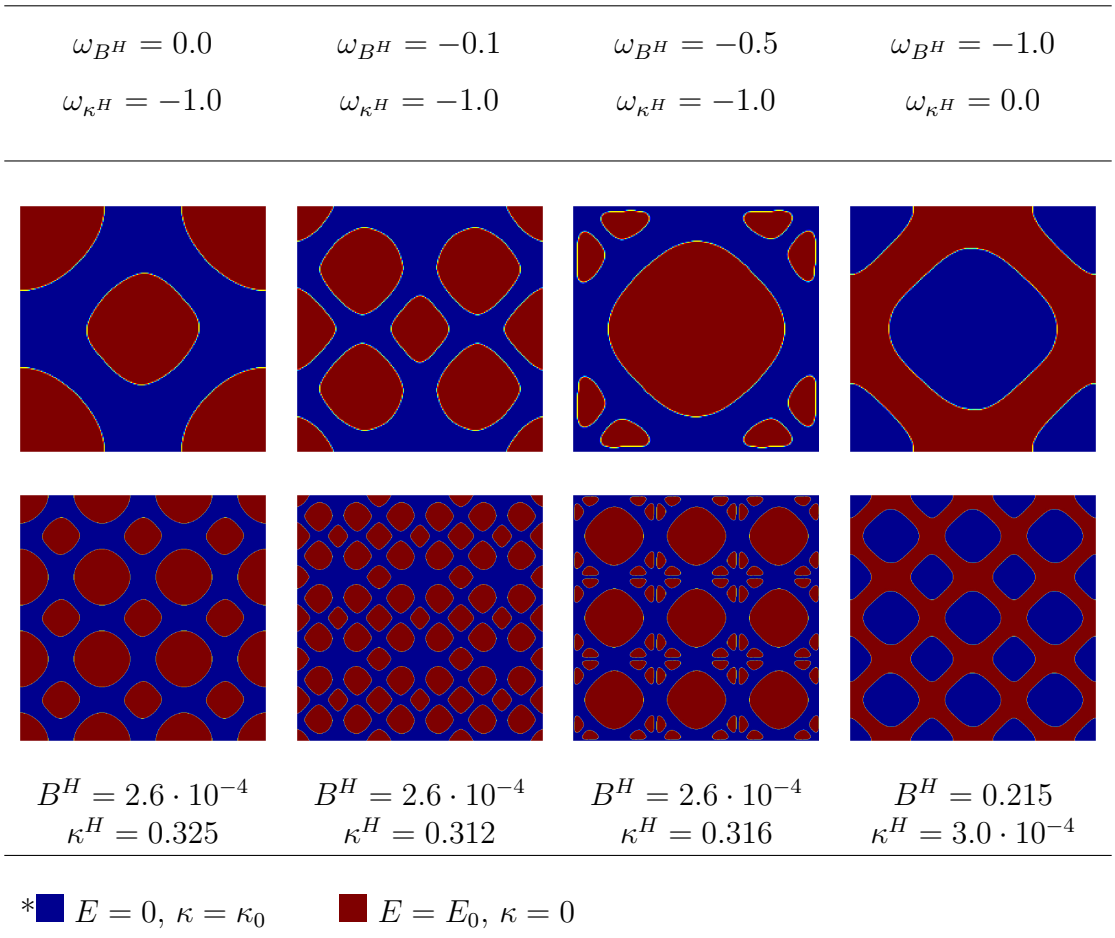

Figure 3.8: Unit cell and 3×3 samples of topologies maximized for multiobjectives of bulk modulus B^H and thermal conduction κ^H as defined in Eq.s (3.13) and (3.25).

and (3.25) with $V = 50\%$. The results are found using continuation on the SIMP exponent from $\eta_{init} = 5.0$ to $\eta_{max} = 10.0$ in increments of $\Delta\eta = 1.0$. Figure 3.8 shows topologies obtained with a range of different weighting factors on the thermal conductivity ω_{κ^H} and the bulk modulus ω_{B^H}. The figure shows how the designs change when the emphasis is shifted from being exclusively on the thermal conduction to increasingly on the bulk modulus (left to right). When the stiffness property is not fully emphasized, topologies are created where the stiff (red) phase is not connected.

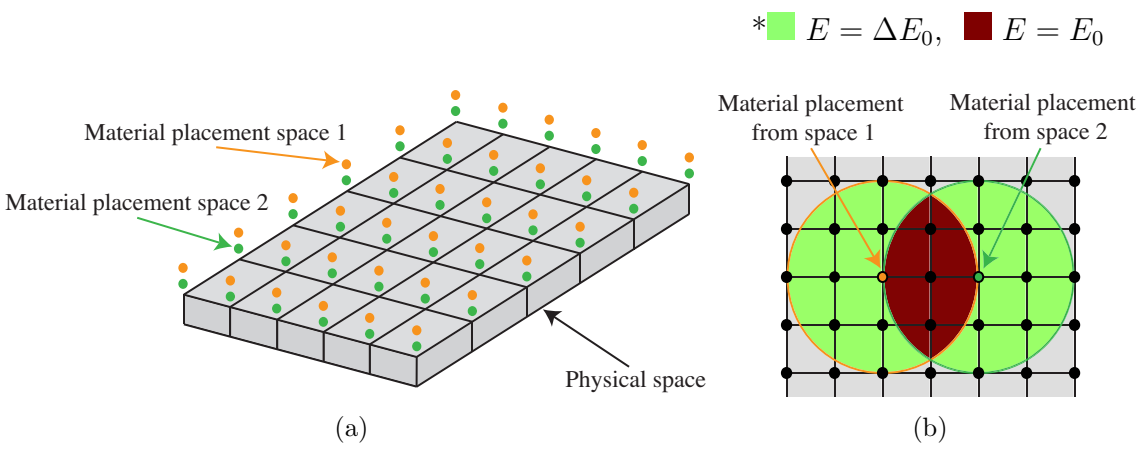

Figure 3.9: Schematic of the used multimaterial topology optimization approach for design with two solid materials that varyies with ΔE in stiffness. Figure (a) illustrates the two material placement spaces and the physical represenation, and (b) shows how the placement spaces each projects features with ΔE stiffness onto the finite elements.

3.4 Cellular Material Design with Multiple Material Phases

As mentioned in the introduction of this chapter, there exists several formulations that include multiple material phases in topology optimization.[24,40] In this work we have used the combinatorial formulation proposed by Gaynor et al.[24] because it adds the least nonlinearity to the design problem. The cellular designs in this work will consist of three material phases, however the algorithm is generally extendable.

The multimaterial design approach suggested by Gaynor et al.[24] is projection based. It is therefore convenient to recall from section 2.2 how the Heaviside Projection Method (HPM) divides the topology optimization problem into two spaces; a material placement space where the optimization is performed and a physical repre-

sentation where the finite element equilibrium is solved. In the extension to multimaterial design, each solid material phase is associated with a separate design variable space. The spaces individually projects on to the finite elements using standard HPM as defined in Eq.s (2.1-2.3). Therefore, for the example of three phase design, the topology optimization problem will have a material placement space 1 and 2 as schematically illustrated by the orange and green spheres in Fig. 3.9a. Figure 3.9b shows design variables from each of these spaces projecting features of ΔE stiffness onto the finite elements. The total element stiffness is simply the addition of the penalized projections from all spaces. For three phase design that leads to the following expression:

$$E_e = \left[\left(\rho_e(\phi_1)\right)^{\eta_1} + \left(\rho_e(\phi_2)\right)^{\eta_2}\right]\Delta E \tag{3.43}$$

where η_1 and η_2 are the SIMP exponents. In this work a small offset is used between η_1 and η_2 to ensure that the optimizer does not get stuck at the first iteration. For all designs we have used that $\eta_2 = \eta_1 - \eta_{off}$ and $\eta_{off} = -0.1$.

It should be noted that in the multimaterial formulation, using HPM as defined in Eq. (2.3) provides the designer with minimum length scale control of feature sizes, but not with rigorous control on the length scale of the individual material phases within the feature.

Topology optimization of elastic cellular materials with three phases can be solved

using the following formulation.

$$
\begin{aligned}
\underset{\phi}{\text{minimize}} \quad & f(\mathbf{C}^H(\phi, \mathbf{d}^{(i)})) \\
\text{subject to} \quad & \mathbf{K}(\phi)\mathbf{d}^{(i)} = \mathbf{f}(\phi)^{(i)} \quad \forall \quad i \\
& g\big(\mathbf{C}^H(\phi, \mathbf{d}^{(i)})\big) \geq g_{min} \\
& \sum_{e \in \Omega} H(\rho_{e,avg}(\phi)) v_e \leq V_{max} \\
& \sum_{e \in \Omega} \rho_e(\phi_1) v_e \leq V_1 \\
& \sum_{e \in \Omega} \rho_e(\phi_2) v_e \leq V_2 \\
& \phi_{min} \leq \phi_n \leq \phi_{max} \quad \forall \quad n \in \Omega \\
& \mathbf{d}^{(i)} \quad \text{is } \Omega\text{-periodic}
\end{aligned}
\tag{3.44}
$$

Notice that Eq. (3.44) has three volume constraints: one for each of the material phases $\rho_e(\phi_1)$ and $\rho_e(\phi_2)$, and one for the total amount of volume in the design domain. The total amount of volume is in this work evaluated by using a Heaviside function on the average of the $\rho_{e,avg}$ of the element densities, such that all solid elements in the design domain have same emphasis regardless of its stiffness. In this work we have used the Heaviside formulation in Eq. (2.3).

3.4.1 Topologies with Improved Mechanical Properties

The multimaterial topology optimization problem for cellular material design in Eq. (3.44) has been solved with two solid base materials for a range of mechanical properties. The solutions can therefore consist of three material phases: a void (blue) phase with ~ 0 stiffness, a complaint (green) phase with ΔE stiffness and a stiff (red)

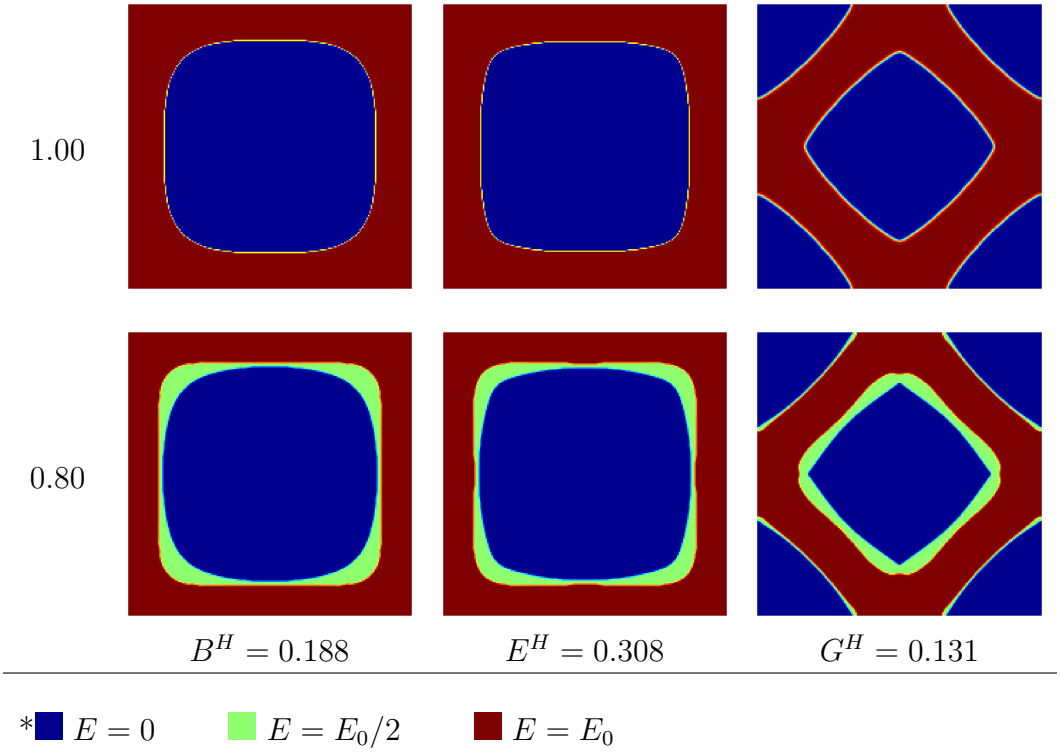

Figure 3.10: Multimaterial unit cell topologies maximized for the stiffness objectives bulk–, Young's– and shear modulus as defined in Eq.s (3.13), (3.16) and (3.18) with $V_{max} = 50\%$, $V_2 = 1.00V_1$ and $V_2 = 0.80V_1$.

phase with E_0 stiffness. In this work we have used $\Delta E = E_0/2$ and as previously specified we have taken the Young's modulus and Poisson's ratio as $E_0 = 1$ and $\nu_0 = 1/3$.

Figure 3.10 gives the obtained unit cell topologies for maximizing the stiffness objectives of bulk–, Young's– and shear modulus with a square symmetry constraint. The results are obtained with SIMP continuation from $\eta_{init} = 5.0$ till $\eta_{max} = 10.0$ in increments of $\Delta\eta = 1.0$. The minimum length scale is specified as $r_{min} = 0.02$ and a continuation scheme is used on the Heaviside parameter till $\beta_{max} = 50$. It is found that the total volume constraint works best if the Heaviside parameter β_{vol} has a small initial value and is then gradually increased. In this work we have used $\beta_{vol,init} = 3.0$ and increased to $\beta_{vol,max} = 15.0$ in increments of $\Delta\beta_{vol} = 3.0$. Two types of volume constraints has been applied to obtain the topologies in Fig. 3.10. In the top row of the figure, the optimizer has been allowed to use as much as desired of each solid phase, i.e. $V_{max} = V_1 = V_2 = 50\%$. As expected, the obtained topologies only consist of the void (blue) and the stiff (red) material phases. Visual comparison of the two-phase topologies in Fig. 3.4 with the three-phase designs in top row of Fig. 3.10 reveals that the solutions are nearly identical. The figure's second row contain solutions obtained with a requirement of having 20% of the designed topology being of the complaint (green) phase, i.e. $V_{max} = 50\%$, $V_1 = 50\%$ and $V_2 = 40\%$. For stiffness objectives this requirement obviously results in a decreased performance. However, it is interesting to note that the optimizer choses to place the complaint (green) phase

Table 3.1: Normalized performance of the unit cell topologies with three material phases (Fig. 3.10). The normalization is performed by dividing with the objective values obtained with two material phases (Fig. 3.4).

V_2/V_1	$f = -B^H$	$f = -E^H$	$f = -G^H$
1.00	98.4%	98.7%	92.2%
0.80	86.5%	88.6%	90.5%

where it would first remove material if designing with a lower volume fraction.

In Tab. 3.1 the performance of the two types of three-phase designs is compared. A normalization has been done where the objective values from Fig. 3.10 are divided by the performances of the two-phase topologies in Fig. 3.4. The first row of the table shows that the performance is very similar when there is no required use of the complaint (green) phase - especially for the bulk– and Young's modulus designs. The second row reveals that the 20% required complaint (green) phase results in $10-15\%$ lower performance. For the shear modulus topologies, it is seen that designing with two solid material phases without a specific phase requirement causes a minor sacrifice of the performance. The very small difference between the performance values in the last column is largely attributed to this.

The multimaterial topology optimization problem has also been solved for minimized Poisson's ratio with square symmetry conditions as defined in Eq. (3.21). However the formulation in Eq. (3.44) has been modified slightly to a robust formulation similar to that in Eq. (3.40). A minimum length scale of $r_{min} = 0.015$ has

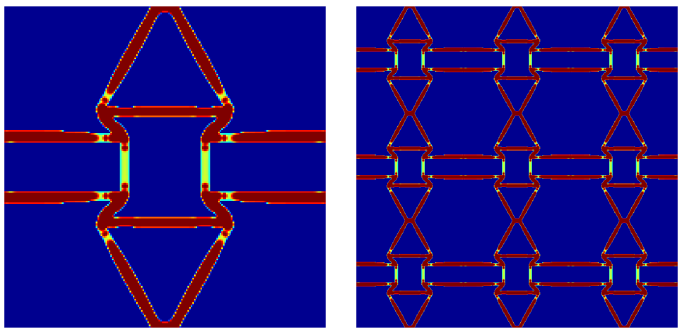

(a) (b)

Figure 3.11: Multimaterial negative Poisson's ratio design with $V_{max} = 20\%$ and $V_2 = 1.00V_1$; (a) gives unit cell topology, and (b) provides a 3×3 sample of the effective material. A square symmetry constraint is applied and a robust formulation is used with $r_{min} = 0.015$ and $\Delta r = 0.005$.

been prescribed and the length scale variation taken as $\Delta r = 0.005$. We have used a constant SIMP penalty term of $\eta = 3.0$ and continuation on the Heaviside parameter till $\beta_{max} = 50$. For this problem the total volume constraint has been enforced with an initial Heaviside parameter of $\beta_{vol,init} = 1.0$ that has been gradually increased to $\beta_{vol,max} = 15.0$ through increments of $\Delta\beta_{vol} = 1.0$. Finally, the design is conducted with $V_{max} = 20\%$ and the optimizer has been free to chose how much of each material phase to use.

Figure 3.11 gives the obtained unit cell topology and a 3×3 sample of the cellular material. It is noteworthy that the complaint (green) material is placed in the hinge regions of the topology where the performance benefits from flexibility. Table 3.2 compares the amounts of used material and the obtained Poisson's ratios for the robust two-phase design in Fig. 3.6b and the three-phase design in Fig. 3.11. It should

here be noted that the auxerics material design problem is self penalizing and the optimizer therefore not necessarily chooses to use all available material. The table shows that the three-phase design uses a smaller total material volume but achieves a more negative Poisson's ratio. It is seen that the optimizer has chosen that 14.5% of the placed volume is of the complaint (green) phase and that the increase in performance is over the two-phase design 7.25%.

Table 3.2: Comparison of the performance and material use in the robust negative Poisson's ratio designs with two material phases (Fig. 3.6b) and three material phases (Fig. 3.11).

	V_{total} $(red + green)$	V_{stiff} (red)	$V_{compliant}$ $(green)$	ν^H
2 material phases	18.44%	18.44%	N/A	-0.67
3 material phases	15.54%	13.28%	2.26%	-0.74

3.4.2 Designs Optimized for Stiffness–Conduction Objectives

The proposed three-phase topology optimization algorithm has also used to design cellular topologies for objective combinations of thermal conduction and bulk modulus. In this context the three material phases represents a conductive (blue) phase with full conduction capability and ~ 0 stiffness ($\kappa = \kappa_0, E = 0$), a semi stiff–semi

conductive (green) phase with $\kappa = \Delta\kappa_0, E = \Delta E_0$, and a stiff (red) phase with no conduction capability ($\kappa = 0, E = E_0$). To solve this design problem, the multimaterial topology optimization formulation in Eq. (3.44) has been changed to allow for multiobjectives similarly to the formulation in Eq. (3.41).

Figure 3.12 gives the unit cell topologies and 3×3 sample of the cellular materials obtained with different combinations of the objective weighting factors ω_{κ^H} and ω_{B^H}. We have required the use of $V = 50\%$ purely conductive (blue) material, square symmetry conditions and specified the minimum length scale as $r_{min} = 0.02$. The solutions are obtained with a constant SIMP exponent of $\eta = 5.0$ and for this problem the continuation on the Heaviside parameter on the volume constraint has been applied from $\beta_{vol,init} = 5.0$ to $\beta_{vol,max} = 15.0$ in increments of $\Delta\beta_{vol} = 5.0$. The figure shows (from left to right) how the unit cell topologies change from having full emphasis on the conductive properties of the effective material, to placing increased focus on the stiffness objective. Initially the optimizer is found to place the semi stiff–semi conductive (green) phase in well-known effective stiffness layouts. This causes a negligible reduction in the conductive performance of the effective material. Finally the optimizer uses the stiff (red) material in the same stiffness layout, resulting in almost zero conduction capability.

$\omega_{B^H} = 0.0$	$\omega_{B^H} = -0.1$	$\omega_{B^H} = -0.5$	$\omega_{B^H} = -1.0$
$\omega_{\kappa^H} = -1.0$	$\omega_{\kappa^H} = -1.0$	$\omega_{\kappa^H} = -1.0$	$\omega_{\kappa^H} = 0.0$
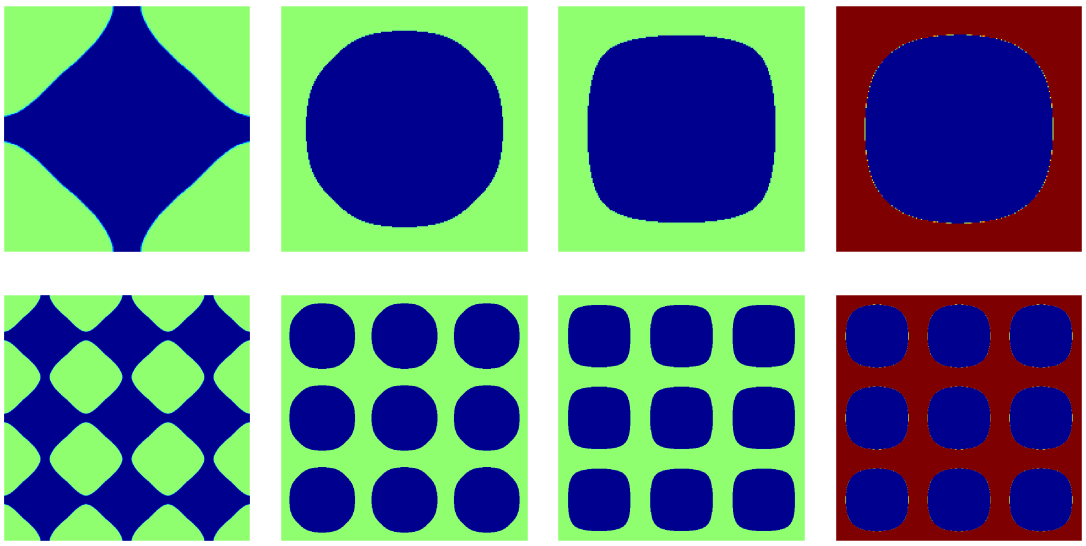			
$B^H = 2.9 \cdot 10^{-4}$ $\kappa^H = 0.708$	$B^H = 0.100$ $\kappa^H = 0.676$	$B^H = 0.105$ $\kappa^H = 0.680$	$B^H = 0.220$ $\kappa^H = 3.0 \cdot 10^{-4}$

*$E = 0$, $\kappa = \kappa_0$ $E = E_0/2$, $\kappa = \kappa_0/2$ $E = E_0$, $\kappa = 0$

Figure 3.12: Multimaterial unit cell topologies maximized for multiobjective combinations of bulk modulus B^H and thermal conduction κ^H as defined in Eq.s (3.13) and (3.25) with $V_{max} = 50\%$ and $V_2 = 1.00V_1$.

3.5 Summary

A technique is proposed for multimaterial topology optimization of periodic cellular materials that allows cellular designs with two or more solid base materials. The multimaterial projection-based approach from Gaynor et. al[24] is used and therefore the designer is provided with minimum length scale control over the feature sizes. However, the current formulation does not allow specific length scale control over the

individual phases within a feature.

The main disadvantage of the proposed approach is that a large number of design variables is needed. For example, doubling the number of design variables is required for three-phase design since a design variable space is needed per solid phase. Although the methodology is generally extendable to designing with a higher number of phases, solving even simple problems with a very large number of candidate materials becomes involved. In addition, nonlinearity is added to the optimization problem through the total volume constraint. For stiffness objectives this has not been observed to pose any difficulty, however for problems with a more nonlinear nature it might. For the robust negative Poisson's ratio design and for the multiobjective designs that use the absolute value on the volume constraint we have found that some parameter tuning was needed to obtain quality solutions.

Chapter 4

Cellular Materials with Nonlinear Properties

4.1 Introduction

As discussed in previous chapters, implementations of topology optimization have mainly focused on design for linear properties. Solutions to linear elastic problems are optimal only for the problem as mathematically posed and hence only for the linear elastic response. This may lead to designs that exhibit undesirable effects in the nonlinear regime. Examples include designs that are stiff but brittle, or stiff without redundant load paths. Additionally, considering only linear mechanics excludes the possibility of optimizing for nonlinear properties. As an example of an application where designing for nonlinear properties is appealing, can be mentioned cellular

materials of Bulk Metallic Glasses (BMGs). BMGs are a type of metals with an amorphous atomic structure that makes them very stiff and strong but prone to brittle failure for macroscopic freature sizes (> 1 mm). An interesting property of BMGs is that they exhibit microscopic ductility.[90] Recent advances in manufacturing technologies has made it possible to fabricate cellular BMG materials by thermoplastic forming. The effective energy absorption observed for cellular BMGs with traditional honeycomb topologies are drastically enhanced compared to solid BMGs.[91] Topology optimization has the potential to improve the ductility even further. Therefore this chapter investigates the possibility of extending topology optimization to design cellular materials governed by nonlinear mechanics.

Few methodologies for performing topology optimization under nonlinear mechanics have been developed. The first algorithms with nonlinear effects separately considered elasto-plastic materials[25,92] and geometric nonlinearity.[26,27,46,93] These research efforts clearly showed that including nonlinearities has a significant effect on the obtained topology if the response enters the nonlinear regime. Topology optimization schemes have since been suggested for several nonlinear phenomena including visco-elasticity,[94] fatigue,[95] and interface and contact problems.[96–98] In this work our discussion on nonlinearity in topology optimization will concentrate on material– and geometric nonlinearities.

Most research on including nonlinearities in topology optimization has focused on structural and component level design. Maute et al.[25] developed a topology optimiza-

tion approach and sensitivity analysis scheme for maximizing the energy absorption of structures made of an elasto-plastic material. The energy absorption is here defined as the area under the stress-strain curve. The algorithm is demonstrated on 2D plane stress beam examples with displacement control. The formulation uses an isotropic hardening law and is limited to infinitesimal strains. Geometric nonlinearities were first included by Buhl et al.[26] that suggested an algorithm and sensitivity analysis for finite strains. The algorithm was limited to force controlled design problems and demonstrated on beam designs for compliance and absorbed energy objectives. Bruns and Tortorelli[46] and Pedersen et al.[27] extended the formulation to design compliant inverter mechanism under finite strains.

Including nonlinear mechanics in the cellular design problem faces the additional challenge lacking rigorous upscaling technique. Nakshatrala et al.[99] were the first to include nonlinear effects in cellular topology design and suggested using a numerical homogenization procedure to evaluate the effective properties for hyperelastic materials under finite deformation. A hierarchical multi-scale topology optimization approach was proposed and demonstrated through the design of compliance beams with locally varying unit cells. Wang et al.[100] also performed cellular design with a hyperelastic base material under finite strains, but designed for prescribed stress-strain curves and Poisson's ratio using 2D truss and continuum elements. The upscaling is suggested as a subjecting the unit cell to a series of tensile tests and the effective properties obtained by the upscaling method were compared to the response of a

finite sample. However, the topology optimization performed by Wang et al.[100] was simplified by only considering tensile loading cases and hence implicitly limiting the buckling occurrence in the designed topologies.

Energy absorption is important for numerous cellular material applications. When designing for energy absorbing objectives elasto-plastic buckling can be an important contributing factor. However, both material– and geometric nonlinearities must be included in the formulation to capture elasto-plastic buckling. To date only a couple of researches have formulated topology optimization algorithms that combine material– and geometric nonlinearities. Wallin et al.[101] proposed a formulation for topology optimization with finite strain plasticity and demonstrated it on beam examples with maximized plastic energy absorption. The sensitivity scheme is based on the adjoint method for coupled transient problems and results in a path-dependent adjoint strategy. Lotfi[102] simplified the sensitivity calculation by using existing schemes for material–[25] and geometric nonlinearities[26] and combining them through addition. The sensitivity scheme was used to maximize the energy absorption for cellular BMG topologies using finite periodicity for the upscaling.

It should be noted that true energy absorption refers to applications subjected to impact loading. A limited number of topology optimization algorithms with nonlinear mechanics have been presented for impact loading. Nakshatrala and Tortorelli[103] proposed a framework for designing with an elasto-plastic material subjected to dynamic loading and demonstrated it on a plate design problem. It is worth emphasizing that

the proposed algorithm assumes infinitesimal strains. Nakshatrala and Tortorelli[104] recently extended the framework to hierarchical design with a hyperelastic material under finite strains. The suggested approach is based on the assumption that the primary wavelengths of interest are much longer than the size of the unit cells and therefore that the effective properties can be computed using the static homogenization theory proposed in.[99] Algorithms that consider both material– and geometric nonlinearities for impact problems are yet to be developed.

The aim of the current chapter is to investigate the necessary steps in developing topology optimization with both material– and geometric nonlinear mechanics for the design of periodic cellular materials. The chapter will first discuss the challenges encountered when nonlinear mechanics are included in the topology optimization formulation. The effect it has on the obtained topology will be demonstrated on the beam benchmark problems for material– and geometric nonlinearities from Maute et al.[25] and Buhl et al.[26] This will be followed by an examination of the key components in formulating a finite plasticity optimization algorithm for cellular topology design. The last section of the chapter will numerically analyze the cellular BMG topologies that were maximized for energy absorption by Lotfi.[102] Preliminary analysis has shown that the designed topologies achieved a higher level of energy absorption than other topologies.[105–107] The numerical analyses in this work will compare the nonlinear stress-strain responses of the new BMG designs to the behaviors of cellular BMGs with traditional topologies and topologies designed for various elastic properties.

4.2 Topology Optimization of Beams with Nonlinear Mechanics

The topology optimization problem for structural or component design with nonlinear mechanics is typically formulated as follows:

$$\begin{aligned} \underset{\phi}{\text{minimize}} \quad & f(\phi, \mathbf{d}) \\ \text{subject to} \quad & \mathbf{R}(\phi, \mathbf{d}) = \mathbf{0} \\ & \sum_{e \in \Omega} \rho_e v_e \leq V_{max} \\ & \phi_{min} \leq \phi_n \leq \phi_{max} \quad \forall \quad n \in \Omega \end{aligned} \tag{4.1}$$

Here f is the objective function and ϕ is the design variables. The material or volume use is limited by V_{max} and ϕ_{max} and ϕ_{min} describes the design variable bounds that in work are taken as 0 and 1. The element volume is denoted v^e and ρ^e is the density of element e. The element densities are in this work related to the design variables using the standard Heaviside Projection Method (HPM)[22] as it provides implicit minimum length scale control of the topological features. The procedure follows Eq.s (2.1-2.3) and the reader is referred to section 2.2 for a full description. The problems in this chapter are solved using continuation on the Heaviside parameter with $\Delta\beta = 1.1^k$ where k is the iteration number.

The equilibrium condition in Eq. (4.1) is described in terms of $\mathbf{R}(\phi, \mathbf{d})$ which

is the residual force vector. This equilibrium condition must be solved using an iterative nonlinear FE solver. For this purpose we have developed standard Newton-Raphson schemes for (i) geometric nonlinearities, (ii) a plasticity model for infinitesimal strain with isotropic hardening that uses the radial return method, and (iii) combined material– and geometric nonlinearities. The FE solvers uses standard formulations as found in literature.[108–110]

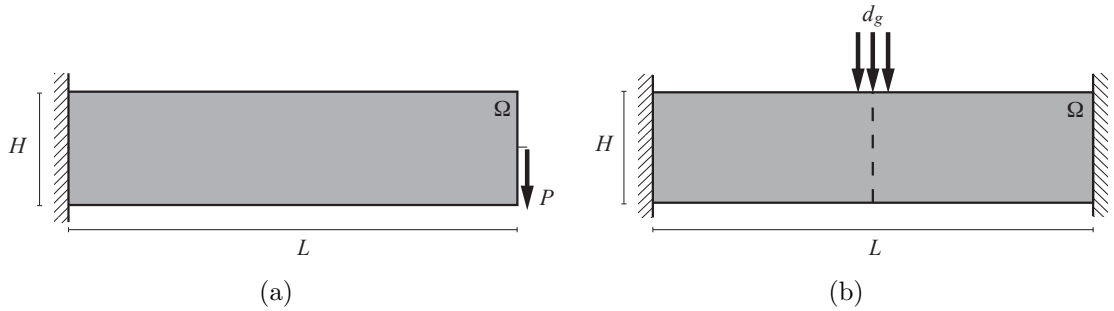

Figure 4.1: Design domains for the benchmark beam design problems that considers (a) geometric– , and (b) material nonlinear effects.

In this section the benchmark beam examples for geometric and material nonlinearities from Buhl et al.[26] and Maute et al.[25] will be redesigned to illustrate the effect of nonlinearities in the topology optimization formulation. The design domains for the two problems are shown in Fig. 4.1. Figure 4.1a shows the cantilever beam problem that geometric nonlinear effects are typically demonstrated on and Fig. 4.1b gives the design domain for the clamped beam problems that is commonly used to illustrate the effect of elasto-plasticity.

All problems in this chapter are solved using the Method of Moving Asymptotes

(MMA) as the optimization algorithm.[63,64]

4.2.1 Solids-Only Modeling in the Physical Space

An important drawback of material distribution approaches is the requirement of modeling the entire domain, including void regions. Elements in the void regions are structurally insignificant in the analysis and they are removed in the manufacturing of the final design. They are, however, still needed in the optimization process for reintroduction of material as the design evolves. It can therefore be said that they are necessary for the design portion of the optimization process, not the analysis. In fact, elements of negligible volume fraction are quite detrimental to analysis as they maximize the size of the system to be solved and thus computational expense and are susceptible to numerical instabilities under nonlinear mechanics, such as excessive distortions under finite deformations.

Researchers have proposed different methods for neglecting void element analysis such as re-meshing,[111] modified nonlinear convergence criteria[26] and stabilizing the stiffness matrix following Gaussian elimination.[93] Recently it has been suggested to use a hyperelastic formulation for tension elements,[112] a linear formulation for elements in compression[113] and a combination of hyperelastic tension elements and linear compression elements.[100] Most of these methods require a threshold ρ_t to be set below which element stiffness is considered negligible. In this work, we simply introduce artificial boundary conditions to degrees of freedom that are surrounded completely by

void elements.[102] Recall from section 2.2 how HPM is based on splitting the topology optimization problem into two spaces: a design variable space where the optimization is done and a physical representation space where the finite element analysis is conducted. This means that we can place boundary conditions on the finite elements without loosing design variable functionality. The temporary boundary conditions are placed by looping over the elements and marking the nodes of elements whose stiffness is to be modeled ($\rho^e > \rho_t$). Nodes that are unmarked receive a temporary boundary condition. Equation numbering and finite element assembly proceed in the standard manner, although it is noted the assembly routine need not check the equation numbers of void elements (including these along the structural interface). This process is performed at each design iteration where the solids-topology changes.

4.2.2 Geometric Nonlinearities

Geometric nonlinearities or finite deformations are characterized by the shape and location differing significantly in the reference or initial configuration $\mathbf{X}$ and the current deformed configuration $\mathbf{x}$. The small deformation assumption is therefore no longer valid and the equilibrium can no longer adequately be described in terms of the infinitesimal strain ϵ. The residual force for geometric nonlinearities is herein described by

$$\mathbf{R}(\phi, \mathbf{d}) = \mathbf{F} - \int_{\Omega} \mathbf{B}^T \mathbf{s} \, d\Omega \tag{4.2}$$

Here $\mathbf{s}$ is the second Piola Kirchoff stress (here in vector form) and $\mathbf{B}$ is the strain displacement matrix. When using a finite strain formulation we use an advanced $\mathbf{B}$ matrix defined in terms of the Green-Lagrangian strain E_{ij}:

$$E_{ij} = \frac{1}{2}\left(\frac{\partial d_i}{\partial X_j} + \frac{\partial d_j}{\partial X_i} + \frac{\partial d_k}{\partial X_i}\frac{\partial d_k}{\partial X_j}\right) \tag{4.3}$$

The Piola-Kirchoff stress is calculated from the Green-Lagrangian strain using Hook's law:

$$\mathbf{s} = \mathbf{D}^e\mathbf{E} \tag{4.4}$$

where $\mathbf{D}^e$ is the elastic constitutive matrix for element e.

Typical benchmark examples for topology optimization under finite strains designs a cantilever beam for a final compliance objective:

$$f = \mathbf{F}^\mathbf{T}\mathbf{d}_{final} \tag{4.5}$$

where $\mathbf{F}$ is the applied force force vector and $\mathbf{d}_{final}$ contains the final displacements.

We note that using final compliance as the objective function can be problematic as tremendous inefficiencies can result at load magnitudes below those considered in the design problem. This was discussed thoroughly by Buhl et al.[26]

4.2.2.1 Penalization of Intermediate Densities

As for elastic problems, the Solid Isotropic Material with Penalization (SIMP) method[19] is used to guide the design to a 0-1 solution. Therefore the following expression relates the element constitutive matrix to the topology:

$$\mathbf{D}^e(\phi) = \left(\rho_e^\eta + \rho_{min}\right)\mathbf{D_0}^e \tag{4.6}$$

Here $\eta \geq 1$ is the exponent penalty term, $\mathbf{D}_0^e$ is the elastic constitutive matrix of a pure solid element and ρ_{min}^e is a small positive number that is usually required to maintain positive definiteness of the global stiffness matrix. However, the solids only finite element modeling makes the ρ_{min} parameter in Eq. (4.6) unnecessary. Herein we have therefore used $\rho_{min} = 0$ for all nonlinear problems.

4.2.2.2 Sensitivities

The sensitivities used to solve the topology optimization problem in Eq. (4.1) with the final compliance objective in Eq (4.5) is calculated using the adjoint method as suggested by Buhl et al.[26]

Since the residual force vector $\mathbf{R}(\phi, \mathbf{d})$ must equal zero for the structure to meet the equilibrium condition, the term $\lambda^\mathbf{T}\mathbf{R}(\phi, \mathbf{d})$ can be added to the objective function without changing it.

$$f = \mathbf{F}^\mathbf{T}\mathbf{d}_{final} + \lambda^\mathbf{T}\mathbf{R}(\phi, \mathbf{d}) \tag{4.7}$$

Assuming design independent loads, the sensitivity of Eq. (4.7) is

$$\frac{\partial f}{\partial \rho_e} = \mathbf{F^T}\frac{\partial \mathbf{d}_{final}}{\partial \rho_e} + \lambda^{\mathbf{T}}\left(\frac{\partial \mathbf{R}}{\partial \mathbf{d}_{final}}\frac{\partial \mathbf{d}_{final}}{\partial \rho_e} + \frac{\partial \mathbf{R}}{\partial \rho_e}\right)$$

Rearranging and using that the tangent stiffness matrix is defined as $\mathbf{K}_T = -\dfrac{\partial \mathbf{R}}{\partial \mathbf{d}}$ leads to

$$\frac{\partial f}{\partial \rho_e} = \lambda^{\mathbf{T}}\left(\frac{\partial \mathbf{R}}{\partial \rho_e}\right) + \left(\mathbf{F^T} - \lambda^{\mathbf{T}}\mathbf{K}_T\right)\frac{\partial \mathbf{d}_{final}}{\partial \rho_e}$$

The Lagrangian multipliers λ can be chosen freely. To eliminate the costly term $\dfrac{\partial \mathbf{d}_{final}}{\partial \rho_e}$, the adjoint problem is defined as following:

$$\mathbf{F} - \mathbf{K}_T\lambda = \mathbf{0} \tag{4.8}$$

The adjoint problem in Eq. (4.8) is solved to determine λ and the sensitivities of the final compliance can then be found by

$$\frac{\partial f}{\partial \rho_e} = \lambda^{\mathbf{T}}\left(\frac{\partial \mathbf{R}}{\partial \rho_e}\right) \tag{4.9}$$

where the sensitivity of the residual force is found by differentiation of Eq. (4.2).

$$\frac{\partial \mathbf{R}}{\partial \rho_e} = -\int_\Omega \mathbf{B}^T \frac{\partial \mathbf{s}}{\partial \rho_e}\, d\Omega \tag{4.10}$$

Here the stress sensitivity in each gauss point is found by differentiation of Eq.s (4.4)

and (4.6).

$$\frac{\partial \mathbf{s}}{\partial \rho_e} = \eta \rho_e^{\eta-1} \mathbf{D_0}^e \mathbf{E} \tag{4.11}$$

4.2.2.3 Cantilever Beam Designs

The benchmark cantilever beam problem from Fig. 4.1a has been optimized within the design domain of $L = 1$ m and $H = 0.25$ m and with $t = 0.1$ m. To resemble nylon, the material properties have been taken as $E_0 = 3$ GPa and $\nu_0 = 0.4$. In this work the problem has been solved on a 160×40 mesh with 2D plane strain elements and a volume constraint of $V_{max} = 50\%$ has been specified. The minimum length scale has been prescribed as $r_{min} = 12.5$ mm and the maximum Heaviside parameter is taken as $\beta_{max} = 25.0$.

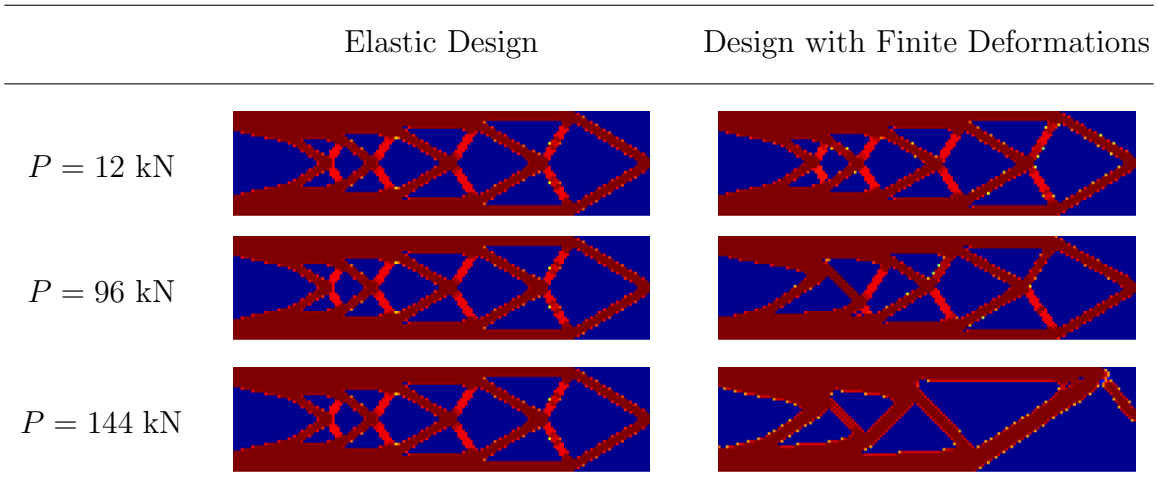

Figure 4.2: Solutions to the benchmark cantilever beam problem with geometric nonlinearities and the final compliance objective from Eq. (4.5). The figure contains the obtained topologies for a various amplitudes of the applied load and provides elastic designs for comparison.

Figure 4.2 shows examples of the obtained topologies. The final compliance problem is solved in a single Newton-Raphson step as in Buhl et al.[26] A continuation method is applied to the SIMP exponent penalty to transform the problem from a relaxed, unpenalized state to the penalized, near discrete formulation with an increment of $\Delta\eta = 1.0$ till $\eta_{max} = 3.0$. It should be mentioned that for high load magnitudes, a large number of iterations are needed within each continuation step. In this work we have used a maximum limit of 100 for $P = 144$ kN. Figure 4.2 contains three columns; the first lists the applied load magnitudes, the second the elastically designed topologies and the third gives the topologies obtained under finite deformations. As expected, it is seen that the elastic designs are the same for all load magnitudes. For a small magnitude of the applied load, the finite deformation design is identical to the elastic solution. When the load is increased the design changes are more noticeable. A very significant change is the angled bar at the bottom of the third column which is obtained with $P = 144$ kN. This bar seems unintuitive in the undeformed state but becomes vertical in the deflected state, essentially serving as a hanger as shown in Fig. 4.3b.

4.2.3 Material Nonlinearities

Material nonlinearities account for yielding of the designs solid phase material. In this work we use the formulation by Maute et al.[25] and describe the nonlinear material behavior by Von Mises yield function with isotropic hardening. We use an

(a) (b)

Figure 4.3: The obtained topology from Fig. 4.2 with $P = 144$ kN in its (a) undeformed and (b) deformed state.

elasto-plastic material model and assume linear hardening.

To show the effect of material nonlinearities on a topology optimization design we consider the benchmark beam example from[25] that is shown in Fig. 4.1 b. The beam is clamped on both sides and subjected to an applied displacement at its midspan. The objective for the design is maximizing the total absorbed energy:

$$f = -\int_{\Omega}\int_{\hat{\epsilon}} \sigma^T d\epsilon d\Omega \tag{4.12}$$

To solve the equilibrium equation in Eq. (4.1) we have developed a Newton-Raphson solver that uses a redial return method to account for the material nonlinearity. The incremental material update is therefore

$$d\sigma = \mathbf{D^{ep}} d\epsilon \tag{4.13}$$

where $\mathbf{D^{ep}}$ is the consistent elasto-plastic tangent modulus. Our algorithm is based on the formulation from Simo and Hughes.[110] The consistent tangent matrix for 2D

plane stress with J_2 plastic flow and isotropic hardening is therefore defined as:

$$\mathbf{D^{ep}} = \mathbf{\Xi} - \frac{[\mathbf{\Xi P}\sigma][\mathbf{\Xi P}\sigma]^{\mathbf{T}}}{\sigma^{\mathbf{T}}\mathbf{P\Xi P}\sigma + \bar{\beta}} \tag{4.14}$$

Here $\mathbf{D}$ is the elastic constitutive matrix and $\mathbf{\Xi}$ is the modified algorithmic elastic tangent modulus. The latter is defined as:

$$\mathbf{\Xi} = \left[\mathbf{D}^{-1} + \Delta\gamma\mathbf{P}\right]^{-1} \tag{4.15}$$

where $\mathbf{P}$ is the projection matrix that for 2D plane stress is as follows:

$$\mathbf{P} = \frac{1}{3}\begin{bmatrix} 2 & -1 & 0 \\ -1 & 2 & 0 \\ 0 & 0 & 6 \end{bmatrix} \tag{4.16}$$

The plastic multiplier $\Delta\gamma$ is found by iteratively solving the consistency condition. The hardening component $\bar{\beta}$ in Eq. (4.14) is calculated using the hardening modulus H:

$$\bar{\beta} = \frac{2}{3}\frac{H}{1 - \frac{2}{3}H\Delta\gamma}\sigma^{\mathbf{T}}\mathbf{P}\sigma \tag{4.17}$$

4.2.3.1 Penalization of Intermediate Densities

Again, the Solid Isotropic Material with Penalization (SIMP) method[19] is used to guide the design to a 0-1 solution. As we use the solids only finite element modeling

the ρ^e_{min} term is left out here. For material nonlinearity the relation between the material properties and the element density are defined by:

$$\begin{aligned} \mathbf{D}^e(\phi) &= (\rho_e)^{\eta_{\mathbf{D}}}\mathbf{D_0}, \\ H^e(\phi) &= (\rho_e)^{\eta_H} H_0, \\ \sigma^e_y(\phi) &= (\rho_e)^{\eta_\sigma}\sigma_{y_0} \end{aligned} \tag{4.18}$$

Here $\mathbf{D}^e(\phi)$ is the elastic constitutive matrix, $H^e(\phi)$ is the plastic hardening modulus and $\sigma^e_y(\phi)$ is the yield stress for element e. The $_0$ subscript denotes the solid phase material properties. It should be noted that the SIMP exponents η can be chosen differently for each of the penalized properties.

4.2.3.2 Sensitivities

We have derived the sensitivities for maximizing the absorbed energy in Eq. (4.12). As the design problem is displacement controlled the derivation follows that of Maute et al.[25] In the sensitivity calculations it is used that the sensitivities of the penalized material properties from Eq. (4.18) are

$$\begin{aligned} \mathbf{D}^e(\phi) &= \eta_{\mathbf{D}}(\rho_e)^{\eta_{\mathbf{D}}-1}\mathbf{D_0}, \\ H^e(\phi) &= \eta_H(\rho_e)^{\eta_H-1} H_0, \\ \sigma^e_y(\phi) &= \eta_\sigma(\rho_e)^{\eta_\sigma-1}\sigma_{y_0} \end{aligned} \tag{4.19}$$

The sensitivity of the incremental form of the absorbed energy from Eq. (4.12) is

$$\begin{aligned}\frac{\partial f}{\partial \rho_e} &= -\frac{\partial}{\partial \rho_e}\int_\Omega \int_{\hat{\epsilon}} \int_\sigma d\sigma^{\mathbf{T}} d\epsilon \; d\Omega \\ &= -\int_\Omega \int_{\hat{\epsilon}} \int_\sigma \left(\left(\frac{\partial d\sigma}{\partial \rho_e} \right)^{\mathbf{T}} d\epsilon + d\sigma^{\mathbf{T}} \frac{\partial d\epsilon}{\partial \rho_e} \right) d\Omega \end{aligned} \tag{4.20}$$

Recall that the weak form of the virtual work is defined by

$$\int_\Omega \delta\epsilon^{\mathbf{T}} \sigma \; d\Omega - \lambda \int_\Gamma \delta \mathbf{d}_g^{\mathbf{T}} \hat{\mathbf{t}} \; d\Gamma = 0$$

where λ is the load factor, $\mathbf{d}_g$ is the applied displacements and $\hat{\mathbf{t}}$ is the load. The sensitivity of the weak form is

$$\int_\Omega \frac{\partial (d\sigma)^{\mathbf{T}}}{\partial \rho_e} \delta\epsilon \; d\Omega - \int_\Gamma \frac{\partial (d\lambda \hat{\mathbf{t}})^{\mathbf{T}}}{\partial \rho_e} \delta \mathbf{d}_g^{\mathbf{T}} \hat{\mathbf{t}} \; d\Gamma = 0 \tag{4.21}$$

The sensitivity of the weak from from Eq. (4.21) is inserted in Eq. (4.20) where $\delta\epsilon = d\epsilon$ and $\delta \mathbf{d}_g = d\mathbf{d}_g$:

$$\frac{\partial f}{\partial \rho_e} = -\int_\Gamma \int_{\hat{\lambda}} \int_{\hat{\mathbf{d}_g}} \frac{\partial (d\lambda \hat{\mathbf{t}})^{\mathbf{T}}}{\partial \rho_e} \hat{\mathbf{t}} \; d\mathbf{d}_g^{\mathbf{T}} \; d\Gamma - \int_\Omega \int_{\hat{\epsilon}} \int_\sigma \left(d\sigma^{\mathbf{T}} \frac{\partial d\epsilon}{\partial \rho_e} \right) d\Omega \tag{4.22}$$

Taking the derivative of the material update from Eq. (4.13) results in:

$$\frac{\partial d\sigma}{\partial \rho_e} = \frac{\partial \mathbf{D}^{\mathbf{ep}}}{\partial \rho_e} d\epsilon + \mathbf{D}^{\mathbf{ep}} \frac{\partial d\epsilon}{\partial \rho_e} \tag{4.23}$$

The sensitivity of the material update from Eq. (4.23) is inserted in the sensitivity expression for the weak form in Eq. (4.21).

$$\begin{aligned}\int_\Omega \int_{\hat{\epsilon}} \int_\epsilon d\boldsymbol{\epsilon}^{\mathbf{T}} \frac{\partial \mathbf{D}^{\mathbf{ep}}}{\partial \rho_e} d\boldsymbol{\epsilon}\, d\Omega \;\; &+ \;\; \int_\Omega \int_{\hat{\epsilon}} \int_\epsilon \frac{\partial d\boldsymbol{\epsilon}^{\mathbf{T}}}{\partial \rho_e} \mathbf{D}^{\mathbf{ep}} d\boldsymbol{\epsilon}\, d\Omega \\ &- \;\; \int_\Gamma \int_{\hat{\lambda}} \int_{\hat{\mathbf{d}}_g} \frac{\partial d\lambda}{\partial \rho_e}\, \hat{\mathbf{t}}^{\mathbf{T}} d\mathbf{d}_g\, d\Gamma = 0\end{aligned}$$

Rewriting leads to

$$\begin{aligned}\int_\Omega \int_{\hat{\epsilon}} \int_\epsilon \frac{\partial d\boldsymbol{\epsilon}^{\mathbf{T}}}{\partial \rho_e} \mathbf{D}^{\mathbf{ep}} d\boldsymbol{\epsilon}\, d\Omega \;\; &= \;\; \int_\Gamma \int_{\hat{\lambda}} \int_{\hat{\mathbf{d}}_g} \frac{\partial d\lambda}{\partial \rho_e}\, \hat{\mathbf{t}}^{\mathbf{T}}\, d\mathbf{d}_g\, d\Gamma \\ &\quad - \int_\Omega \int_{\hat{\epsilon}} \int_\epsilon d\boldsymbol{\epsilon}^{\mathbf{T}} \frac{\partial \mathbf{D}^{\mathbf{ep}}}{\partial \rho_e} d\boldsymbol{\epsilon}\, d\Omega \end{aligned} \tag{4.24}$$

Equation (4.24) is inserted into Eq. (4.22):

$$\frac{\partial f}{\partial \rho_e} = -2 \int_\Gamma \int_{\hat{\lambda}} \int_{\hat{\mathbf{d}}_g} \frac{\partial d\lambda}{\partial \rho_e}\, \hat{\mathbf{t}}^{\mathbf{T}}\, d\mathbf{d}_g\, d\Gamma + \int_\Omega \int_{\hat{\epsilon}} \int_\epsilon d\boldsymbol{\epsilon}^{\mathbf{T}} \frac{\partial \mathbf{D}^{\mathbf{ep}}}{\partial \rho_e} d\boldsymbol{\epsilon}\, d\Omega \tag{4.25}$$

Since our design problem is displacement controlled the therm $\dfrac{\partial d\boldsymbol{\epsilon}}{\partial \rho_e}$ is zero. Assuming that only the displacement controlled point is subject to the load $\hat{t}_j$, i.e. $\hat{\mathbf{t}}^{\mathbf{T}} d\mathbf{d}_g = \hat{t}_j (\hat{d}_g)_j$ means that Eq. (4.24) reduces to

$$\int_\Gamma \int_{\hat{\lambda}} \int_{\hat{\mathbf{u}}} \frac{\partial d\lambda}{\partial \rho_e}\, \hat{\mathbf{t}}^T d\mathbf{u}\, d\Gamma = \int_\Omega \int_{\hat{\epsilon}} \int_\epsilon d\boldsymbol{\epsilon}^T \frac{\partial \mathbf{D}^{\mathbf{ep}}}{\partial \rho_e} d\boldsymbol{\epsilon}\, d\Omega$$

Therefore the sensitivity of the load increment can be written as

$$\frac{\partial d\lambda}{\partial \rho_e} = \frac{\int_\Omega \int_{\hat{\epsilon}} \int_\epsilon d\epsilon^{\mathbf{T}} \frac{\partial \mathbf{D^{ep}}}{\partial \rho_e} d\epsilon \; d\Omega}{\hat{\mathbf{t}}^{\mathbf{T}} \; d\mathbf{d}_g} \tag{4.26}$$

The sensitivity of the objective can now be found by inserting Eq. (4.26) into Eq. (4.25).

$$\frac{\partial f}{\partial \rho_e} = -\int_\Omega \int_{\hat{\epsilon}} \int_\epsilon d\epsilon^{\mathbf{T}} \frac{\partial \mathbf{D^{ep}}}{\partial \rho_e} d\epsilon \; d\Omega \tag{4.27}$$

The sensitivity of the consistent elasto-plastic tangent modulus is found by differentiation of Eq. (4.14). As in,[25] the sensitivity of the consistent elastic-plastic moduli is split up with respect to the elastic constitutive matrix $\mathbf{D}$, the hardening modulus H and the yield stress σ_y:

$$\frac{\partial \mathbf{D^{ep}}}{\partial \rho_e} = \frac{\partial \mathbf{D^{ep}}(\mathbf{D})}{\partial \rho_e} + \frac{\partial \mathbf{D^{ep}}(\mathbf{H})}{\partial \rho_e} + \frac{\partial \mathbf{D^{ep}}(\sigma_\mathbf{y})}{\partial \rho_e} \tag{4.28}$$

Because we use a linear hardening model, it is assumed that the sensitivity of the consistent elasto-plastic moduli due to the change of stress state caused by a design change can be neglected.

$$\frac{\partial \mathbf{D^{ep}}}{\partial \sigma} \frac{\partial \sigma}{\partial \rho_e} = 0$$

This means that the sensitivities $\dfrac{\partial \sigma}{\partial \rho_e}$ and $\dfrac{\partial \Delta\gamma}{\partial \rho_e}$ vanish. The first part of Eq. (4.28)

is therefore:

$$\frac{\partial \mathbf{D}^{\mathbf{ep}}(\mathbf{D})}{\partial \rho_e} = \frac{\partial \mathbf{\Xi}}{\partial \rho_e} - \omega\left(\frac{\partial \mathbf{\Xi}}{\partial \rho_e}[\mathbf{P}\sigma][\mathbf{P}\sigma]^{\mathbf{T}}\mathbf{\Xi}\right) - \omega\left(\mathbf{\Xi}[\mathbf{P}\sigma][\mathbf{P}\sigma]^{\mathbf{T}}\frac{\partial \mathbf{\Xi}}{\partial \rho_e}\right) - \frac{\partial \omega(\mathbf{D})}{\partial \rho_e}\Big(\mathbf{\Xi}[\mathbf{P}\sigma][\mathbf{P}\sigma]^{\mathbf{T}}\mathbf{\Xi}\Big) \tag{4.29}$$

where

$$\omega = \big(\sigma^{\mathbf{T}}\mathbf{P}\mathbf{\Xi}\mathbf{P}\sigma + \bar{\beta}\big)^{-1} \tag{4.30}$$

and

$$\frac{\partial \omega(\mathbf{D})}{\partial \rho_e} = -\omega^2\left(\sigma^{\mathbf{T}}\mathbf{P}\frac{\partial \mathbf{\Xi}}{\partial \rho_e}\mathbf{P}\sigma\right) \tag{4.31}$$

The sensitivity of the modified algorithmic tangent moduli in $\dfrac{\partial \mathbf{\Xi}}{\partial \rho_e}$ Eq. (4.29-4.31) can using matrix calculus be expressed as:

$$\frac{\partial \mathbf{\Xi}}{\partial \rho_e} = \mathbf{\Xi}\mathbf{D}^{-1}\frac{\partial \mathbf{D}}{\partial \rho_e}\mathbf{D}^{-1}\mathbf{\Xi} \tag{4.32}$$

The second part of Eq. (4.28) is derived in a similar way

$$\frac{\partial \mathbf{D}^{\mathbf{ep}}(H)}{\partial \rho_e} = \omega^2\big(\mathbf{\Xi}[\mathbf{P}\sigma][\mathbf{P}\sigma]^{\mathbf{T}}\mathbf{\Xi}\big)\frac{\partial \bar{\beta}}{\partial \rho_e} \tag{4.33}$$

where differentiation of Eq. (4.17) leads to

$$\frac{\partial \bar{\beta}}{\partial \rho_e} = \frac{2}{3}\frac{1}{(1-\frac{2}{3}H\Delta\gamma)^2}\frac{\partial H}{\partial \rho_e}\sigma^{\mathbf{T}}\mathbf{P}\sigma \tag{4.34}$$

The third part of Eq. (4.28) is zero since the elasto-plastic tangent modulus for the von Miss yield function is independent of the yield stress.

$$\frac{\partial \mathbf{D}^{\mathbf{ep}}(\sigma_y)}{\partial \rho_e} = 0 \tag{4.35}$$

4.2.3.3 Clamped Beam Designs

The clamped problem in Fig. 4.1b is solved with plane stress elements. The design domain is defined as $L = 20$ m and $H = 5$ m and the minimum length scale is prescribed as $r_{min} = 0.10$ m. The symmetry of the problem is exploited so only half domain is designed using a 100×50 mesh. The Young's modulus of the base material is taken as $E_0 = 180,000$ kN/m^2, Poisson's ratio as $\nu_0 = 0.3$, the hardening modulus as $H_0 = 0.1$ kN/m^2 and the yield stress is defined as $\sigma_{y_0} = 360$ kN/m^2. A prescribed displacement is applied to 20% of the top mid boundary with a magnitude of $d_g = -0.25$ m. The displacement is applied in 20 equally sized steps

Elastic Base Material	Elasto-Plastic Base Material
	

Figure 4.4: Solutions to the benchmark clamped beam problem with maximized energy absorption as defined in Eq. (4.12) and an elastic– and an elasto-plastic material model, respectively.

in the Newton-Raphson solver. Finally, the design problem is solved with a volume constraint of $V_{max} = 25\%$.

We have solved the problem with different values of the SIMP exponents $\eta_{\mathbf{D}}$, η_H and η_σ and found that using constant values of $\eta_{\mathbf{D}} = \eta_H = 3.0$ and $\eta_\sigma = 2.0$ works well. It is also possible to solve problem with $\eta_{\mathbf{D}} = \eta_H = \eta_\sigma = 3.0$, however, the exponent on the yield stress makes the yield condition more strict in low density elements and therefore tends to make the Newton-Raphson solver expensive in the first design iterations. We have also found that applying continuation strategies, especially on the η_σ exponent, tends to force the solution to an elastic design.

The optimized designs for linear elastic– and elasto-plastic material models are shown in Fig. 4.4. Both the thickness and the number of members in the two designs are seen to be different. In the elastic design case two thick members carry the load to the supports providing the structure a large amount of elastic stiffness. The elasto-plastic design has a lower stiffness in the elastic region but the secondary members provide a higher level of energy dissipation. Maute et al.[25] examined the load-displacement diagrams for the two designs. The area under this curve indicates amount of mechanical energy dissipated. The dissipated energy is $\sim 10\%$ higher for the optimized structure based on the elasto-plastic nonlinear analysis compared to the linear elastic one.

4.3 Extending to Cellular Topology Design with Nonlinear Mechanics

The problem formulation for cellular material design with nonlinear mechanics can be defined as:

$$
\begin{aligned}
\underset{\phi}{\text{minimize}} \quad & f(\phi, \mathbf{C}^H, \mathbf{s}, \mathbf{E}) \\
\text{subject to} \quad & \mathbf{K}_E(\phi)\mathbf{d}_E^{(i)} - \mathbf{f}_E^{(i)}(\phi) \quad \forall \quad i \\
& \mathbf{R}^t(\phi) = \mathbf{K}^t(\phi, \mathbf{d})\mathbf{d}^t - \mathbf{f}^t(\phi) = 0 \quad \forall \quad t \\
& g_E\big(\mathbf{C}^H(\phi, \mathbf{d}_E^{(i)})\big) \geq g_{E,min} \\
& g_{NL}\big(\sigma(\phi, \mathbf{d}), \epsilon(\phi, \mathbf{d})\big) \geq g_{NL,min} \\
& V_{min} \leq \sum_{e \in \Omega} \rho^e(\phi) v^e \leq V_{max} \\
& \phi_{min} \leq \phi_n \leq \phi_{max} \quad \forall \quad n \in \Omega \\
& \mathbf{d}_E^{(i)} \quad \text{is } \Omega\text{-periodic}
\end{aligned}
\tag{4.36}
$$

where the subscript $_E$ refers to the elastic and $_{NL}$ to the nonlinear parts. The superscript t refers to the current load step and $\mathbf{d}^t$ is hence the displacement vector at the current load step and $\mathbf{d}$ the displacement vector untill t. The elastic unit cell equilibrium is given by the first constraint, and constraints g_E include the effective elastic property constraints such as the symmetry conditions. The nonlinear equilibrium constraints are given in the second set of constraints, and constraints g_{NL} comprise

nonlinear property constraints as needed.

As mentioned in the introduction of this chapter, consideration of nonlinear mechanics, particularly inelasticity, in the topology optimization of periodic cellular materials remains a challenge. This is primarily due to the lack of unit cell upscaling methods. Homogenization of nonlinear mechanics from unit cell analysis is not yet established. One way of estimating the nonlinear effective properties is to use finite periodicity. The effective elastic properties and symmetries would still be evaluated using elastic homogenization as described in section 3.2.1. The unit cell topology optimization problem will hence have analysis conducted over two different domains: the unit cell for elastic properties and a structure with finite periodicity for the nonlinear properties. It should be noted that the finite sample size should be demonstrated to adequately estimate the effective material properties.

In this work we have developed a finite plasticity Newton-Raphson FE solver as it is required to solve the topology optimization problem in Eq. (4.36) with both material– and geometric nonlinearities. An additional necessity in performing topology optimization for combined material– and geometric nonlinearities is to develop a sensitivity analysis scheme. Wallin et al.[101] proposed a path-dependent adjoint method when maximizing the plastic energy absorption of beams with finite plasticity and Lotfi[102] estimated the sensitivity for cellular designs by adding the expressions from Maute et al.[25] and Buhl et al.[26] for material and geometric nonlinearities, respectively. This addition does not account for the cross term and therefore necessarily

produces a small error in the sensitivities. In this work we have compared with the sensitivities calculated with finite difference and found the error to be $\sim 10\%$.

4.4 Energy Absorption of Cellular Bulk Metallic Glass Topologies

Lotfi[102] solved the topology optimization problem for cellular design in Eq. (4.36) with a BMG as the base material and maximizing the absorbed energy as the objective. Figure 4.5 shows the unit cell topologies and 3×3 sampled of the cellular materials for volume constraints of $V_{max} = 10\%$, $V_{max} = 12.5\%$ and $V_{max} = 25\%$. The design domain was defined as a 1×1 mm^2 unit cell, square symmetry constraints were applied and the minimum length scale of the topological features was specified as $r_{min} = 0.006$ mm. The elastic properties of BMG were assumed to be $E_0 = 86.9$ GPa and $\nu_0 = 0.375$, and an elasto-plastic uniaxial behavior was defined with $\sigma_{y_0} = 1.475$ GPa and linear hardening with $H_0 = 0.84$ GPa. The upscaling of the unit cell mechanics was performed using finite periodicity with a sample size of 5 unit cells in the $x-$ and $y-$directions. This size was found to achieve a reasonably converged response without an excessive computational cost. Boundary conditions were applied to the finite samples as horizontally fixed on the top and bottom in addition to a vertically fixed bottom. Downward displacements were applied to the top of the samples. The design algorithm considered both material– and geometrical nonlinearities and, as

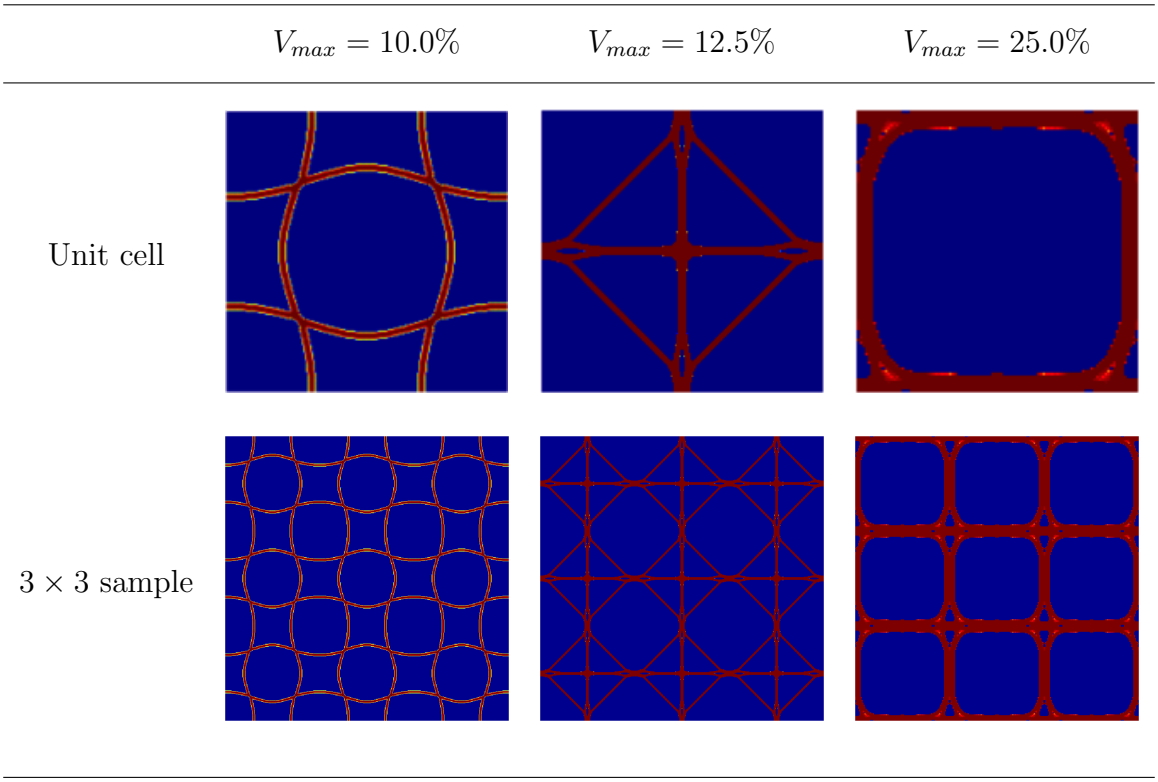

Figure 4.5: Previously obtained unit cell topologies maximized for absorbed energy considering both material– and geometric nonlinearities. A bulk metallic glass (BMG) is used as the base material, the minimum length scale is prescribed as $r_{min} = 0.006$ and designs are made with volume constraints of $V_{max} = 10\%$, $V_{max} = 12.5\%$ and $V_{max} = 25\%$.

mentioned, estimated the sensitivities using existing schemes.[25,26] The stopping criterion for the topology optimization problem was collapse initiation of a unit cell and contact was therefore not considered.

The unit cell topology in Fig. 4.5 for $V_{max} = 10\%$ is interesting because it resembles a buckled grid. Therefore we have in this work conducted nonlinear FE analyses of 5×5 samples of the designed unit cell and of a regular grid with the same volume fraction. The analyses have been performed in the commercial FE program Abaqus

6.13 using an arch length solver. The stress-strain response plots obtained by these analyses are given in Fig. 4.6. It is clearly seen that grid has a higher stiffness and strength than the new design but that the new topology absorbs almost 2.5 times more energy. It should be noted that the stiffness and strength were not objectives in the optimization. When examining the deformations in the two samples, it is seen

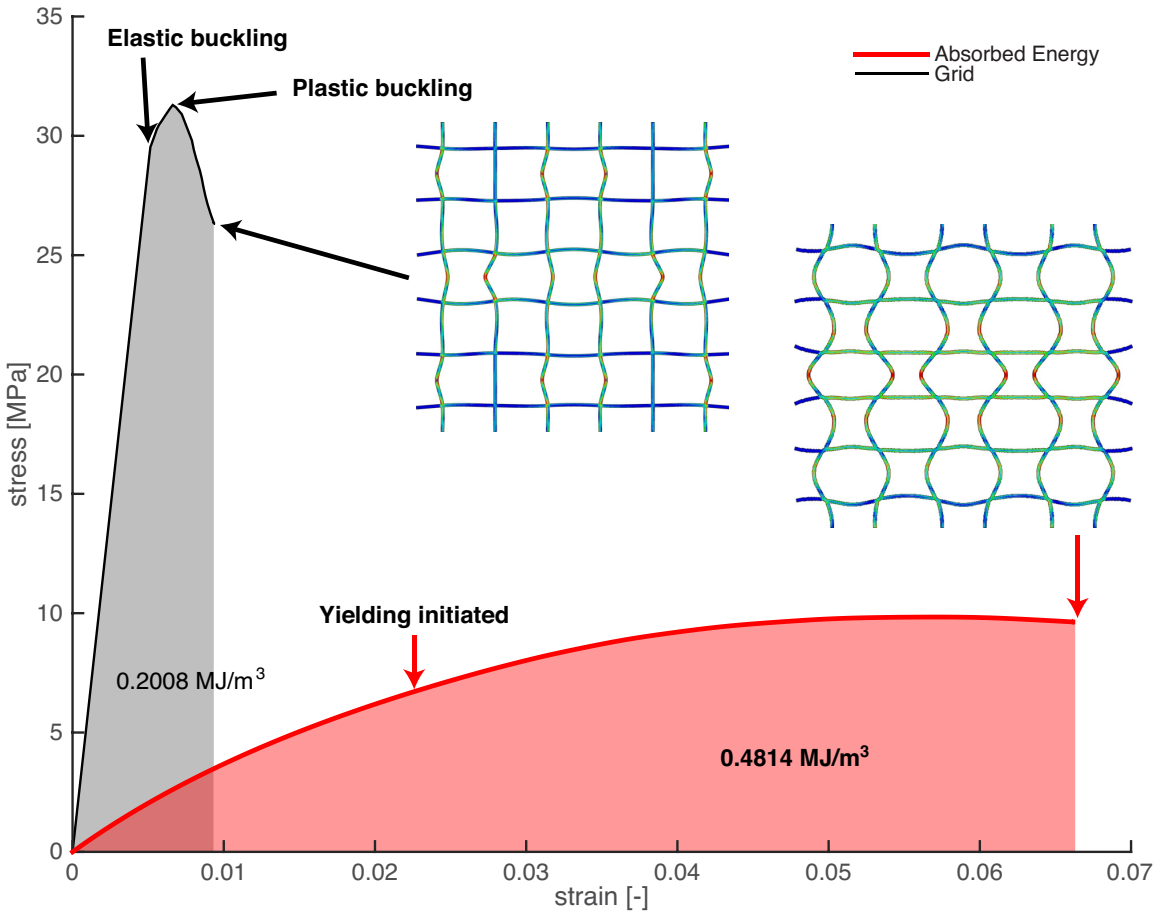

Figure 4.6: Response comparison for $V_{max} = 10\%$ of 5×5 samples of the unit cell topology with optimized energy absorption (Fig. 4.5) and a regular grid. The deformed states are illustrated in the plot and the magnitudes of the absorbed energies are listed.

that the regular grid deforms elastically until buckling is initiated. The buckling very rapidly transitions from elastic to plastic. The plastic buckling creates plastic-hinge like features in the sample that results in unit cell collapse. The new topology initiates yielding at a much higher strain and is seen to use the yielding beneficially to straighten out the curved members and thereby absorb higher levels of energy.

In this work we have designed a range of cellular BMG topologies for elastic objectives with square symmetry constraints and $V_{max} = 10\%$, $V_{max} = 12.5\%$ and $V_{max} = 25\%$. The design follows the description for elastic topology optimization of cellular materials in Chapter 3 and the obtained topologies are shown in Fig. 4.7. The objectives of the optimizations are taken as maximizing the effective bulk– B^H, Young's– E^H and shear modulus G^H and minimizing the Poisson's ratio ν^H. The design domain is discretized using 200×200 plane stress elements and, for the stiffness objectives, the minimum length scale is prescribed as $r_{min} = 0.006$ mm with continuation on the Heaviside parameter till $\beta_{max} = 25.0$. The Poisson's ratio designs are conducted using a robust topology optimization formulation[24] (see section 3.3.1) with $r_{min} = 0.0075$ and $\Delta r = 0.0025$. Continuation is applied to the SIMP exponent till $\eta_{max} = 15.0$ in increments of $\Delta\eta = 1.0$. The stiffness designs start the continuation at $\eta_{init} = 5.0$ and the Poisson's ratio designs at $\eta_{init} = 3.0$.

Finite samples with 5×5 unit cells of all designs (Fig.s 4.5 and 4.7) have been numerically analyzed in Abaqus 6.13 with material– and geometric nonlinearities. The stress-strain response plots obtained by these analyses are given in Fig. 4.8 and

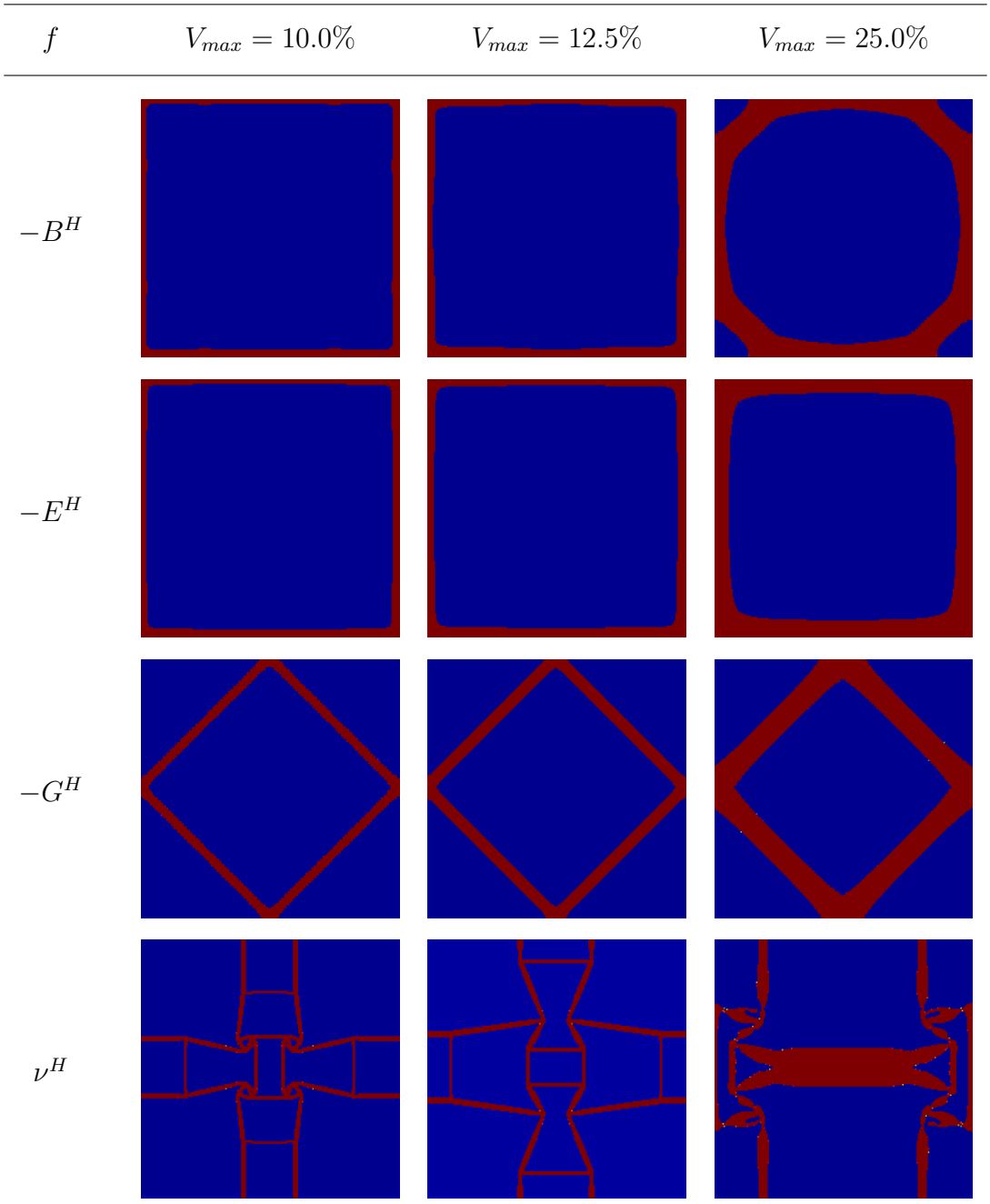

Figure 4.7: Unit cell designs obtained with linear topology optimization for maximized bulk–, Young's– and shear modulus and minimized Poisson's ratio. The base material is a bulk metallic glass (BMG) and the minimum length scale is prescribed as $r_{min} = 0.006$ for the stiffness objectives. A robust formulation is used for the negative Poisson's ratio designs with $r_{min} = 0.0075$ and $\Delta r = 0.0025$.

the absorbed energies are listed in Tab. 4.1. In Fig 4.8a, the stress-strain responses for the unit cell topologies with $V_{max} = 10\%$ show that the absorbed energy design is less stiff and has a lower strength than the bulk– and Young's modulus designs. However, in Tab. 4.1 it is clearly seen that it absorbs more energy. In Fig. 4.8b the responses of the $V_{max} = 12.5\%$ topologies are given and the absorbed energy

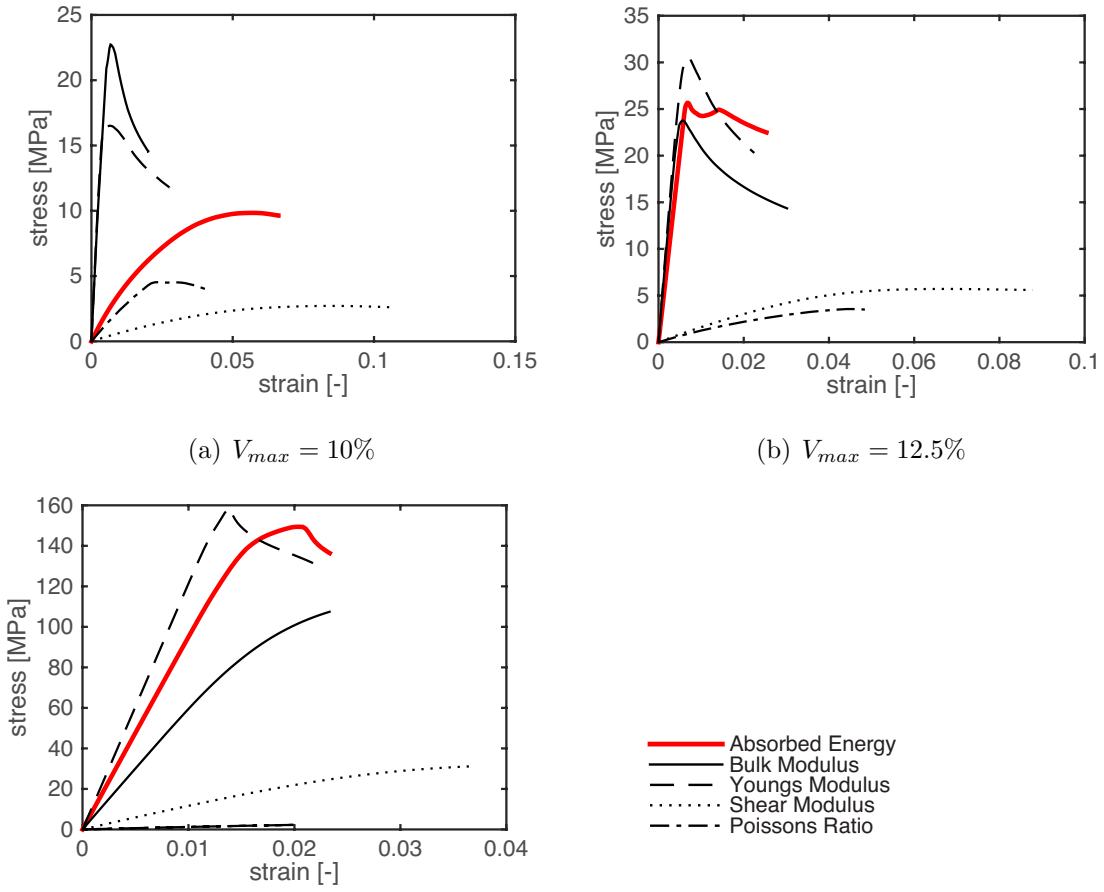

(a) $V_{max} = 10\%$

(b) $V_{max} = 12.5\%$

(c) $V_{max} = 25\%$

Figure 4.8: Stress-strain responses obtained by the nonlinear FE analysis of 5×5 cellular material samples. The absorbed energies for of the each cellular materials are listed in Tab. 4.1.

Table 4.1: Absorbed energies [MJ/m^3] in the response plots in Fig. 4.8 obtained by numerical analyses of 5×5 samples of the unit cells in Fig.s. 4.5-4.7. The largest magnitude for each volume constraint is indicated in bold.

f	$V_{max} = 10\%$	$V_{max} = 12.5\%$	$V_{max} = 25\%$
$-\int_\Omega \int \sigma^{\mathbf{T}} d\epsilon \; d\Omega$	**0.4814**	**0.53859**	2.2633
$-B^H$	0.33048	0.5192	1.4751
$-E^H$	0.37284	0.51081	**2.2873**
$-G^H$	0.21471	0.38074	0.69818
ν^H	0.13675	0.11095	0.05946

design here behaves more similar in stiffness and strength to the bulk– and Young's modulus cellular materials designs. The post-peak behavior however differs, making the energy absorption higher as Tab. 4.1 reveals. Figure 4.8c contains the responses of the designs with $V_{max} = 25\%$ and here the topology optimized for absorbed energy has a stress-strain response that is similar to that of the Young's modulus design. The absorbed energies in Tab. 4.1 for these objectives are also seen to be very close in value, with the Young's modulus topology achieving a slightly higher magnitude. The analyses are both terminated due to yielding in outer walls of the the external unit cells and here the Young's modulus design is slightly thicker than the energy absorbance design. The fact that design optimized for energy absorbance does not achieve the highest level here is because only local optimality can be guaranteed in topology optimization.

It should be noted, that auxetics have been rumored to have good energy ab-

sorbance. As mentioned in section 3.4.1, the negative Poisson's ratio design is self penalizing and therefore the obtained designs in Fig. 4.7 only has material volumes of $V = 9\%$, $V = 10\%$ and $V = 18\%$. Keeping this in mind, the plots in Fig. 4.8 and values in Tab. 4.1 show that the energy absorbance of the herein designed BMG auxetics is poor as they fail due to yielding of the thin members in the hinge regions.

4.5 Summary

The significant improvement of manufacturing technologies presents a remarkable opportunity for the design of new cellular materials with complex topologies and new capabilities. Using topology optimization for cellular material design can leverage the new manufacturing possibilities. Designing for effective linear properties is well understood, however, topology optimization-based design for nonlinear response properties is significantly more challenging. Previous research efforts have mainly concentrated on formulating topology optimization algorithms with nonlinear mechanics for structural, component and device design. Additionally, material– and geometric nonlinearities are typically considered separately. In this work we have illustrated on benchmark beam examples the significant effect including nonlinear mechanics in the design formulation has on the obtained topology.

Topology optimization of cellular materials with nonlinear mechanics faces the additional challenge of the lack of a rigorous upscaling method. Although computa-

tionally heavy, we suggest using finite periodicity. In this work we have discussed the necessary steps in formulating and solving a cellular topology optimization problem with both material– and geometric nonlinearities. Through nonlinear FE analyses of samples with several unit cell topologies we have shown that topology optimization with nonlinear mechanics offers tremendous opportunities in designing cellular materials with new improved effective properties.

Chapter 5

Concluding Remarks and Future Work

In this thesis we have presented topology optimization algorithms for cellular design that aim at incorporating manufacturability restrictions and capabilities and include nonlinearity. The first part of the thesis presented a two-phase projection algorithm that provides the designer with minimum length scale control of both the solid and void phases of the design. The methodology is based on letting the design variable magnitude determine if the solid or the void phase of a design is active. Nonlinear weighting functions are introduced to achieve this. In the presented approach, a solid element can only be created if it receives active solid– and passive void projection. Ongoing work is an extension of the idea that provide the designer maximum feature size control. Here it is required for the creation of a solid element

that a void element is detected in the domain $r_{max,s} + r_{min,v}$. It should be noted that although not seen for the two-phase designs presented in this thesis, the additional maximum length scale projection at current introduces significant nonlinearity in the formulation and hence make it difficult for the optimizer to identify quality solutions.

The second part of this thesis has extended multimaterial topology optimization to cellular material design. In this work we have presented an algorithm and used it to design for a range of linear objectives, including stiffness and Poisson's ratio and combinations of bulk modulus and thermal conductivity. The designed we obtained for the objectives that typically are associated with a nonlinear design space (the negative Poisson's ratio and multiobjective designs) required some parameter tuning. The used multimaterial approach would benefit from a generalization such the increments of material properties (ΔE_i and $\Delta \kappa_i$) does not need to be equal. However, this generalization should be constructed in way that does not introduce unnecessary nonlinearity to the design space. This will especially be important if extending to design governed by nonlinear mechanics. Moreover, applicability of the present work could be demonstrated on examples where the base materials vary in cost.

The thesis' third part looked at extending topology optimization to design cellular topologies governed by nonlinear mechanics. To achieve this, an upscaling law must be defined to connect the unit cell behavior to the effective material properties. In lack of a recognized homogenization law for nonlinear mechanics, we suggest using finite periodicity. A future direction of this work is to apply the discussed topology

optimization approach to design cellular materials with improved energy absorption. However, a rigorous sensitivity scheme must be developed for material– and geometric nonlinear analysis. Further, a thorough examination of how the choice of stopping criterion in the design algorithm affects the stress-strain response of the effective material would be interesting. Finally, all algorithms in this thesis would benefit from incorporating uncertainties in the design formulation. This is especially important when designing under nonlinear mechanics as the effects of uncertainties, such as imperfections, may amplify the nonlinear response.

Bibliography

[1] M. P. Bendsøe and O. Sigmund, *Topology optimization: Theory, Methods and Applications*. Berlin, Germany: Springer-Verlag, 1 ed., 2003.

[2] M. Sarkisian, "Tall buildings design inspired by nature," in *36th Conference in Our World in Concrete and Structures*, (Singapore), pp. 9–16, August 2011.

[3] L. Krog, A. Tucker, M. Kemp, and R. Boyd, "Topology optimization of aircraft wing box ribs," in *10th AIAA/ISSMO Multidisciplinary Analysis and Optimization Conference*, (Albany, NY), pp. 6–1–6–16, August 2004.

[4] J. E. Cadman, S. Zhou, Y. Chen, and Q. Li, "On design of multi-functional microstructural materials," *Journal of Materials Science*, vol. 48, no. 1, pp. 51–66, 2013.

[5] M. Osanov and J. K. Guest, "Topology optimization for architected materials design," *Annual Review of Materials Research*, vol. 46, pp. 211–233, 2016.

[6] O. Sigmund, "Materials with prescribed constitutive parameters: An inverse ho-

mogenization problem," *International Journal of Solids and Structures*, vol. 31, no. 17, pp. 2313–2329, 1994.

[7] O. Sigmund, "Tailoring materials with prescribed elastic properties," *Mechanics of Materials*, vol. 20, no. 4, pp. 351–368, 1995.

[8] O. Sigmund and S. Torquato, "Composites with extremal thermal expansion coefficients," *Applied Physics Letters*, vol. 69, no. 21, pp. 3203–3205, 1996.

[9] O. Sigmund and S. Torquato, "Design of materials with extreme thermal expansion using a three-phase topology optimization method," *Journal of Mechanics and Physics of Solids*, vol. 45, no. 6, pp. 1037–1067, 1997.

[10] E. C. Elli Silva, J. S. Ono Fonseca, and N. Kikuchi, "Optimal design of piezoelectric microstructures," *Computational Mechanics*, vol. 19, no. 5, pp. 397–410, 1997.

[11] O. Sigmund and S. Torquato, "Design of smart composite materials using topology optimization," *Smart Materials and Structures*, vol. 8, no. 3, pp. 365–379, 1999.

[12] J. K. Guest and J. H. Prévost, "Optimizing multifunctional materials: design of microstructures for maximized stiffness and fluid permeability," *Computer Methods in Applied Mechanics and Engineering*, vol. 196, no. 4, pp. 1006–1017, 2007.

BIBLIOGRAPHY

[13] J. K. Guest and J. H. Prévost, "Design of maximum permeability material structures," *International Journal of Solids and Structures*, vol. 43, no. 22, pp. 7028–7047, 2006.

[14] V. J. Challis, J. K. Guest, J. F. Grotowski, and A. P. Roberts, "Computationally generated cross-property bounds for stiffness and fluid permeability using topology optimization," *International Journal of Solids and Structures*, vol. 49, no. 23, pp. 3397–3408, 2012.

[15] V. J. Challis, A. P. Roberts, and A. H. Wilkins, "Design of three dimensional isotropic microstructures for maximized stiffness and conductivity," *International Journal of Solids and Structures*, vol. 45, no. 14, pp. 4130–4146, 2008.

[16] O. Sigmund, "On the usefulness of non-gradient approaches in topology optimization," *Structural and Multidisciplinary Optimization*, vol. 43, no. 5, pp. 589–596, 2011.

[17] O. Sigmund and K. Maute, "Topology optimization approaches," *Structural and Multidisciplinary Optimization*, vol. 48, no. 6, pp. 1031–1055, 2013.

[18] M. P. Bendsøe and N. Kikuchi, "Generating optimal topologies in structural design using a homogenization method," *Computer Methods in Applied Mechanics and Engineering*, vol. 71, no. 2, pp. 197–224, 1988.

BIBLIOGRAPHY

[19] M. P. Bendsøe, "Optimal shape design as a material distribution problem," *Structural Optimization*, vol. 1, no. 4, pp. 193–202, 1989.

[20] G. I. N. Rozvany, M. Zhou, and T. Birker, "Generalized shape optimization without homogenization," *Structural Optimization*, vol. 4, no. 3–4, pp. 250–252, 1992.

[21] M. Stolpe and K. Svanberg, "An alternative interpolation scheme for minimum compliance topology optimization," *Structural and Multidisciplinary Optimization*, vol. 22, no. 2, pp. 116–124, 2001.

[22] J. K. Guest, J. H. Prévost, and T. Belytschko, "Achieving minimum length scale in topology optimization using nodal design variables and projection functions," *International Journal for Numerical Methods in Engineering*, vol. 61, no. 2, pp. 238–254, 2004.

[23] O. Sigmund, "Morphology-based black and white filters for topology optimization," *Structural and Multidisciplinary Optimization*, vol. 33, no. 4–5, pp. 401–424, 2007.

[24] A. T. Gaynor, N. A. Meisel, C. B. Williams, and J. K. Guest, "Multiple-material topology optimization of compliant mechanisms created via polyjet three-dimensional printing," *Journal of Manufacturing Science and Engineering*, vol. 136, no. 6, pp. 061015–1–061015–10, 2014.

BIBLIOGRAPHY

[25] K. Maute, S. Schwarz, and E. Ramm, "Adaptive topology optimization of elastoplastic structures," *Structural Optimization*, vol. 15, no. 2, pp. 81–91, 1998.

[26] T. Buhl, C. B. W. Pedersen, and O. Sigmund, "Stiffness design of geometrically nonlinear structures using topology optimization," *Structural and Multidisciplinary Optimization*, vol. 19, no. 2, pp. 93–104, 2000.

[27] C. B. W. Pedersen, T. Buhl, and O. Sigmund, "Topology synthesis of large-displacement compliant mechanisms," *International Journal for numerical methods in engineering*, vol. 50, no. 12, pp. 2683–2705, 2001.

[28] J. K. Guest and M. Zhu, "Casting and milling restrictions in topology optimization via projection-based algorithms," in *ASME 2012 International Design Engineering Technical Conferences and Computers and Information in Engineering Conference*, (Chicago, IL), pp. 913–920, August 2012.

[29] G. Allaire, F. Jouve, and G. Michailidis, "Casting constraints in structural optimization via a level-set method," in *10th World Congress on Structural and Multidisciplinary Optimization*, (Orlando, FL), pp. 1–10, June 2013.

[30] A. T. Gaynor, J. K. Guest, and C. D. Moen, "Reinforced concrete force visualization and design using bilinear truss-continuum topology optimization," *Journal of Structural Engineering*, vol. 139, no. 4, pp. 607–618, 2012.

BIBLIOGRAPHY

[31] Y. Yang, C. D. Moen, and J. K. Guest, "Three-dimensional force flow paths and reinforcement design in concrete via stress-dependent truss-continuum topology optimization," *Journal of Engineering Mechanics*, vol. 141, no. 1, pp. 04014106–1–04014106–10, 2014.

[32] J. K. Guest, "Optimizing the layout of discrete objects in structures and materials: A projection-based topology optimization approach," *Computer Methods in Applied Mechanics and Engineering*, vol. 283, pp. 330–351, 2015.

[33] S.-H. Ha and J. K. Guest, "Optimizing inclusion shapes and patterns in periodic materials using discrete object projection," *Structural and Multidisciplinary Optimization*, vol. 50, no. 1, pp. 65–80, 2014.

[34] S. Koh and J. K. Guest, "Topology optimization of components with embedded objects using discrete object," in *Proceedings of the ASME 2017 International Design Engineering Technical Conferences & Computers and Information in Engineering Conference*, (Cleveland, OH), pp. 1–9, August 2017.

[35] A. T. Gaynor and J. K. Guest, "Topology optimization considering overhang constraints: Eliminating sacrificial support material in additive manufacturing through design," *Structural and Multidisciplinary Optimization*, vol. 54, no. 5, pp. 1157–1172, 2016.

[36] M. Langelaar, "An additive manufacturing filter for topology optimization of

print-ready designs," *Structural and Multidisciplinary Optimization*, vol. 55, no. 3, pp. 871–883, 2017.

[37] G. Allaire, C. Dapogny, A. Faure, and G. Michailidis, "A model of layer by layer mechanical constraint for additive manufacturing in shape and topology optimization," in *12th World Congress on Structural and Multidisciplinary Optimization*, (Braunschweig, Germany), pp. 1–6, June 2017.

[38] J. Wu, N. Aage, R. Westermann, and O. Sigmund, "Infill optimization for additive manufacturing approaching bone-like porous structures," *IEEE Transactions on Visualization and Computer Graphics*, pp. 1–13, 2017.

[39] M. Osanov and J. K. Guest, "Topology optimization for additive manufacturing considering layer-based minimum feature sizes," in *Proceedings of the ASME 2017 International Design Engineering Technical Conferences & Computers and Information in Engineering Conference*, (Cleveland, OH), pp. 1–8, August 2017.

[40] M. P. Bendsøe and O. Sigmund, "Material interpolation schemes in topology optimization," *Archive of applied mechanics*, vol. 69, no. 9–10, pp. 635–654, 1999.

[41] O. Sigmund and J. Petersson, "Numerical instabilities in topology optimization: A survey on procedures dealing with checkerboards, mesh-dependencies and local minima," *Structural and Multidisciplinary Optimization*, vol. 16, no. 1, pp. 68–75, 1998.

BIBLIOGRAPHY

[42] T. Borrvall, "Topology optimization of elastic continua using restriction," *Archives of Computational Methods in Engineering*, vol. 8, no. 4, pp. 351–385, 2001.

[43] O. Sigmund, *Design of Material Structures using Topology Optimization*. PhD thesis, The Technical University of Denmark, Lyngby, Denmark, December 1994.

[44] A. Diaz and O. Sigmund, "Checkerboard patterns in layout optimization," *Structural and Multidisciplinary Optimization*, vol. 10, no. 1, pp. 40–45, 1995.

[45] B. Bourdin, "Filters in topology optimization," *International Journal for Numerical Methods in Engineering*, vol. 50, no. 9, pp. 2143–2158, 2001.

[46] T. E. Bruns and D. A. Tortorelli, "Topology optimization of non-linear elastic structures and compliant mechanisms," *Computer Methods in Applied Mechanics and Engineering*, vol. 190, no. 26, pp. 3443–3459, 2001.

[47] J. Petersson and O. Sigmund, "Slope constrained topology optimization," *International Journal for Numerical Methods in Engineering*, vol. 41, no. 8, pp. 1427–1434, 1998.

[48] T. A. Poulsen, "A new scheme for imposing a minimum length scale in topology optimization," *International Journal for Numerical Methods in Engineering*, vol. 57, no. 6, pp. 741–760, 2003.

BIBLIOGRAPHY

[49] S. Xu, Y. Cai, and G. Cheng, "Volume preserving nonlinear density filter based on heaviside functions," *Structural and Multidisciplinary Optimization*, vol. 41, no. 4, pp. 495–505, 2010.

[50] K. Svanberg and H. Svärd, "Density filters for topology optimization based on the pythagorean means," *Structural and Multidisciplinary Optimization*, vol. 48, no. 5, pp. 859–875, 2013.

[51] E. Wadbro and L. Hägg, "On quasi-arithmetic mean based filters and their fast evaluation for large-scale topology optimization," *Structural and Multidisciplinary Optimization*, vol. 52, no. 5, pp. 879–888, 2015.

[52] F. Wang, B. S. Lazarov, and O. Sigmund, "On projection methods, convergence and robust formulations in topology optimization," *Structural and Multidisciplinary Optimization*, vol. 43, no. 6, pp. 767–784, 2011.

[53] M. Zhou, B. S. Lazarov, F. Wang, and O. Sigmund, "Minimum length scale in topology optimization by geometric constraints," *Computer Methods in Applied Mechanics and Engineering*, vol. 293, pp. 266–282, 2015.

[54] B. S. Lazarov and F. Wang, "Maximum length scale in density based topology optimization," *Computer Methods in Applied Mechanics and Engineering*, vol. 318, pp. 826–844, 2017.

[55] J. K. Guest, "Imposing maximum length scale in topology optimization," *Structural and Multidisciplinary Optimization*, vol. 37, no. 5, pp. 463–473, 2009.

[56] J. V. Carstensen and J. K. Guest, "New projection methods for two-phase minimum and maximum length scale control in topology optimization," in *15th AIAA/ISSMO Multidisciplinary Analysis and Optimization Conference*, (Atlanta, GA), pp. 1–11, June 2014.

[57] S. Chen, M. Y. Wang, and A. S. Liu, "Shape feature control in structural topology optimization," *Computer-Aided Design*, vol. 40, no. 9, pp. 951–962, 2008.

[58] G. Allaire, F. Jouve, and G. Michailidis, "Thickness control in structural optimization via a level set method," *Structural and Multidisciplinary Optimization*, vol. 53, no. 6, pp. 1349–1382, 2016.

[59] W. Zhang, W. Zhong, and X. Guo, "An explicit length scale control approach in simp-based topology optimization," *Computer Methods in Applied Mechanics and Engineering*, vol. 282, pp. 71–86, 2014.

[60] J. K. Guest, "Topology optimization with multiple phase projection," *Computer Methods in Applied Mechanics and Engineering*, vol. 199, no. 1, pp. 123–135, 2009.

[61] J. K. Guest and L. C. Smith Genut, "Reducing dimensionality in topology

optimization using adaptive design variable fields," *International journal for numerical methods in engineering*, vol. 81, no. 8, pp. 1019–1045, 2010.

[62] J. K. Guest, "Improved projection-based algorithms for continuum topology optimization," in *Collection of Technical Papers - 13th AIAA/ISSMO Multidisciplinary Analysis and Optimization Conference*, (Fort Worth, TX), pp. 1–9, 2010.

[63] K. Svanberg, "The method of moving asymptotes: A new method for structural optimization," *International journal for numerical methods in engineering*, vol. 24, no. 2, pp. 359–373, 1987.

[64] K. Svanberg, "A globally convergent version of MMA without linesearch," in *Proceedings of the first world congress of structural and multidisciplinary optimization* (G. Rozvany and N. Olhoff, eds.), vol. 28, (Goslar, Germany), pp. 9–16, 1995.

[65] J. K. Guest, A. Asadpoure, and S.-H. Ha, "Eliminating beta-continuation from heaviside projection and density filter algorithms," *Structural and Multidisciplinary Optimization*, vol. 44, no. 4, pp. 443–453, 2011.

[66] O. Sigmund, N. Aage, and E. Andreassen, "On the (non-)optimality of Michell structures," *Structural and Multidisciplinary Optimization*, vol. 54, no. 2, pp. 361–373, 2016.

BIBLIOGRAPHY

[67] E. Andreassen, B. S. Lazarov, and O. Sigmund, "Design of manufacturable 3d extremal elastic microstructure," *Mechanics of Materials*, vol. 69, no. 1, pp. 1–10, 2014.

[68] V. J. Challis, A. P. Roberts, J. F. Grotowski, L.-C. Zhang, and T. B. Sercombe, "Prototypes for bone implant scaffolds designed via topology optimization and manufactured by solid freeform fabrication," *Advanced Engineering Materials*, vol. 12, no. 11, pp. 1106–1110, 2010.

[69] L. Zhao, S.-H. Ha, K. W. Sharp, A. B. Geltmacher, R. W. Fonda, A. H. Kinsey, Y. Zhang, S. M. Ryan, D. Erdeniz, D. C. Dunand, K. J. Hemker, J. K. Guest, and T. P. Weihs, "Permeability measurements and modeling of topology-optimized metallic 3-d woven lattices," *Acta Materialia*, vol. 81, pp. 326–336, 2014.

[70] Y. Zhang, S.-H. Ha, K. W. Sharp, J. K. Guest, T. P. Weihs, and K. J. Hemker, "Fabrication and mechanical characterization of 3d woven cu lattice materials," *Materials and Design*, vol. 85, pp. 743–752, 2015.

[71] L. Zhao, S. M. Ryan, J. K. Ortega, S.-H. Ha, K. W. Sharp, J. K. Guest, K. J. Hemker, and T. P. Weihs, "Experimental investigation of 3d woven cu lattices for heat exchanger applications," *International Journal of Heat and Mass Transfer*, vol. 96, pp. 296–311, 2016.

[72] S. Zhou, W. Li, Y. Chen, G. Sun, and Q. Li, "Topology optimization for negative

permeability metamaterials using level-set algorithm," *Acta Materialia*, vol. 59, no. 7, pp. 2624–2636, 2011.

[73] N. de Kruijf, S. Zhou, Q. Li, and Y.-W. Mai, "Topological design of structures and composite materials with multiobjectives," *International Journal of Solids and Structures*, vol. 44, no. 22, pp. 7092–7109, 2007.

[74] O. Sigmund, "Manufacturing tolerant topology optimization," *Acta Mechanica Sinica*, vol. 25, no. 5, pp. 227–239, 2009.

[75] L. Yin and G. K. Ananthasuresh, "Topology optimization of compliant mechanisms with multiple materials using a peak function material interpolation scheme," *Structural and Multidisciplinary Optimization*, vol. 23, no. 1, pp. 49–62, 2001.

[76] S. Watts and D. A. Tortorelli, "An n?material thresholding method for improving integerness of solutions in topology optimization," *International Journal for Numerical Methods in Engineering*, vol. 108, no. 12, pp. 1498–1524, 2016.

[77] E. Andreassen, J. S. Jensen, and O. Sigmund, "Optimal design of porous materials," Tech. Rep. DCAMM Special Report; No. S172, DTU Mechanical Engineering, January 2015.

[78] E. Andreassen, *Optimal Design of Porous Materials*. PhD thesis, The Technical University of Denmark, Lyngby, Denmark, January 2015.

[79] S. Watts and D. A. Tortorelli, "Optimality of thermal expansion bounds in three dimensions," *Extreme Mechanics Letters*, vol. 12, pp. 97–100, 2017.

[80] L. V. Gibiansky and O. Sigmund, "Multiphase composites with extremal bulk modulus," *Journal of the Mechanics and Physics of Solids*, vol. 48, no. 3, pp. 461–498, 2000.

[81] Z. Hashin and S. Shtrikman, "A variational approach to the theory of the elastic behaviour of multiphase materials," *Journal of the Mechanics and Physics of Solids*, vol. 11, no. 2, pp. 127–140, 1966.

[82] L. J. Walpole, "On bounds for the overall elastic moduli of inhomogeneous systemsi," *Journal of the Mechanics and Physics of Solids*, vol. 14, no. 3, pp. 151–162, 1966.

[83] S. Torquato, *Random heterogeneous materials: microstructure and macroscopic properties*. New York, NY: Springer-Verlag, 2 ed., 2002.

[84] J. Guedes and N. Kikuchi, "Preprocessing and postprocessing for materials based on the homogenization method with adaptive finite element methods," *Computer methods in applied mechanics and engineering*, vol. 83, no. 2, pp. 143–198, 1990.

[85] B. Hassani and E. Hinton, "A review of homogenization and topology optimiza-

tion i – homogenization theory for media with periodic structure," *Computers and Structures*, vol. 69, no. 6, pp. 707–717, 1998.

[86] B. Hassani and E. Hinton, "A review of homogenization and topology optimization ii – analytical and nummerical solution of homogenization equations," *Computers and Structures*, vol. 69, no. 6, pp. 719–738, 1998.

[87] E. Andreassen and C. S. Andreasen, "How to determine composite material properties using numerical homogenization," *Computational Materials Science*, vol. 83, pp. 488–495, 2014.

[88] J. K. Guest, *Design of Optimal Porous Material Structures for Maximized Stiffness and Permeability Using Topology Optimization and Finite Element Methods*. PhD thesis, Princeton University, Princeton, NJ, April 2005.

[89] L. V. Gibiansky and S. Torquato, "Thermal expansion of isotropic multiphase composites and polycrystals," *Journal of Mechanics and Physics of Solids*, vol. 45, no. 7, pp. 1223–1252, 1997.

[90] G. Kumar, A. Desai, and J. Schroers, "Bulk metallic glass: the smaller the better," *Advanced materials*, vol. 23, no. 4, pp. 461–476, 2011.

[91] Z. Liu, W. Chen, J. V. Carstensen, J. Ketkaew, R. M. O. Mota, J. K. Guest, and J. Schroers, "3d metallic glass cellular structures," *Acta Materialia*, vol. 105, pp. 35–43, 2016.

[92] C. C. Swan and I. Kosaka, "Voigt-reuss topology optimization for structures with nonlinear material behaviors," *International Journal for Numerical Methods in Engineering*, vol. 40, no. 20, pp. 3785–3814, 1997.

[93] T. E. Bruns and D. A. Tortorelli, "An element removal and reintroduction strategy for the topology optimization of structures and compliant mechanisms," *International journal for numerical methods in engineering*, vol. 57, no. 10, pp. 1413–1430, 2003.

[94] R. Behrou and J. K. Guest, "Topology optimization for transient response of structures subjected to dynamic loads," in *18th AIAA/ISSMO Multidisciplinary and Optimization Conference*, (Denver, CO), pp. 1–13, June 2017.

[95] J. Oest and E. Lund, "Topology optimization with finite-life fatigue constraints," *Structural and Multidisciplinary Optimization*, pp. 1–15, 2017.

[96] M. Lawry and K. Maute, "Level set topology optimization of structural problems with interface cohesion," *Structural and Multidisciplinary Optimization*, vol. 52, no. 6, pp. 1107–1119, 2015.

[97] M. Lawry and K. Maute, "Level set shape and topology optimization of nite strain bilateral contact problems," *International Journal for Numerical Methods in Engineering*, pp. 1–39, 2017.

[98] R. Behrou, M. Lawry, and K. Maute, "Level set topology optimization of struc-

tural problems with interface cohesion," *International Journal for Numerical Methods in Engineering*, pp. 1–27, 2017.

[99] P. B. Nakshatrala, D. A. Tortorelli, and K. B. Nakshatrala, "Nonlinear structural design using multiscale topology optimization. Part I: Static formulation," *Computer Methods in Applied Mechanics and Engineering*, vol. 261–262, pp. 167–176, 2013.

[100] F. Wang, O. Sigmund, and J. S. Jensen, "Design of materials with prescribed nonlinear properties," *Journal of Mechanics and Physics of Solids*, vol. 69, pp. 156–174, 2014.

[101] M. Wallin, V. Jönsson, and E. Wingren, "Topology optimization based on finite strain plasticity," *Structural and Multidisciplinary Optimization*, vol. 54, no. 4, pp. 783–793, 2016.

[102] R. Lotfi, *Topology Optimization under Nonlinear Mechanics*. PhD thesis, Johns Hopkins University, Baltimore, MD, November 2013.

[103] P. B. Nakshatrala and D. A. Tortorelli, "Topology optimization for effective energy propagation in rate-independent elastoplastic material systems," *Computer Methods in Applied Mechanics and Engineering*, vol. 295, pp. 305–326, 2015.

[104] P. B. Nakshatrala and D. A. Tortorelli, "Nonlinear structural design using multi-

scale topology optimization. Part II: Transient formulation," *Computer Methods in Applied Mechanics and Engineering*, vol. 304, pp. 605–618, 2016.

[105] R. Lotfi, S. ha, J. Carstensen, and J. K. Guest, "Topology optimization for cellular material design," in *MRS Proceedings*, (Cambridge University Press), 2014.

[106] J. V. Carstensen, R. Lotfi, and J. K. Guest, "Topology optimization of cellular materials for properties governed by nonlinear mechanics," in *11th World Congress on Structural and Multidisciplinary Optimization*, (Sydney, Australia), pp. 1–6, June 2015.

[107] J. V. Carstensen, R. Lotfi, W. Chen, J. Schroers, and J. K. Guest, "Topology optimization of cellular materials with maximized energy absorption," in *Proceedings of the ASME 2015 International Design Engineering Technical Conferences & Computers and Information in Engineering Conference*, (Boston, MA), pp. 1–10, August 2015.

[108] K.-J. Bathe, *Finite Element Procedures in Engineering Analysis*. Englewood Cliffs, NJ: Prentice-Hall, 1 ed., 1982.

[109] R. de Borst, M. A. Crisfield, J. J. C. Remembers, and C. V. Verhoodel, *Finite Element Procedures in Engineering Analysis*. Chichester, United Kingdom: John Wiley & Sons, 2 ed., 2012.

BIBLIOGRAPHY

[110] J. C. Simo and T. J. R. Hughes, *Computational Inelasticity*. New York, NY: Springer-Verlag, 2 ed., 2000.

[111] K. Maute and E. Ramm, "Adaptive topology optimization," *Structural optimization*, vol. 10, no. 2, pp. 100–112, 1995.

[112] A. Klarbring and N. Strömberg, "Topology optimization of hyperelastic bodies including non-zero prescribed displacements," *Structural and Multidisciplinary Optimization*, vol. 47, no. 1, pp. 37–48, 2013.

[113] F. Wang, B. S. Lazarov, O. Sigmund, and J. S. Jensen, "Interpolation scheme for fictitious domain techniques and topology optimization of finite strain elastic problems," *Computer Methods in Applied Mechanics and Engineering*, vol. 276, pp. 453–472, 2014.

Vita

Josephine Voigt Carstensen received her B.Sc. and M.Sc. degrees in Civil Engineering from the Technical University of Denmark in 2008 and 2011. As part of the latter, Josephine spent five months conducting research at the BRE Centre for Fire Safety Engineering at the University of Edinburgh (2010-2011). In 2012 she enrolled in the Civil Engineering Ph.D. program at Johns Hopkins University. Her research focuses on topology optimization; more specifically on developing formulations that improves the manufacturability of the designs and that includes nonlinear mechanics in the formulation.

Starting in August 2017, Josephine will work as a Lecturer in the Department of Civil and Environmental Engineering and the Department of Architecture at Massachusetts Institute of Technology in Cambridge, MA, where she will teach and continue her research on topology optimization.